DATCP2021-2

Geophysics-informed Transport and Shallow Bedrock Topography in NE and SC Wisconsin Counties

Report Submitted

to the Wisconsin Department of Natural Resources (DNR)

and

to the Wisconsin Department of Wisconsin Department of Agriculture, Trade and Consumer Protection (DATCP)

Research Team:

Dante Fratta (PI)
David J. Hart
Laure Fuentes
Katherine Swager
Michael Cardiff
Jingyi Huang
Francisco Arriaga
University of Wisconsin-Madison

December 30, 2023

Geophysics-informed Transport and Shallow Bedrock Topography in NE and SC Wisconsin Counties

Introduction to the Report

Due to the different components of the funded study, we divided the report into two parts:

- Part A: Seasonal Monitoring of an Infiltration Experiment Using Time-Lapse Geophysics and Chemical Characterization to Understand Nitrate Transport in the Vadose Zone
- Part B: Evaluation of Geophysical Techniques for the Determination of Bedrock Depth

The first part deals with evaluating a set of field and laboratory experiments aimed at imaging and studying the fate of nitrate in the vadose zone in an agricultural setting. The second part of the report assesses the geophysical techniques designed to comply with Wisconsin N.R. 151 *Maximum liquid manure application rates for Silurian bedrock as a function of depth* by farmers across Wisconsin. While each of these parts should be considered an individual stand report, they are linked using geophysical techniques to image processes and structures within the near-surface sediments and rocks.

Acknowledgments: several individuals have helped with this study, including Dr. Carla Romano, Dr. Christopher Zahasky, Ms. Emma Carew, Mr. Pete Chase, Mr. Jake Pfund, Mr. Bronson McQueen, and several farmers and property owners across the State of Wisconsin. Their participation is greatly appreciated.

Table of Content

Part A: Seasonal Monitoring of an Infiltration Experiment Using Time-Lapse Geophysics and Chemical Characterization to Understand Nitrate Transport in the Vadose Zone

A.0. Abstract

Nitrogen-based chemical fertilizers and manure are used throughout Wisconsin to provide crop nutrients. However, nitrogen from these fertilizers may leach from the surface and root zone to the groundwater, creating health risks for communities relying on private wells for drinking water. Therefore, understanding the fate of nitrate transport and infiltration processes in the vadose zone is crucial for protecting groundwater quality and meeting drinking water standards. Infiltration of groundwater contaminants is most likely to occur during periods of intense recharge (i.e., significant precipitation events). To simulate this natural process, we conducted localized infiltration experiments on a Lower Wisconsin River Valley site with sandy soils at the farm field's edge using a constant head infiltrometer with a bromide tracer solution. We monitored the infiltration process using electrical resistivity tomography and ground penetrating radar. We also used ion chromatography to measure bromide and nitrate concentrations (present due to fertilization applications) in soil cores collected immediately after the infiltration and a year later. The results show a general trend of nitrate contamination high at the surface and decreases exponentially with depth. However, the results from the infiltration experiment using a sodium bromide solution show an almost constant concentration with depth for samples collected one year after the infiltration experiment. In addition, the concentration, organic content, and grain size distribution analyses show data spikes at depths around 30 cm, 60 cm, 100 cm, and 150 cm, potentially showing a higher probability of contamination retention at subtle boundary composition changes. The difference in these results may be related to the

localized injection of the sodium bromide solution vs. the uniform spreading of nitrate fertilizer in the field, the duration of the compounds' application, and soil heterogeneities, emphasizing the complex nature of the processes.

A.1. Introduction

A.1.1 Motivation

The most common groundwater contaminant in Wisconsin is nitrate (WDHS 2022), with about 90% of the nitrate contamination directly linked to agricultural practices. In addition, more than 42,000 private wells exceed the EPA-established maximum contaminant level (MCL) of 10 mg/L (ppm) under the Safe Drinking Water Act (EPA 2009). The presence of nitrates in the groundwater means that many state residents do not have access to safe drinking water and are at a higher risk for health problems such as thyroid disease, cancer, "blue baby syndrome," and other congenital disabilities (Laine 2021).

The origin of nitrate contamination begins during farming when fertilizers and manure containing nitrates are spread across fields to aid the growth of crops. After irrigating these fields, the crops absorb much of the nitrates from the fertilizer; however, a fraction of the nitrates is transported to creeks, rivers, and lakes through surface runoff, and a residual fraction of the nitrates remains in the vadose zone, leaching into the ground and diffusing deeper into the soil (Ward 2009, Clean Wisconsin 2022). This nitrate plume eventually reaches the groundwater and might move into private wells and systems that use groundwater for drinking water (WDNS 2022). Figure A.1 shows the estimated percentage of nitrate contamination over the standard for each county in Wisconsin as of March 2023 (UWSP 2023).

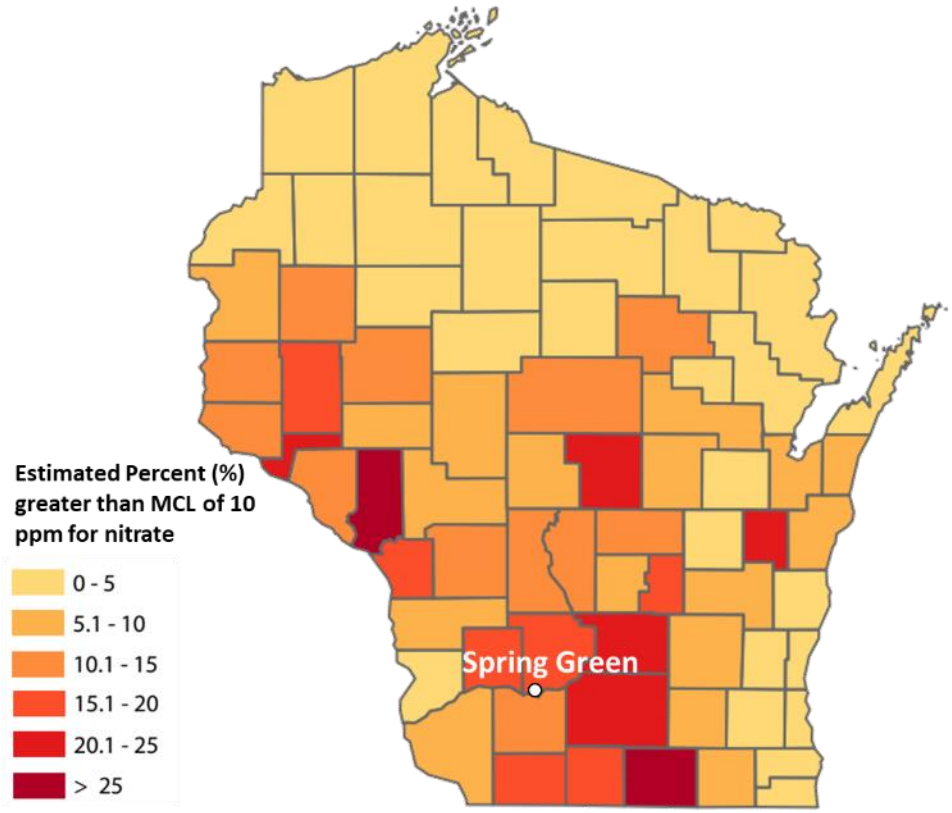

Figure A.1: Estimated percentage of private wells over nitrate standard by county as of March 27, 2023 (after UWSP 2023).

The vadose zone is the unsaturated soil and rock layer between the ground surface and the water table. It is a critical component of the hydrological cycle and is crucial in controlling the flow and fate of water, nutrients, and contaminants in the subsurface environment (Green et al. 2008). The pollutants enter the ground through a process known as infiltration. Infiltration occurs from natural precipitation or irrigation in farming practices (Figure A.2). The properties of the soil and input parameters dictate the transport process. These properties and input parameters include the distribution of grains and pore sizes, water content, organic content, rainfall intensity and

duration, and irrigation events. These characteristics influence the magnitude of infiltration by preventing or encouraging fluid transport through pore space, roots, or soil boundaries (Tindall et al. 1999). Therefore, understanding how processes occur in the unsaturated zone is essential for managing and protecting groundwater resources and controlling the fate and transport of contaminants.

Furthermore, the vadose zone is the first line of defense against contamination. As nitrates are retained and absorbed by soils in the vadose zone, fewer nitrates become available to contaminate the groundwater, improving the quality of drinking water in private wells. This research investigates the seasonal and short-term changes of different infiltration mechanisms in the vadose zone. We take a better look at the pathway of contaminants after an entire season of farming to provide a better understanding of the transport process of these contaminants and how they can lead the way to creating solutions to mitigate groundwater contamination.

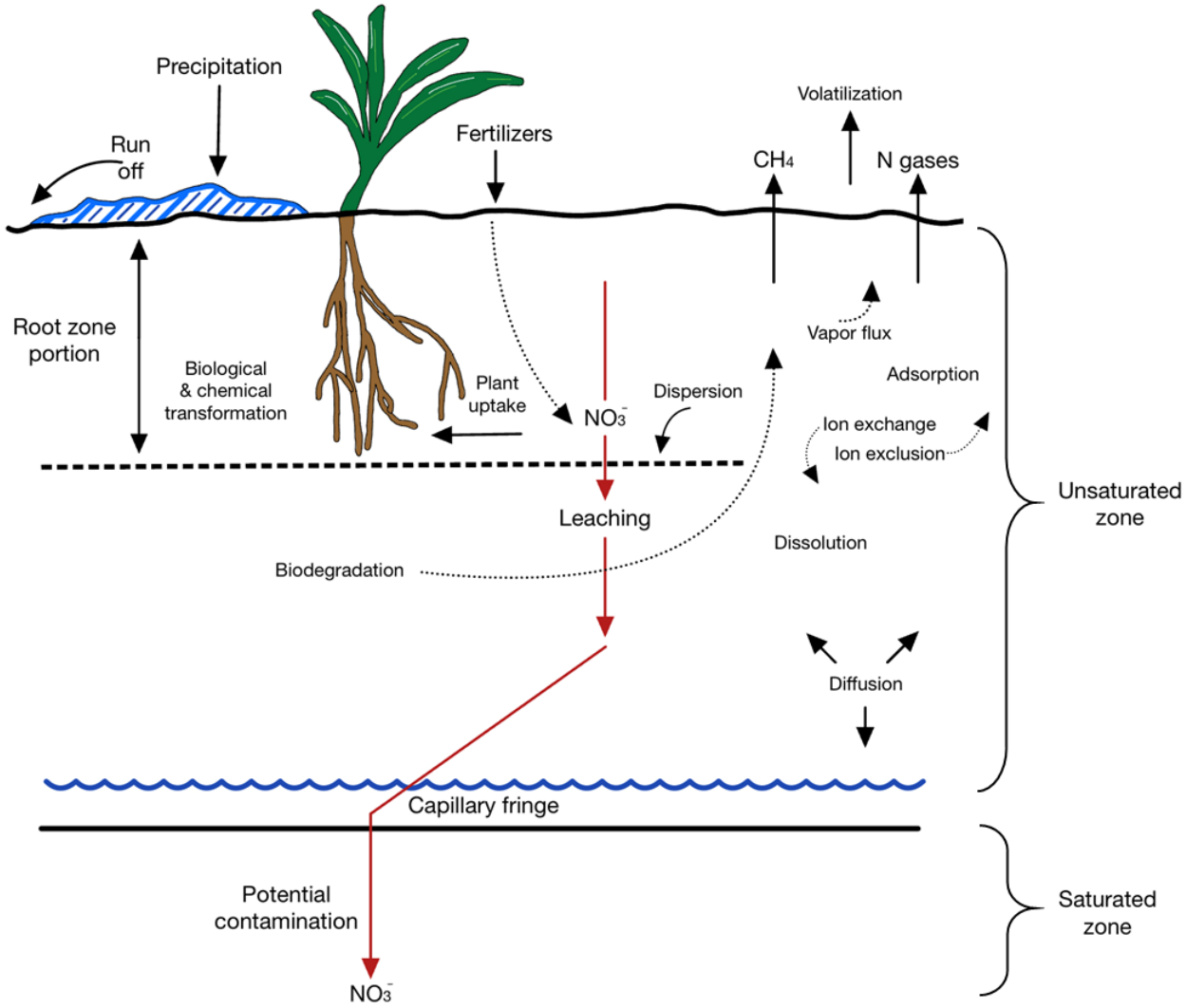

Figure A.2: The vadose zone and the infiltration processes around the root zone (after Tindall et al. 1999).

A.1.2 Site Description

The testing site for our study was a grassy area, not part of the cultivation area, near a farm field (Field 19) in southwestern Wisconsin on the Lower Wisconsin River Valley (Figure A.3). The Lower Wisconsin River Valley is characterized as an outwash plain because it originated from glaciofluvial sedimentary deposits composed mainly of sand and gravel. This geological

environment results from the region's location within the Driftless Area, an expansive land not previously covered by glaciers (Clayton and Attig, 1990). Clayton and Attig (1990) provide an extensive report on the geology of Sauk County.

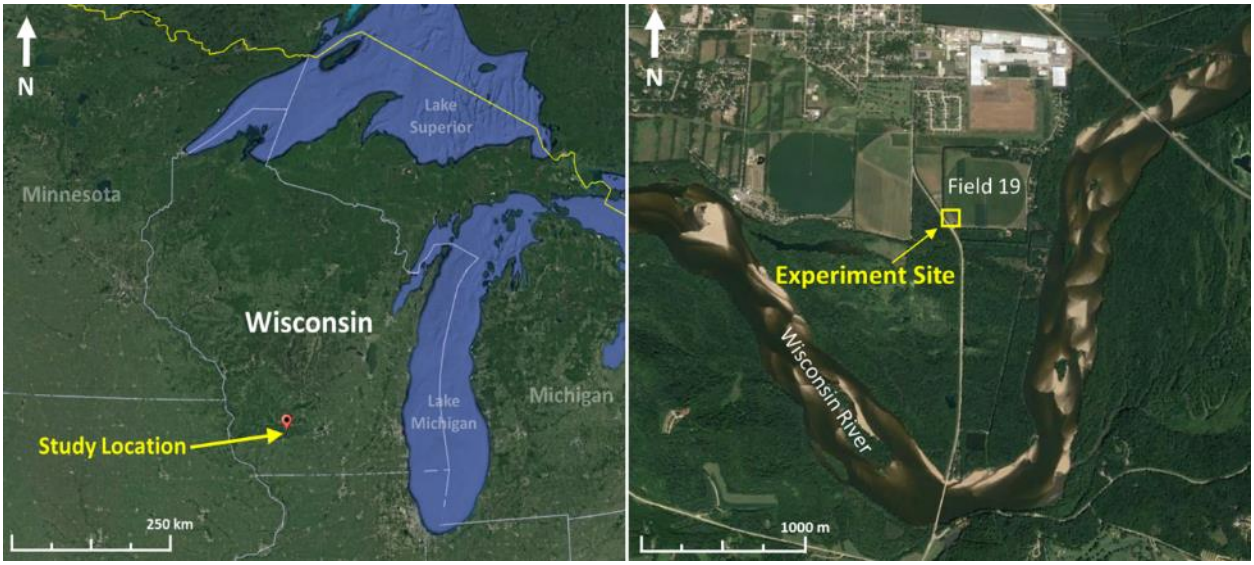

Figure A.3: The study location sits on a glaciofluvial outwash plain in the Lower Wisconsin River Valley. The experiment site is near the southwest edge of the farm field, Field 19 (after Google Earth).

The study area's shallowest bedrock lies at approximately 130 m below the surface and consists of Precambrian igneous and metamorphic rock, predominantly quartzite (Clayton and Attig 1990, Gotkowitz et al. 2005). The Paleozoic bedrock formations in the Elk Mound Group and the Trempealeau Group overlaying the Precambrian are mainly composed of alternating layers of sand, shale, sandstone, siltstone, and dolomite (Clayton and Attig 1990). These almost flat-lying layers make up about 275 m of rock before being overlain by Cenozoic sandy clay and glacial sediments (Gotkowitz et al. 2005 – Figure A.4).

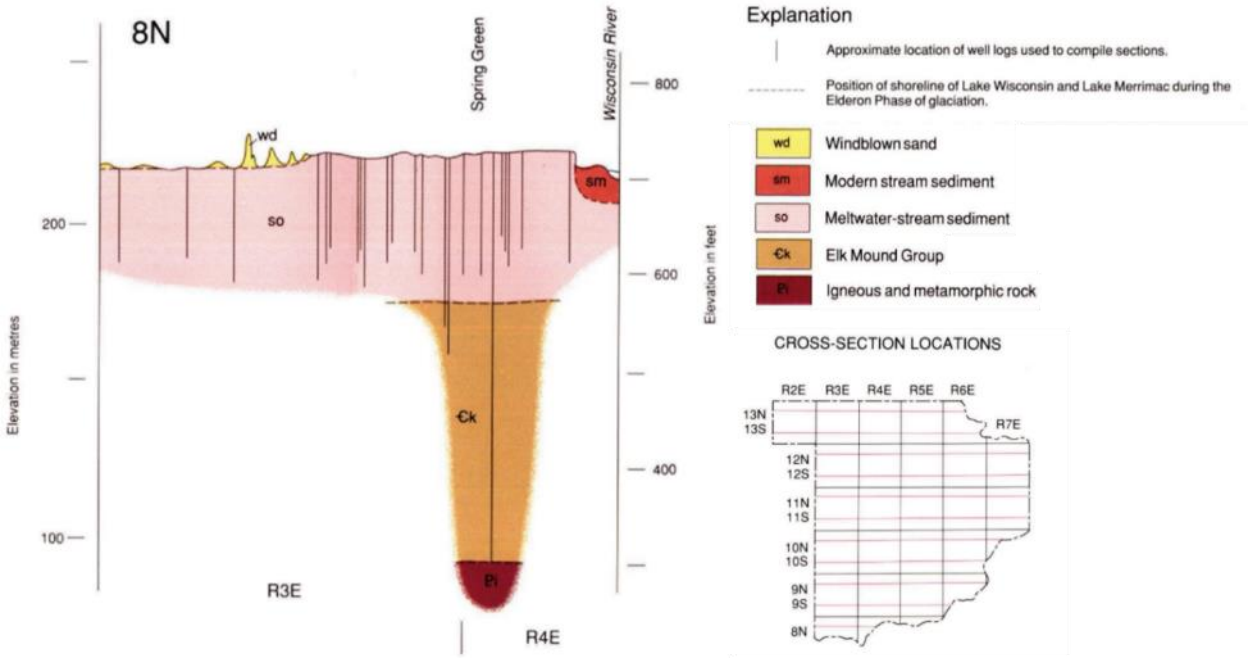

Figure A.4: Geologic cross-section near the study area using well logs (after Gotkowitz et al. 2005).

The floodplains of the LWRV are composed of nutrient-rich, organic alluvial soil ideal for agricultural practices (WDNR 2022). The USDA classifies the soil in the testing site as a Sparta loamy sand having 1 to 6 % slopes with a surface slope ranging from 0 to 3 % in the southern direction towards the Wisconsin River (Figure A.5). At the site, the typical soil profile is loamy sand from the surface to a depth of 40 cm, fine loamy sand from 40-76 cm, and sand from 76-152 cm. Four wells placed on the north, south, west, and east side of the field by Krause (2017) indicate a depth to the water table ranging between 2.3 and 2.4 m.

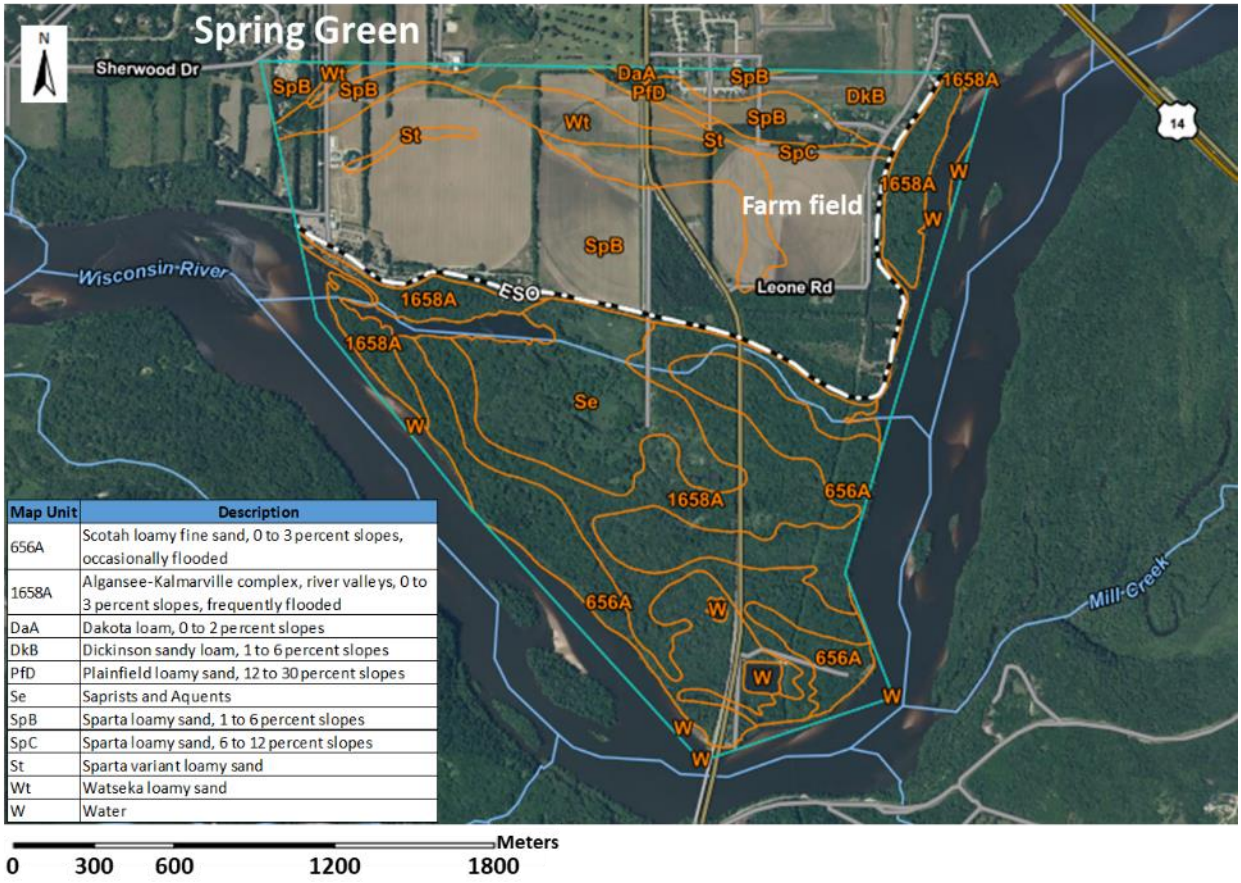

Figure A.5: Soil map for the area around the farm field in Sauk County, Wisconsin (after USGS Web Soil Survey 2023).

Field 19 is approximately 250,000 m^2 (25 hectares). The farming company rotates the types of crops every year (i.e., corn, potatoes, etc.), and the amount and type of fertilizers used during each season vary depending on the crop (Long, 2023). The fertilizers spread over Field 19 for each farming season contained an average between 443.6 ppm and 631.6 ppm of nitrogen. The irrigation schedule for the field can start as early as April and end as late as October every year, with an application of approximately 155-270 mm/m2 of water spread over the field annually. The National Oceanic and Atmospheric Administration (NOAA) reported a 30-year average precipitation of 865 mm/year at the site. However, the total amount of rainfall for the years 2020

to 2022 ranged from 590 to 956 mm/year, as seen in the summary for the farming seasons in Table A.1. Details about the fertilizers used for the 2020 and 2022 farming seasons can be found in Table A.5 in Appendix B.

Table A.1: Summary of seasonal agricultural data for Field 19.

Farming Season	**2020**	**2021**	**2022**
Precipitation[1] (mm/year)	956.1	589.5	791.5
Irrigation (mm/year)	155.7	269.2	151.1
Total volume of irrigation (kL)	12,918	9,573	9,404
Total N kg/ha	230.3	-	238.6
The concentration of nitrogen in total fertilizer added to Field 19 (ppm)	443.6	-	631.6

[1]Precipitation yearly totals from NOAA (ncei.noaa.gov)

A.1.3 Previous Studies at the Site

Cates (1991), Gotkowitz et al. (2005), and Krause (2017) studied the near-surface hydrogeology of the Lower Wisconsin River Valley, including our testing site. We selected the study site for its assumed near-surface homogeneity. The Cates (1991) study collected samples from approximately 78 Lower Wisconsin River Valley wells, including two wells in Spring Green that tested positive for nitrate contamination with concentrations ranging from 19 to 25 ppm. At the same time, Gotkowitz et al. (2005) identified that more than 14% of the 1,430 wells samples in Sauk County exceeded the MCL of 10 ppm for nitrate. Finally, Krause (2017) reported that over 75% of the monitoring wells also exceeded the MCL of 10 ppm for nitrate. The nitrate contamination in the north well of his study was consistently above the MCL despite being up-gradient from Field 19, suggesting that the contamination may be coming from other land uses

up-gradient. The wells have an average pump capacity of 42 L/s and sit above a sandstone/unlithified aquifer (Cates 1991, Gotkowitz et al. 2005).

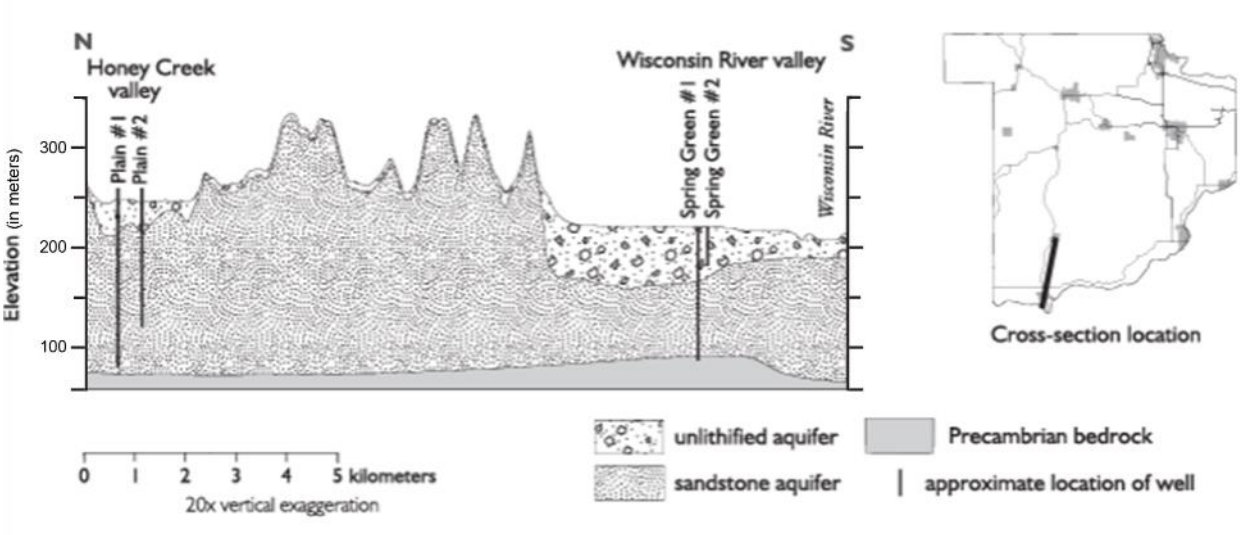

Figure A.6: Cross-section of the geologic composition of underlying aquifers near the study site in Sauk County, WI (Gotkowitz 2005).

The unlithified aquifer underlying this outwash area consists of glacial and alluvial sediments that mainly vary from sand and gravel and clayey till and lake sediments closer to the Wisconsin River (Gotkowitz et al. 2005). This deposit can be as thick as 60 m (Figure A.6) and is highly permeable, with measured hydraulic conductivity measurements ranging from 16 to 300 m/day (Gotkowitz et al. 2005). However, no aquitard separates the underlying sandstone and the unlithified aquifer in multiple areas near the Lower Wisconsin River Valley. Because of this, the aquifers typically have similar hydraulic properties. In addition, Krause (2017) reported hydraulic conductivity measurements at the edges of Field 19 near our study site that ranged between 15 m/day and

75 m/day. Therefore, Krause (2017) suggested that the hydraulic conductivity of Field 19 is relatively high and homogenous.

A.2. Methodology & Testing

2.1 Flow in Unsaturated Media

Hydraulic conductivity, K_{sat}, is an essential property of saturated soils that describes its ability to transmit water at 25°C when saturated. Darcy's law (A.1) models the water flow rate, *Q*, through an isotropic porous medium, where *A* is the medium's cross-sectional area, and *i* is the hydraulic gradient (i.e., the change in total head over the flow path) in a prismatic or cylindrical soil specimen:

$$Q = -K_{sat} i A \qquad A.1$$

However, Darcy's law is only applicable under the assumption of laminar flow in a saturated media, which is a typical flow behavior through saturated fine-grained sediments. To account for the empty pore space and different types of flow through various sediments in unsaturated media, Buckingham (1907) extended Darcy's Law to include that the unsaturated hydraulic conductivity increases with volumetric water content, θ. Darcy-Buckingham's law models this response (Anderson and Woessner 1991, Ochsner 2019, Tindal et al. 1999):

$$q = -K_{unsat}(\theta)\frac{dH}{dz} \qquad A.2$$

where q is the flux density of water, K_{unsat} is the unsaturated hydraulic conductivity and dH/dz is the total water potential gradient in the z-direction.

Since multiple parameters affect fluid flow depending on the properties of the soil medium, calculating the flow in an unsaturated medium is a dynamic process (Nimmo 2005). Because of this, the Darcy-Buckingham law is often combined with the continuity law to create Richard's equation. In addition, Farthing and Ogden (2017) described Richard's equation as a function of the water content, where $D(\theta) = K(\theta)(\partial\psi(\theta)/\partial\theta)$ is the soil-water diffusivity obtained from a water retention curve, z is the distance from one end of the column, and t is time.

$$\frac{\partial\theta}{\partial t} = \frac{\partial}{\partial z}\left[D(\theta)\frac{\partial\theta}{\partial z} - K_{unsat}(\theta)\right] \qquad A.3$$

Since the water content varies with depth and soil type, Richard's equation expands on the limitations implemented using Darcy's law (Tindal et al. 1999).

Much of the transport processes in the unsaturated zone occur through preferential paths like fingers or small pockets of increased moisture, fractures, root holes, or even wormholes created by invertebrates or insects (Nimmo 2005). Determining the hydraulic conductivity is just one crucial step in evaluating the transport of a contaminant in the unsaturated zone.

A.2.2 Infiltration Setup

To simulate rainfall events that recharge the groundwater, short-term and seasonal infiltration experiments were conducted to permeate fluid into the vadose zone of the soil. Initial infiltration experiments (Swager 2021) using an infiltrometer were done in multiple areas on the study site (Figure A.7) with varying volumes of a 0.025 M sodium bromide solution to simulate different recharge events.

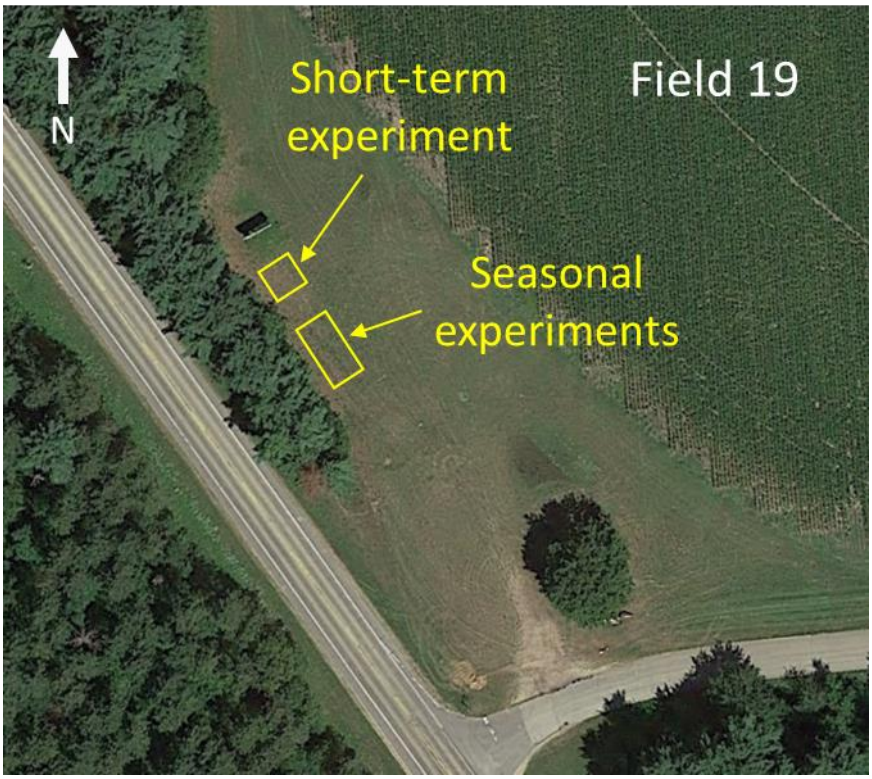

Figure A.7: Location of infiltration experiments on the southwest edge of Field 19.

We deployed an infiltrometer to measure the soil's ability to transmit water. Infiltrometers are commonly used to assess transport processes in soil and hydraulic properties of both unsaturated and saturated zones (Angulo-Jaramillo et al. 2000, Cey and Rudolph 2009, Lassabatere et al.

2019). In our experiments, we used a constant head, single-ring infiltrometer. The constant head infiltrometer method assumes that the water level in the reservoir remains constant during the experiment and that the water flow rate into the soil is also constant. The infiltrometer consists of a vertical cylinder with a constant head reservoir on top and an outlet pipe at the bottom (Figure A.8).

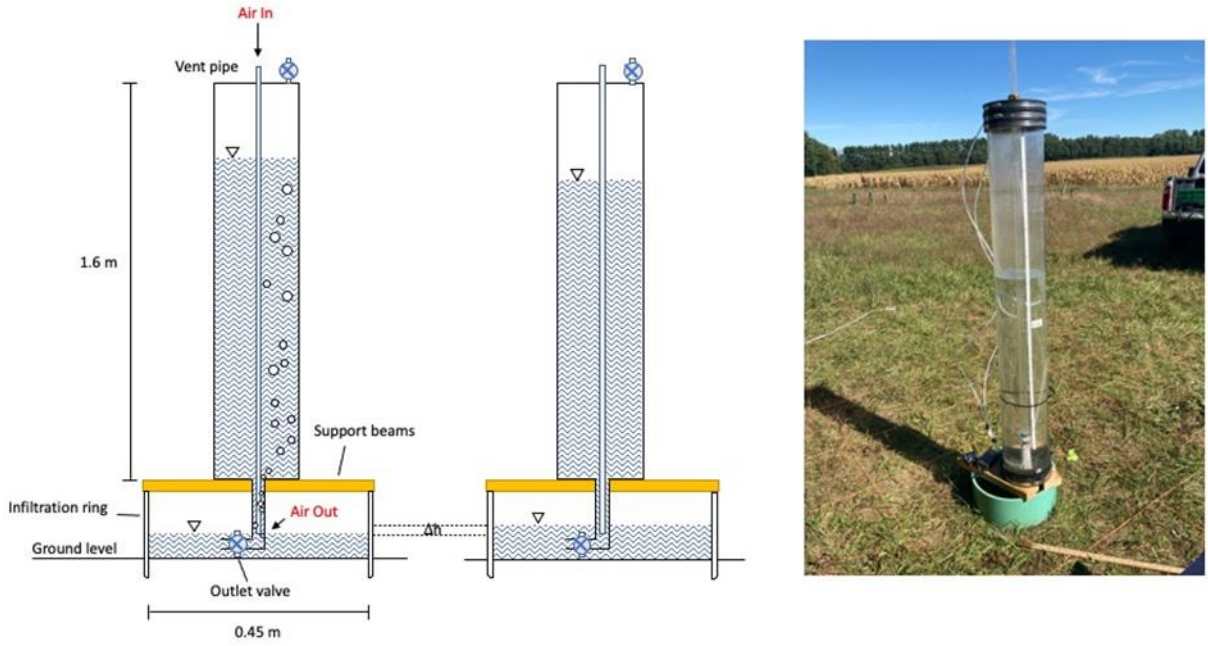

Figure A.8: The setup and design of the infiltrometer and the infiltrometer demonstrated in the field (Swager 2021).

A sodium bromide tracer solution was used throughout this experiment because sodium bromide does not typically absorb onto soil particles, has low toxicity, and its concentration is naturally low in soil and groundwater (Davis et al. 1980, Flury and Papritz 1993, Wilderer et al. 2011). Because salt-based tracers are inorganic compounds, the cations and anions composing the compounds dissolve in water. Bromide ions in the sodium bromide salt also have significantly

lower background concentrations (approximately 300 times less) than that of chlorine ions, which is part of another commonly used hydrology tracer, sodium chloride (Wilderer et al. 2011).

To begin the infiltration experiment, we placed the infiltrometer over a constructed cylindrical or square frame driven slightly into the ground to prevent water from escaping the enclosed area. We then filled the infiltrometer tank with the sodium bromide solution before opening the valve at the bottom of the infiltrometer, releasing the solution to allow seepage into the soil. As the level of sodium bromide solution in the infiltrometer decreases to the elevation of the vent tube outlet, air enters the infiltrometer's reservoir to allow the continuation of flow. Finally, we recorded the elapsed time every 5 cm as the elevation of the solution decreased. Table A.2 describes the parameters for each experiment discussed in this study. While the infiltration lasted similar amounts of corrected times, we labeled one set of experiments as "seasonal experiments" and the other as "short-term experiments" due to the time we spent monitoring the responses.

Table A.2: Parameters for infiltration experiments near Field 19.

	Seasonal experiments		Short-term experiment
Experiment Date	October 2020	April 2021	August 2022
Experiment Duration	1 year	5 months	72 hours
Volume of NaBr Solution Infiltrated (L)	76	76	40
Recharge Simulation (mm)	95	95	50
Infiltrometer Boundary Type	Ring	Ring	Square
Boundary Dimensions	0.4 m diameter	0.4 m diameter	1 m by 1m
Boundary Area (m^2)	0.13	0.13	1.00
Height Above Ground Surface (cm)	5	8	6
Time to Infiltrate (min)	201	148	117*
Cumulative Precipitation 10 days prior[1] (mm)	117.6	0.76	79.8
Hydraulic Conductivity (m/day)	8.4	7.1	14.4

[1]Precipitation data from Weather Underground (wunderground.com), Station ID: KWISPRIN5
*Value normalized to match different parameters for infiltration (calculation in Appendix A).

For the short-term infiltration experiment, a green food-based dye was added to the sodium bromide solution before infiltration to create a color-dyed solution safe for seepage into the soil. After completing the infiltration experiment and collecting all planned data for the 72-hour monitoring period of the short-term experiment, we used a backhoe to dig a soil pit west of the infiltration center. The objective for the soil pit was to observe dye infiltration, evaluate the presence of fingering, and obtain additional soil samples.

A.2.3 Physical Testing

Physical analyses were done on multiple soil samples in the testing area to determine if there was any evidence of fine-scale heterogeneities. In addition, physical soil characterization could

help us determine the influences governing the potential retention or transport of the injected sodium bromide solution.

A.2.3.1 Grain Size Distribution

The particle size distribution of soil is practical for classifying soils, and it also controls the speed of fluid traveling through a medium (Murthy 2002, PGC 2014, and ASTM 2014). A grain size distribution curve can emphasize the characteristics of specific grain sizes, such as the effective grain size, D_{10}, which corresponds to the diameter of the particles at 10 percent finer on the curve. Hazen (1893) uses this variable to correspond a relationship with the uniformity coefficient, C_u, and D_{60}, known as Hazen's Rule:

$$K = C_u \frac{g}{\nu} (D_{10})^2 \qquad A.4$$

This rule is commonly used to approximate the hydraulic conductivity of sandy soils, where C_u is the uniformity coefficient ($C_u = D_{60}/D_{10}$), D_{60} is the particle diameter at 60 percent finer on the grain size distribution curve, $g = 9.81\ m/s^2$ is the acceleration of gravity, and $\nu = 0.89 \times 10^{-6}\ m^2/s$ is the kinematic viscosity of water at 25°C.

The *ASTM Standard Test Method for Particle-Size Distribution (Gradation) of Soil Using Sieve Analysis* was used to determine the percentage of different-sized grains in the samples. A sieve set that includes size sieves No. 4, 10, 20, 40, 60, 100, and 200 was used to separate each soil fraction. The finer material passing the No. 200 sieve and the material retained at each sieve

were weighed to determine the mass of each particle size. The mass for each was then used to calculate the percent passing through each sieve, represented by a grain size distribution curve.

A.2.3.2 Hydrophobicity

Hydrophobicity is the measure of water repellency on the surface of a material (Olorunfemi 2014). The Water Drop Penetration Time (WDPT) method is one of the most common standard methods used in the lab to measure hydrophobicity (Doerr 1998). This method involves placing a water droplet on a smoothed, oven-dried surface without any organic debris and recording the time it takes to penetrate the soil thoroughly. If the droplet penetrates instantly, the soil is considered hydrophilic. However, if the droplet remains on top of the soil without penetration of the sample, it is considered hydrophobic. Then, the soil's surface tension is less than the water droplet. Since hydrophobic soils repel water, this can decrease the amount of water retention in soil, damage the flow of streams from increased erosion and runoff, and reduce plant growth (NRCS 2000). Because of the consequences of the soil becoming hydrophobic, it is another essential aspect to study to help further identify the infiltration mechanisms.

Approximately 15 to 20 g of each soil sample was placed in a ceramic dish and lightly patted to flatten the surface. Five drops were placed with a pipette in the middle and around the sample (Figure A.9). After each drop was placed, a timer was set to determine the penetration time.

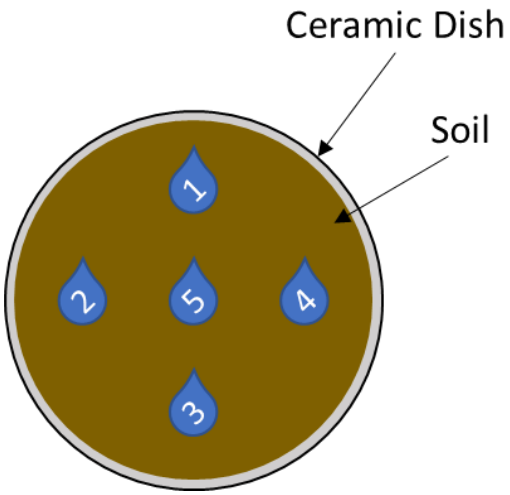

Figure A.9: Setup for hydrophobicity testing. The surface was flattened to help observe the absorption of the water droplets on the dry soil samples.

A combination of threshold WDPT times from the research of various authors (Table A.3) was used to determine the hydrophobicity classification at various depths of each core sample.

Table A.3: Threshold from various authors of Water Drop Penetration Test (WDPT) times used to classify soil repellency (Doerr 1998).

Classification	**Adams et al. (1969)**	**Bisdom et al. (1993)**	**Doerr et al. (1996)**	**Ma'shum & Farmer (1985)**	**McGhie & Posner (1981)**	**Roberts & Carbon (1971)**
	Time (seconds)					
Hydrophilic	< 10	< 5	< 60	< 1	< 60	< 1
Slightly hydrophobic	10 - 60	5 - 60	-	-	-	1 – 10
Strongly hydrophobic	-	60 – 600	-	-	-	10 - 60
Severely hydrophobic	> 60	600 - 3600	-	-	-	> 60
Extremely hydrophobic	-	> 3600	> 3600	-	-	-

A.2.3.3 Loss on Ignition

Organic matter in soils usually increases the pore volume and the hydrophobicity of soil, changing the soil's ability to retain and move water (Bot and Benites 2005). One of the most common methods to quantify soil's organic content loss-on-ignition (LOI). According to the ASTM D7348-21 standard, this method involves heating a sample in an oven to 260°C to remove or "burn off" the organic material in the sample. Approximately 15 to 20 g of soil from each sample was placed in ceramic crucibles (Figure A.10). The mass of the sample was measured before going into the oven and then stirred midway through the 24-hour process to ensure an even heat distribution.

After 24 hours, the mass of the sample is measured again to determine how much organic content burned off. The LOI was then calculated using A.5, where m_1 is the mass of the sample before heating and m_2 is the mass of the sample after heating.

$$LOI = 100\frac{m_1 - m_2}{m_1} \qquad A.5$$

This process was done for a representative soil core sample located in the infiltration testing area, with a sample situated approximately 50 m northwest and upward from the infiltration testing area to observe how the organic content changes with depth.

Figure A.10: Representative soil sample from 10-cm interval prepared for LOI testing.

A.2.4 Near-Surface Geophysics

Geophysical techniques allow for the non-destructive imaging of the near-surface. We used Ground Penetrating Radar and Electrical Resistivity Tomography surveys in our study to monitor how the directional movement of the plume created from the infiltration of the sodium bromide solution changes over time. Since these methods are sensitive to the parameters in our study (i.e., changes in dielectric permittivity and electrical conductivity), they can sense changes in the water content and pore fluid concentrations, giving us a better look at the near-subsurface processes.

2.4.1 Electrical Resistivity Tomography

Electrical Resistivity Tomography (ERT) was used to observe the changes in the resistivity of the near-surface soil during the infiltration study throughout all experiments. ERT is a geophysical method used to image the electrical resistivity distribution of the near-surface soil and rocks. This technique injects an electrical current into the ground through two metal electrodes, creating a voltage field around each electrode (ERT 2020). At the same time, another pair of electrodes picks up the voltage difference across different electrode pairs on the boundaries of the medium. This process repeats for a large combination of pairs of current and voltage electrodes (Figure A.11).

A dipole-dipole array (Figure A.12) was used in our study because this array typically has a better horizontal resolution and coverage of depth at each end of the array. The resolution quality produced from this array results from the small-scale spacing between electrodes, which creates an array line that acts as a single electric field (Neyamadpour et al. 2010, AGI 2017).

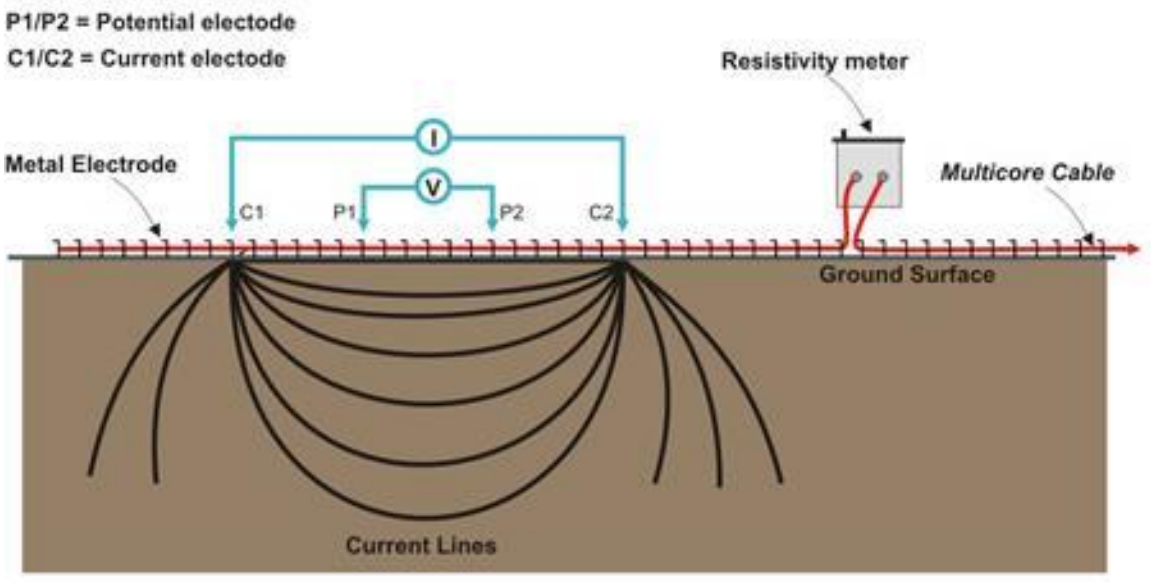

Figure A.11: General resistivity principle of electrical resistivity tomography (after ERT 2020).

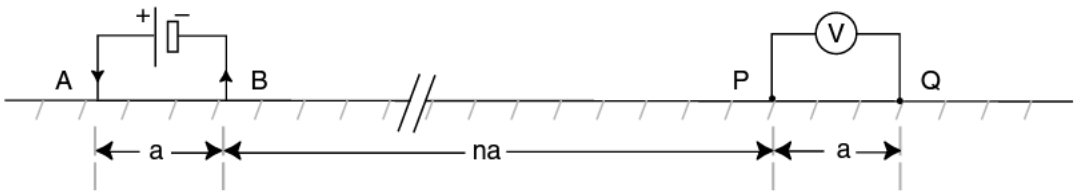

Figure A.12: Arrangement of a Dipole-Dipole array (Everett 2013).

The resistivity of a material, ρ, is the quantitative measurement of how well a material resists the flow of electricity (Witten 2014). The reciprocal of the resistivity is the electrical conductivity, which indicates a material's ability to sustain electric flow. Therefore, electric current is lower in high-resistivity and high in low-resistivity mediums (Everett 2013). Using the notation presented in Figure A.12, the voltage, V, measured across P and Q is calculated by:

$$V = V_P - V_Q = \frac{I\rho}{2}\left[\frac{1}{r_P} - \frac{1}{r_Q}\right] \qquad A.6$$

where I is the electric current, r_P is the distance from the current source to the electrode at P, and r_Q is the distance from the current source to electrode Q. However, A.6 assumes a homogeneous electrical resistivity distribution below the Earth's surface (Everett 2013, Witten 2014). Because most near-surface materials are not homogeneous, the measured resistivity is called the apparent resistivity, ρ_a. The apparent resistivity represents the weighted average of resistivities in a four-electrode configuration and can be computed by:

$$\rho_a = \frac{2\pi V}{I}\left[\frac{1}{r_{AP}} - \frac{1}{r_{AQ}} - \frac{1}{r_{BP}} + \frac{1}{r_{BQ}}\right]^{-1} = kZ \qquad A.7$$

where *k* is the geometric factor of a specific array, *Z* is the earth's impedance ($Z = V/I$), and r_{ij} is the respective distance between the current sources and electrodes in Figure A.12. The geometric factor, *k*, captures the weighted value of the apparent electrical resistivity measurement depending on the type of array used (Everett 2013). The geometric factor for the dipole-dipole array is:

$$k = \pi n(n+1)(n+2)a \qquad A.8$$

where n is the separation factor greater than 1, and a is the distance between the electrodes. Therefore, the apparent resistivity for a dipole-dipole array can now be expressed as:

$$\rho_a = \pi n(n+1)(n+2)a\frac{\Delta V}{I} \qquad A.9$$

The apparent resistivities of the soil obtained from the ERT survey can then be used to create pseudo sections representing the relative distribution of the near-surface Earth resistivity. This is done by plotting the measured apparent resistivities at the intersection of two lines oriented at a 45-degree angle to the ground surface and passing through the center of the respective electrode pairs. The process is repeated for all current and potential electrode pairs, resulting in a figure that displays the contouring of the apparent resistivity data and helps interpret the results. A trapezoidal shape indicates that the measured data have minimal sensitivity to the ground structure in the two triangular regions beneath the first and last set of current or potential electrodes. The maximum sensitivity to the ground structure is typically found near the midpoint of the four-electrode configuration, at a depth approximately halfway between the current and potential electrode pairs (Everett 2013, Witten 2014).

A.2.4.2 ERT Survey Configuration

The electrode configuration for the continued seasonal monitoring of the initial infiltration experiments done by Swager (2021) consisted of two lines of 18 electrodes set in the north-to-south and west-to-east directions, with the infiltration area being the center-point of each line (Figure A.13).

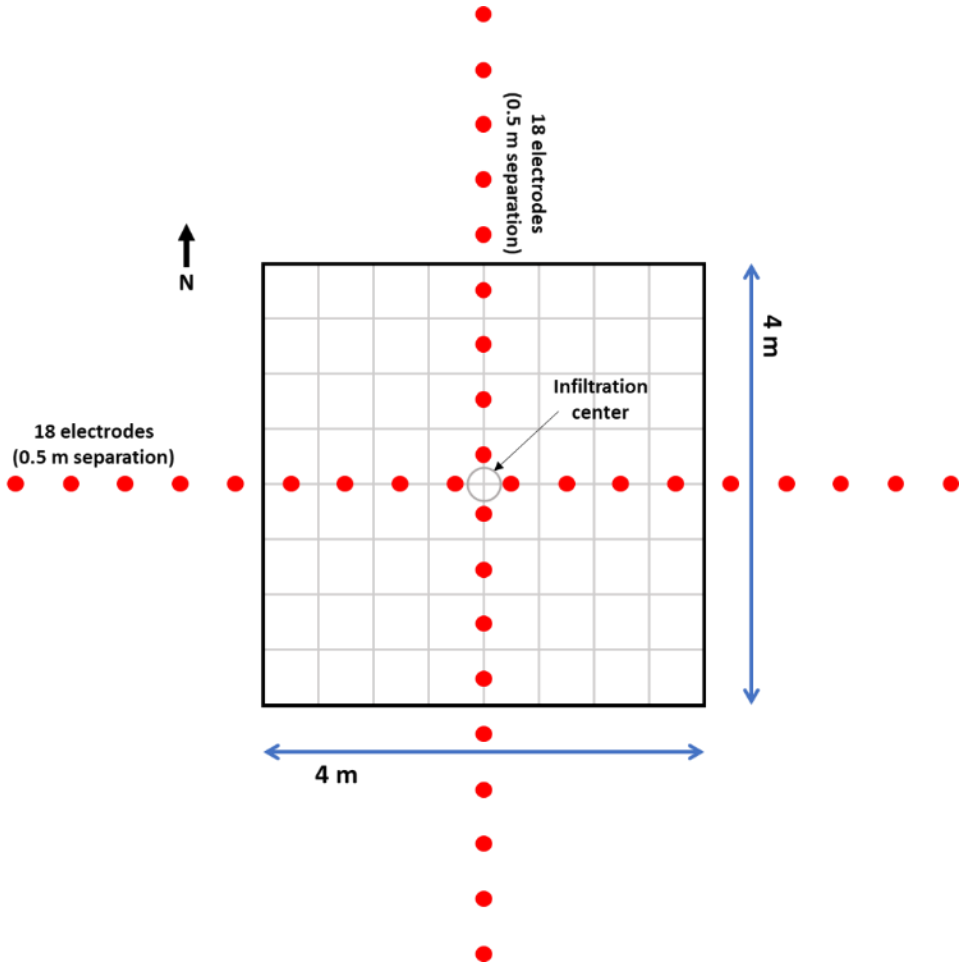

Figure A.13: Electrode configuration and orientation of the ERT surveys done for each infiltration experiment.

Stainless steel electrodes were driven about 10 cm into the ground with a separation of 0.5 m and connected using a multicore cable (Figure A.14). Measurements from each line were taken using a Syscal Kid Switch-24 electrical resistivity tomography system. The apparent resistivity data captured from the instrumentation was inverted using the Geotomo RES2DINV software to estimate the electrical resistivity distribution in the medium. We used the same settings shown in Table A.4 to align with the initial ERT surveys from Swager (2021).

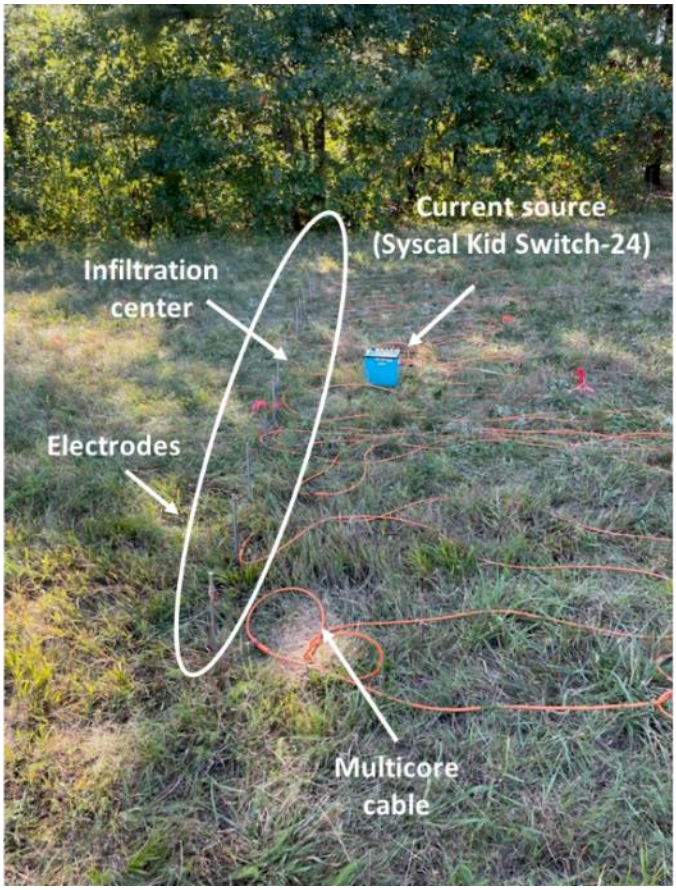

Figure A.14: Field setup for the ERT survey lines near Field 19.

Table A.4: Modified settings[1] used when running the data inversions from the ERT surveys in the RES2DINV software (after Swager 2021).

Damping Parameters	
Damping factor	Initial factor 0.15, increase w/ depth by 1.05 Minimum factor 0.03
Limitation of model resistivity	Model resistivity values cannot exceed between 0.3 and 3.0 times the 1st iteration values.
Forward Modeling Settings	
Type	Finite-difference
Mesh size	Finer
Inversion Progress Settings	
Convergence limit	5
Number of iterations	4
Inversion Method and Settings	
Robust inversion	Yes
Time-lapse inversion	Smoothness constraint
Smoothness constrained least-squares	Applied to model change vector
Least-squares solution	Incomplete Gauss-Newton
Model refinement	Model blocks are half the unit electrode spacing.

[1] Setting names refer to the Geotomo RES2DINVx64 version 4.9.18 software.

A.2.4.3 Ground Penetrating Radar

Ground Penetrating Radar (GPR) is a geophysical technique that uses reflected electromagnetic waves to create subsurface images. It is commonly used in geologic investigations to determine the location and properties of buried objects, structures, materials, subsurface cavities, and heterogeneities in the soil (Utsi 2017). The propagation of electromagnetic waves used in GPR senses the electrical conductivity and permittivity of the subsurface. The components of a GPR system include transmitting and receiving antennas, usually at a fixed distance, that are moved simultaneously across the ground surface. Short pulses of high-frequency electromagnetic energy are sent through the transmitting antenna and propagated into the ground. These pulses are then reflected, refracted, or scattered by subsurface features with contrasting electromagnetic properties, such as those associated with changes in soil or rock types, buried

structures, or water tables (Haeni et al. 1987, Everett 2013, Witten 2014). The receiving antenna captures the direct, reflected, and refracted signals. The interpretation of the signals allows determining the travel time, t, of the reflected waves created from subsurface interfaces and anomalies, and by knowing the speed of the wave through the medium, c_1, and the total distance traveled, 2d, from the transmitting antenna to the interface to the receiving antenna.

$$t = \frac{2d}{c_1} \qquad A.10$$

As the GPR system moves along the survey line, this process is repeated, resulting in multiple travel times for various distances along the survey line. In addition, the waves travel at different speeds through the soil depending on the distribution of dielectric properties of each interface (Jol 2009). These received signals are then plotted as traces on a radargram in real-time using the survey's elapsed time and the antenna pair's horizontal locations. Since these signals mainly rely on soil permittivity, heterogeneities in the subsurface can be inferred at different depths (Witten 2014, Liu et al. 2017). The radargram can then be converted from time to depth to model the results of a subsurface profile (Figure A.15).

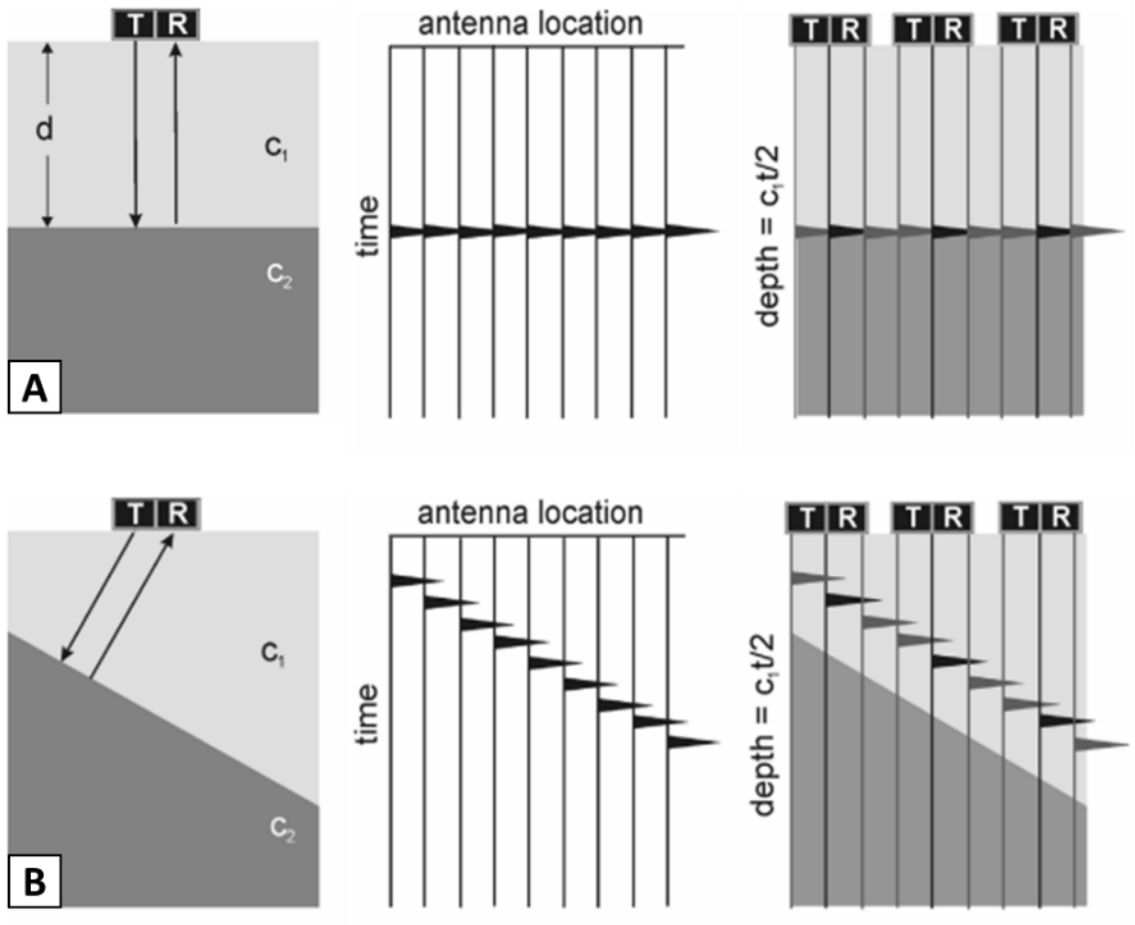

Figure A.15: A) Example of the concept and results created from a GPR system for a horizontal interface and a B) sloping interface. The radargram is converted from time to depth to model the subsurface (after Witten 2014).

Because the transmitting and receiving antennas are assumed to be acting at a point, the amplitude of the waves attenuates with distance, potentially reducing the range of frequencies that can pass through the system (Annan 2005, Jol 2009, Witten 2014). This is one of the reasons why selecting the antenna frequencies is essential while conducting GPR surveys. Different antenna frequencies are used to reach varying depths or achieve different resolutions depending on the soil conditions. Lower frequencies are generally used for deeper surveys but produce a lower resolution, while higher frequencies are used for shallow and subsurface investigations and

produce a higher resolution (Jol 2009, KBGPR 2023, S&S 2023). The GPR results are processed and analyzed to create two-dimensional or three-dimensional subsurface images. This geophysical survey method was used throughout the experiments to assess the soil permittivity directly below and around the injection site of each infiltration experiment.

A.2.4.4 GPR Survey Configuration

GPR survey lines were run north-to-south and west-to-east directions for each infiltration experiment near Field 19. The instrument used was the GSSI GPR with a 500 MHz antenna. The instrument ran down 2 m on either side from the center of the infiltration area with additional lines running through the center and 0.5 m from the center of the infiltration area (Figure A.16). However, in this document, we only present and analyze traces through the center of the infiltration zone. Appendix B presents the complete dataset.

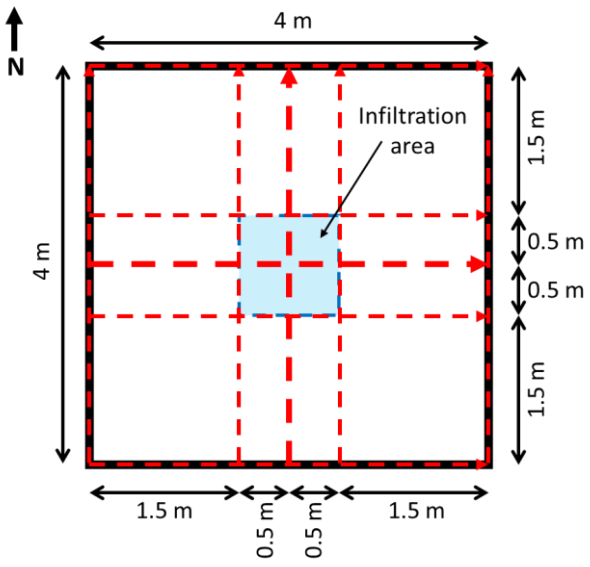

Figure A.16: Example of the GPR configuration for the infiltration experiments near Field 19. The red lines with arrows indicate the direction the GPR traveled during the testing.

A.2.5 Chemical Testing

Chemical analyses of the soil samples collected at our study site were necessary to determine the presence of the contaminant solution in the subsurface from the infiltration experiments. In addition, the soil water chemistry of the samples was also tested for nitrate contamination at various times throughout the farming season to help understand the long-term concentration changes with depth.

A.2.5.1 High-Performance Ion Chromatography

High-Performance Ion Chromatography (HPIC) measures the concentration of ionic components in a solution. In our study, we used HPIC to measure the nitrate and bromide concentrations in the pore fluid of soil cores collected after infiltration of the sodium bromide solution.

HPIC is a process that separates ions in a solution by distributing the sample molecules between two phases using a liquid chromatography ion exchange method (Weiss 2004). This analytical technique separates ionic compounds in a solution based on their electrically charged groups by establishing an equilibrium between each chemical component's mobile and stationary phases as they go through a separator column (Haddad and Jackson 1990). When the solution is injected into the column, components of a sample enter the mobile phase at different times depending on their solubility in the mobile phase and their strength to stay in the stationary phase. Due to varying solubilities and strengths, some sample components will pass through the mobile phase faster than others.

One of the most critical terms in determining the resolution of the component in a chromatographic analysis is the retention factor, $\left(k_f = (t_R - t_0)/t_0\right)$, i.e., the ratio of the retention time of a component in a column, t_R, to the retention time of a component in the stationary phase, t_0. The retention factor controls the quality of the separation of components in a solution. Other factors that are important in determining the resolution are the selectivity factor $\left(1/4\sqrt{N}\right)$ and the efficiency factor $\left((\alpha - 1)/\alpha\right)$, where $N = 16(t_R/W)^2$ is the plate number of a separator column based on the peak width, W, at a specific retention time of an ion and $(\alpha = k_2/k_1)$ is the separation factor responsible for chemically distinguishing between different components using the ratio of the retention factors between two peaks of differing ions, where k_1 and k_2 are the retention factors of two consecutive components. To determine the resolution, R_s, between two peaks of differing ions, the average retention factor, k_{avg}, is used.

$$R_S = \left(\frac{k_{avg}}{1 + k_{avg}}\right)\left(\frac{\alpha - 1}{\alpha}\right)\left(\frac{1}{4}\sqrt{N}\right) \qquad A.11$$

Combining the retention, selectivity, and separator factors for multiple ions in a solution creates the chromatogram (Figure A.17) (Fritz and Gjerde 2000).

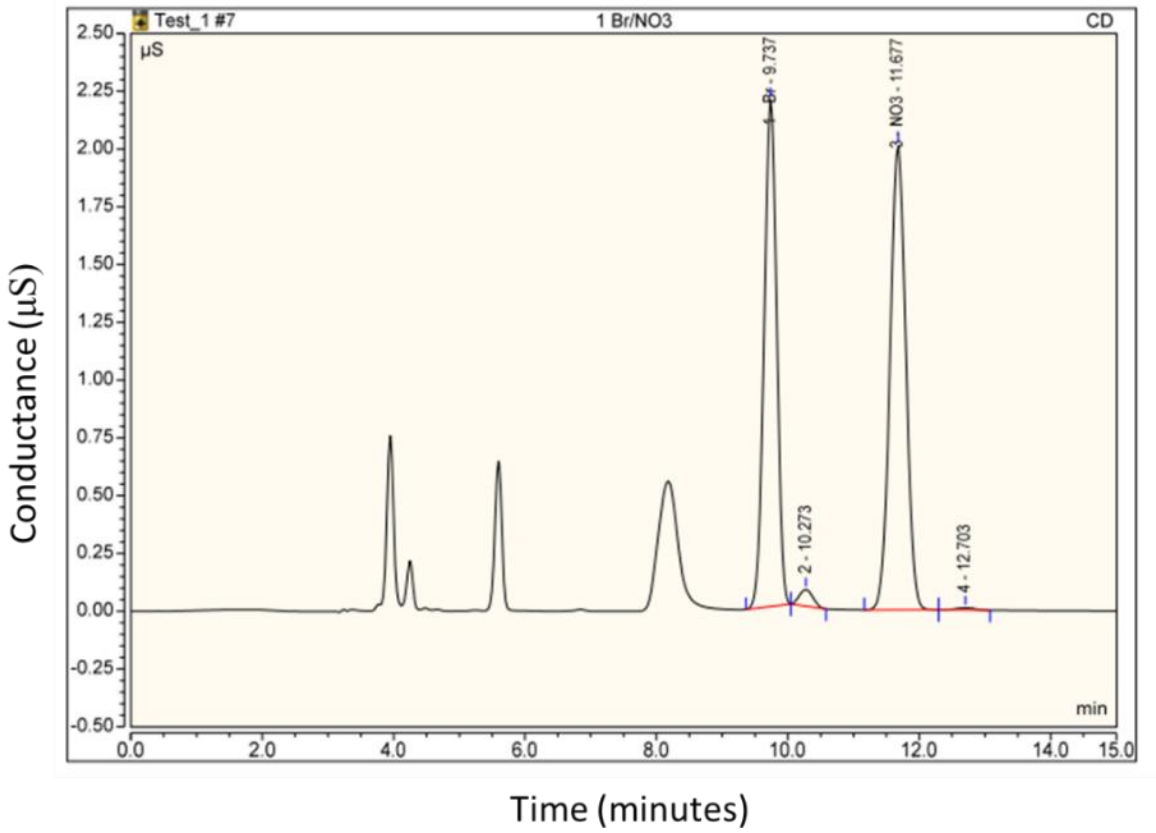

Figure A.17: Example of an ion chromatogram from the HPIC results of a soil sample in our study site. Peaks are identified using the prepared range of calibration standards for NO_3 and Br. Unidentified peaks are other ions within the sample.

A.2.5.2 HPIC Sample Preparation

Approximately 2-meter-deep soil cores were taken at various times after infiltration in multiple directions from the center of the infiltration area throughout the experiment (Figure A.18). The cores were then divided into 10-cm intervals to monitor the changes in bromide and nitrate concentrations with depth. Approximately 1 ± 0.08 g of soil from each interval was mixed with 10 mL of distilled water and filtered through a 0.45 µm filter to produce a liquid representative from the soil sample (Figure A.19). This process ensured that liquid samples with a maximum particle size of 0.45 µm did not damage the ion chromatography instrument.

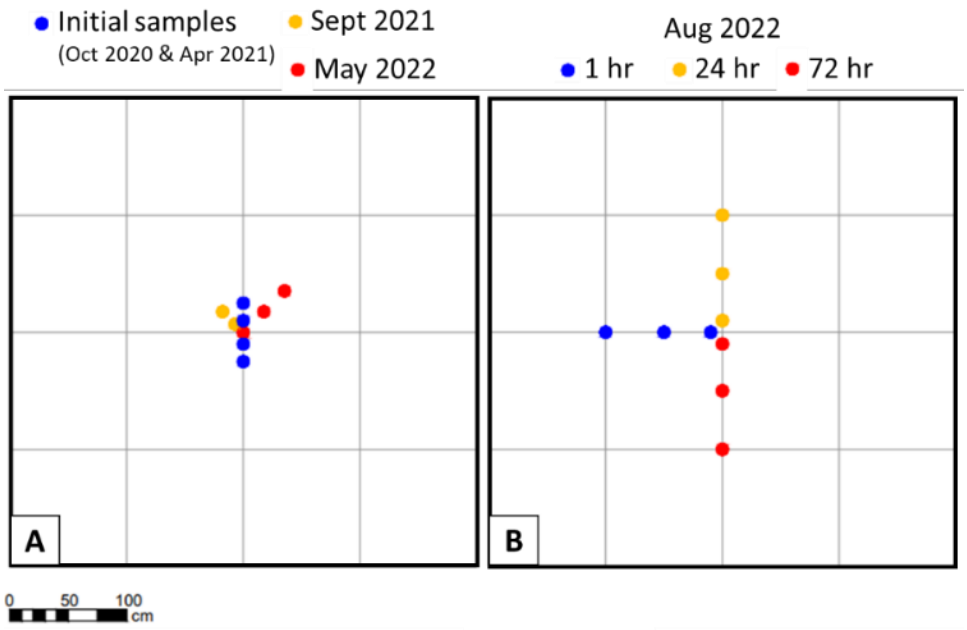

Figure A.18: A) Soil cores taken at various distances from the center of the seasonal experiments post infiltration and B) soil cores taken at 1 hr, 24 hr, and 72 hr post infiltration of the short-term experiment.

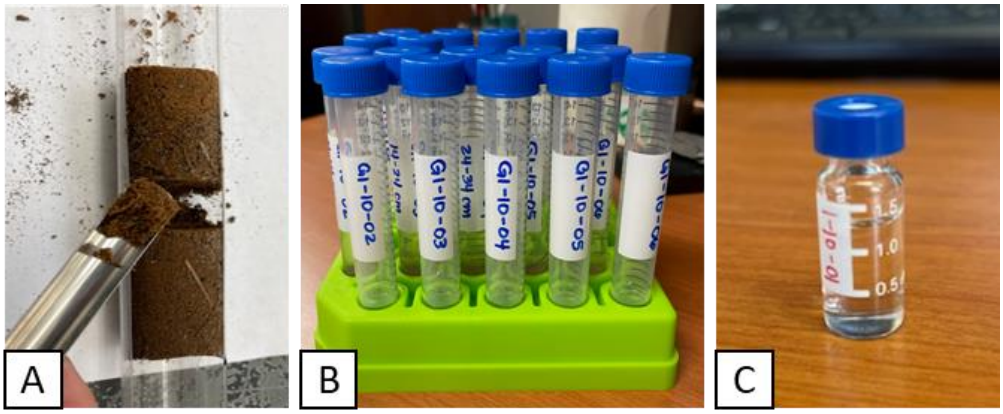

Figure A.19: A) Approximately 1 g of soil taken from the middle of soil interval, B) Soil mixed with 10 mL of DI water, shaken, and left to settle for 48 hours, C) Sample filtered through 0.45 µm filter to obtain a liquid representative of the soil sample before being processed through the HPIC instrumentation.

The chemical analyses of the samples were processed on the Dionex ICS-6000 HPIC System, and the data was interpreted using the Thermo Scientific Chromeleon Chromatography Data System

(CDS) software. The columns used in the HPIC instrumentation were the Dionex IonPac AS18 and the Dionex IonPac AG18. They were selected using the Thermo Scientific Dionex IonPac IC Column Selection Guide and are recommended for finding common inorganic anions in compliance with EPA Methods 300.0 (A) and 300.1 (TFS 2018). The nitrate and bromide calibration standards used for testing were prepared at 20, 10, 1, 0.5, 0.1, 0.05, and 0.01 ppm. From these calibration standards, the retention time for nitrate and bromide are identified to correspond to the same ions found in our samples, and the run time for the samples ranged from 15 to 30 minutes to adjust for ion detection accuracy. As the HPIC instrumentation processes the sample, each ion found in the sample starts showing up as peaks according to their electrical conductance and the time each ion is detected. Because of our known calibration standards, nitrate (NO3-) and bromide (Br-) are the only ions identified in our samples. The Br^- was differentiated from the sodium bromide (NaBr) salt by calculating the bromide concentration based on a 1:1 molar dissociation of sodium bromide in the solution (calculation in Appendix A). The concentrations from each 10-cm interval were then plotted with depth and compared with soil cores taken at various times throughout the experiment to determine the concentration changes over time. Additional nitrate and bromide concentration tests were taken at 30 cm, 80 cm, and 130 cm to determine an error analysis for the samples and instrumentation.

A.3. Results

The findings obtained from an investigation of the subsurface near a farm field using GPR, ERT, and physical and chemical soil analyses are interpreted in this section to help further understand the properties of the soil at the testing site and to explain the behavior and presence of the plume created by the sodium bromide solution over time.

A.3.1 Physical Analyses

A.3.1.1 Grain Size Correlations

The grain size distribution for a soil core sampled just outside the testing area shows slight variation with depth, as seen in Figure A.20. In addition, there are variations in the grain texture, with sharp changes at various depths such as 40 cm, 100 cm, and 140 cm, indicating the presence of multiple soil layers. The grain size distribution curves for this sample can be seen in Appendix B (Figure A. 38).

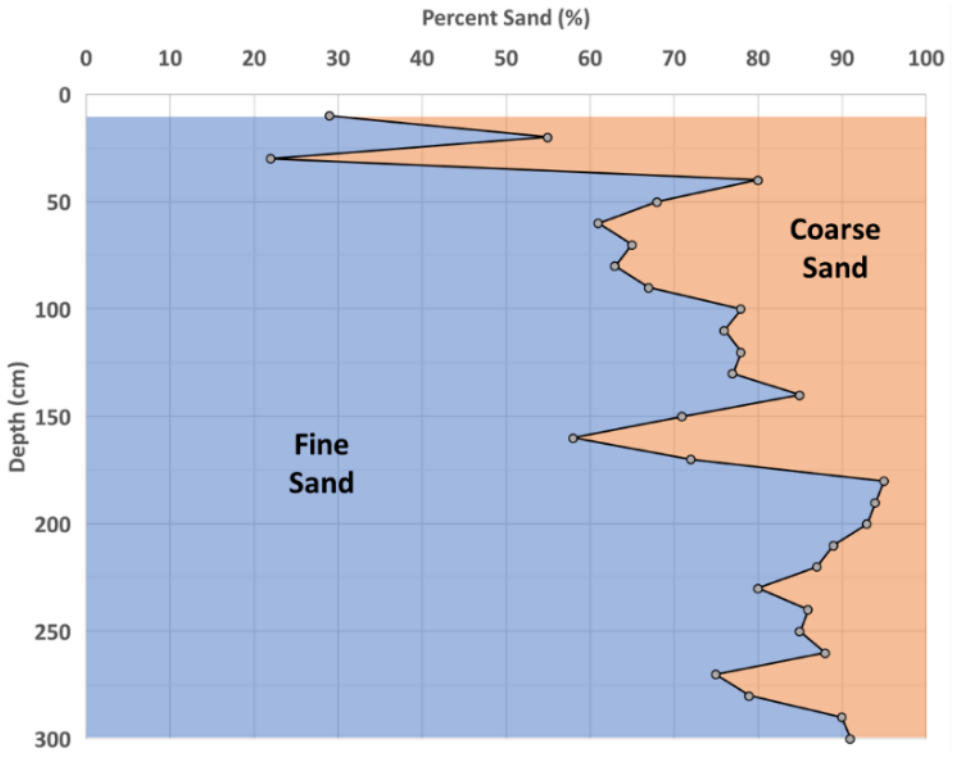

Figure A.20: Grain size classification for a soil core sample collected outside the infiltration testing area.

The variation in the grain size is documented using the D_{10}, D_{30}, and D_{60} in Figure A.21. The grain size decreases from 0.3 mm to 0.2 mm around a depth of 25 cm and remains almost constant after 50 cm until 1.75 m, where depth slightly increases. The saturated hydraulic conductivity, K_{sat}, using Hazen's equation (A.4), indicates that the hydraulic conductivity from 25 to 50 cm where there was a sharp decrease in D_{10}. The hydraulic conductivity is relatively low, from 50 cm to 1.75 m, before increasing slightly to an intermediate level past 1.75 m. Although the soil is classified as fine, clean sand, the grain size and hydraulic conductivity increases indicate textural variations with depth at similar points where concentration peaks were detected in the chemical analyses.

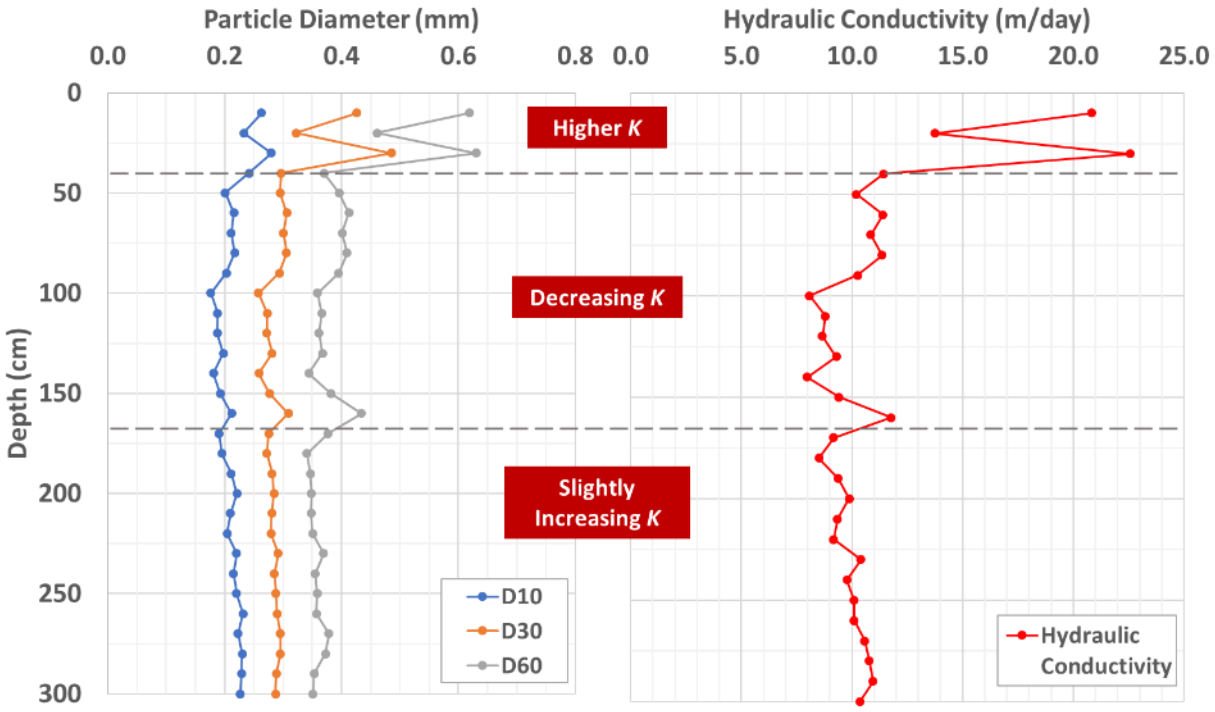

Figure A.21: Qualitative distribution of hydraulic conductivities based on particle sizes, particle size distribution, and the modified Hazen's equation for soil samples collected outside the testing area.

A.3.1.2 Hydrophobicity Classification of Soil

The water droplet on the left side of the sample in Figure A.22 shows the initial hydrophobicity of this sample located in the first 10 cm from the ground surface. This sample analyzed had a median WDPT of 60.2 seconds with a maximum and minimum WDPT of 120.5 seconds and 37.4 seconds, respectively. However, the WDPT times for each sample at depths below 10 cm were absorbed into the soil in less than one second with little to no remarkable change in absorption rate.

Figure A.22: Water droplet immediately after being placed onto the soil showing hydrophobic characteristics before being absorbed (left) next to a droplet already absorbed into the soil (right). This sample is from outside the infiltration testing area of the first 10 cm.

The hydrophobicity results of this sample and the sample inside the infiltration testing area from September 2021 (Figure A.23) are similar in the first 10 cm of the soil. However, the WDPT of the sample inside the infiltration testing area is significantly higher in the first 10 cm of soil than in the rest of the sample.

The hydrophobicity classification according to the WDPT times in Table A.3 classifies the soil sample inside the infiltration testing area as hydrophilic to slightly hydrophobic. In contrast, the sample outside the infiltration testing area is classified as hydrophilic to strongly hydrophobic. Since the sample outside the testing area is north-to-west, upgradient of the experiment site, this could suggest that the soil becomes less hydrophobic in the downgradient direction.

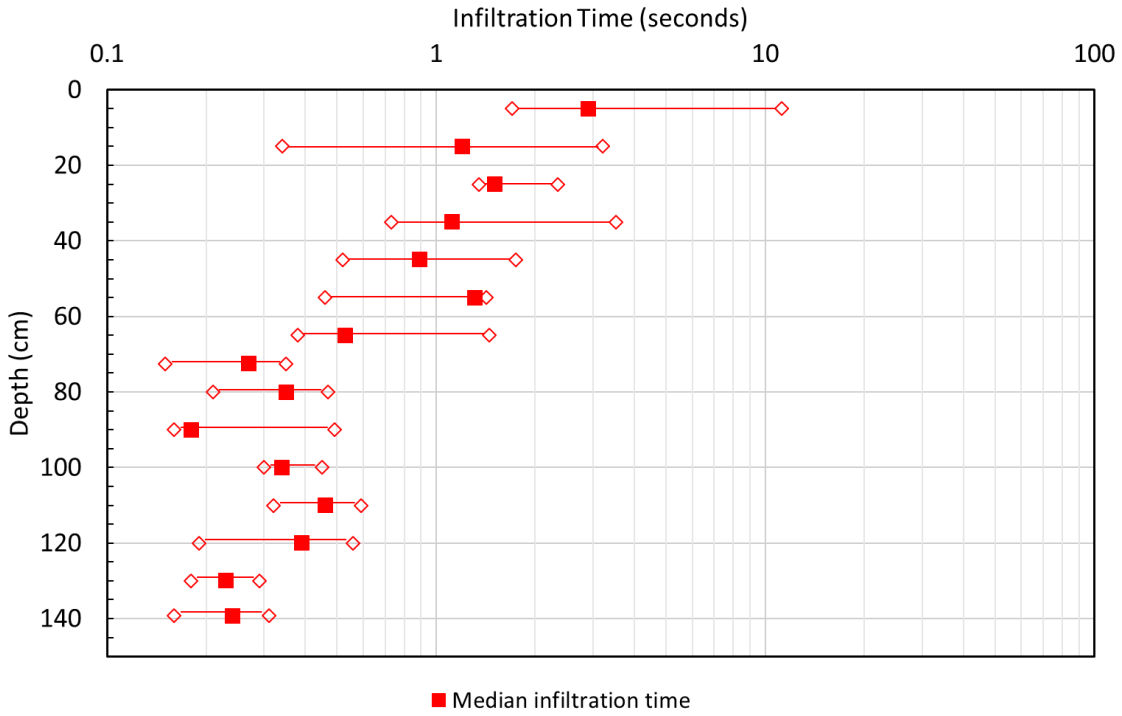

Figure A.23: Previous hydrophobicity results (Sept 2021) from a representative soil sample in the infiltration testing area near Field 19 (data collected by E. Carew).

A.3.1.3 Organic Matter Content

The results for organic content matter using the LOI method in the soil sample located 50 m northwest of the infiltration testing site start higher near the surface and significantly decrease with depth (Figure A.24). However, there are higher percentages of organic content at depths of 70 cm, 110 cm, and 160 cm.

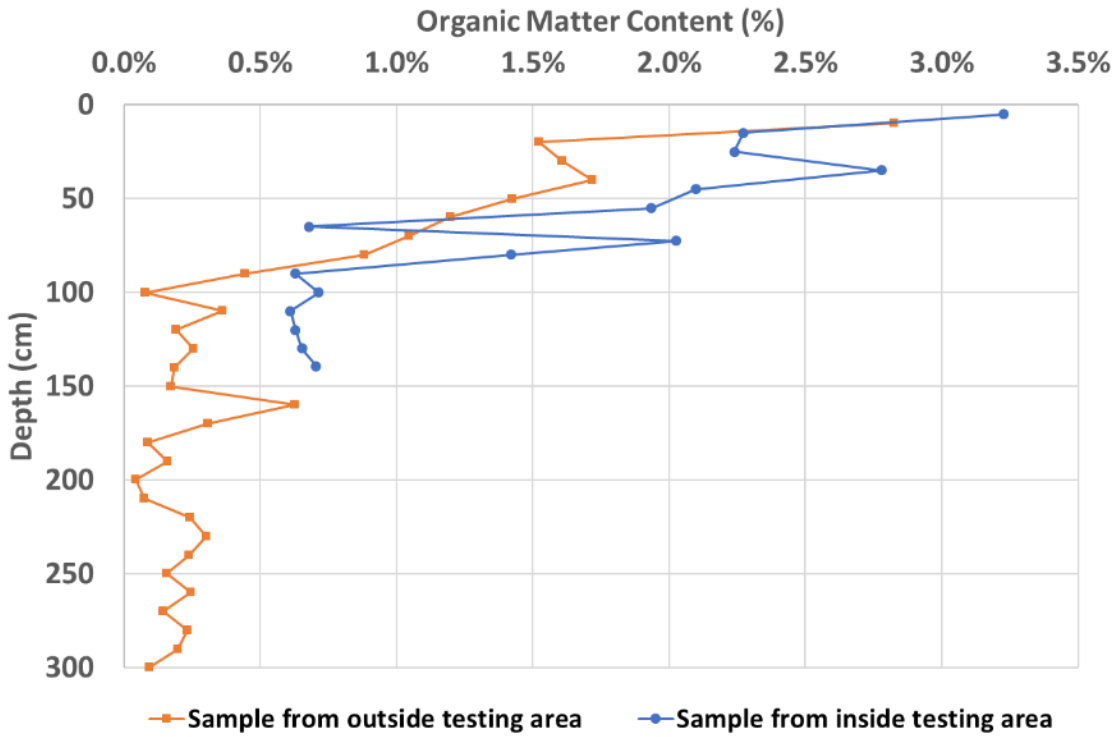

Figure A.24: LOI testing for two soil samples inside and outside the infiltration testing area.

A.3.2 ERT Imaging

A.3.2.1 Electrical Resistivity Profiles for the Seasonal Infiltration Experiment

Before injecting a 76 L sodium bromide solution, the pre-infiltration background conditions show relatively horizontal contours with constant electrical resistivity values after a depth of 0.3 m with slight variations in the resistivity near the surface (Figure A.25A). After 24 hours from the 76 L infiltration, the 0.025 M sodium bromide solution profile penetrates to a depth of approximately 1.0 m, with a small area of decreased resistivity (1000 Ωm to 1500 Ωm) west of the injection point (Figure A.25B). This observation likely results from the increased salinity and saturation in the soil created by the sodium bromide solution. The plume's width is estimated at 1.5 m, as the resistivity past this diameter is almost unchanged. After five months, the plume from the

infiltration of the solution is still apparent, with minimal curvature changes to the contour layers beneath it (Figure A.25C). The resistivity contour layers returned to a somewhat horizontal orientation, similar to pre-infiltration conditions. However, there is still a notable decrease in the resistivity range in these layers with depth after five months.

The electrical resistivity results in the south-to-north direction also show similar pre-infiltration conditions with identical dimensions of the depth and width of the plume (Figure A.26A). However, the direction of the plume is more recognizable because of the same small area of decreased resistivity south of the infiltration center after 24 hours (Figure A.26B). After five months, in the contour layers and under the infiltration area, the decreased resistivity has shifted in the south direction, indicating a plume direction towards the southwest (Figure A.25B and Figure A.26C). The overall decreased resistivity of the top layer (Figure A.25C and Figure A.26C) could be from a precipitation event, as the cumulative precipitation five days before the collection of the data was 19.5 mm.

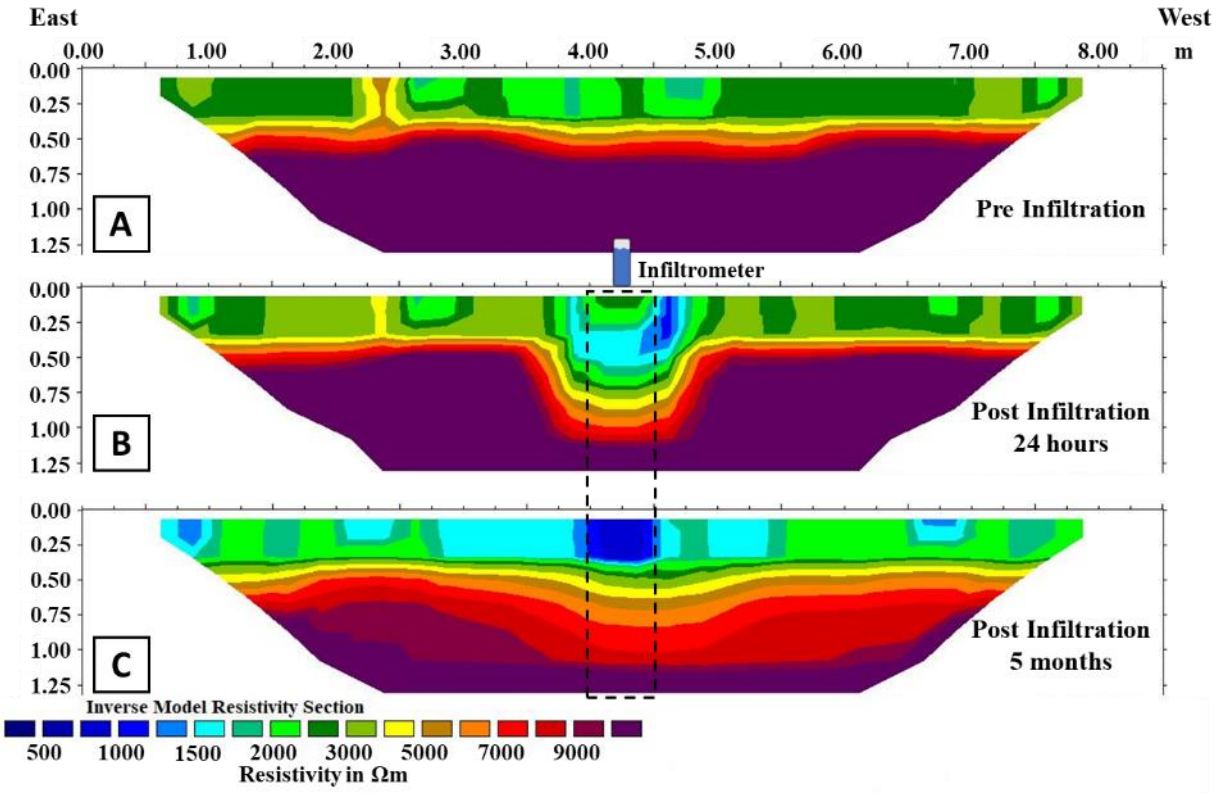

*Figure A.25: Seasonal monitoring of the electrical resistivity after five months in the **east-to-west** direction, where A) is the pre-infiltration condition before the April 2021 infiltration experiment (data collected by K. Swager), B) are the results after 24 hours from an injection of a 76 L NaBr solution (data collected by K. Swager), and C) are the results after five months from the initial injection.*

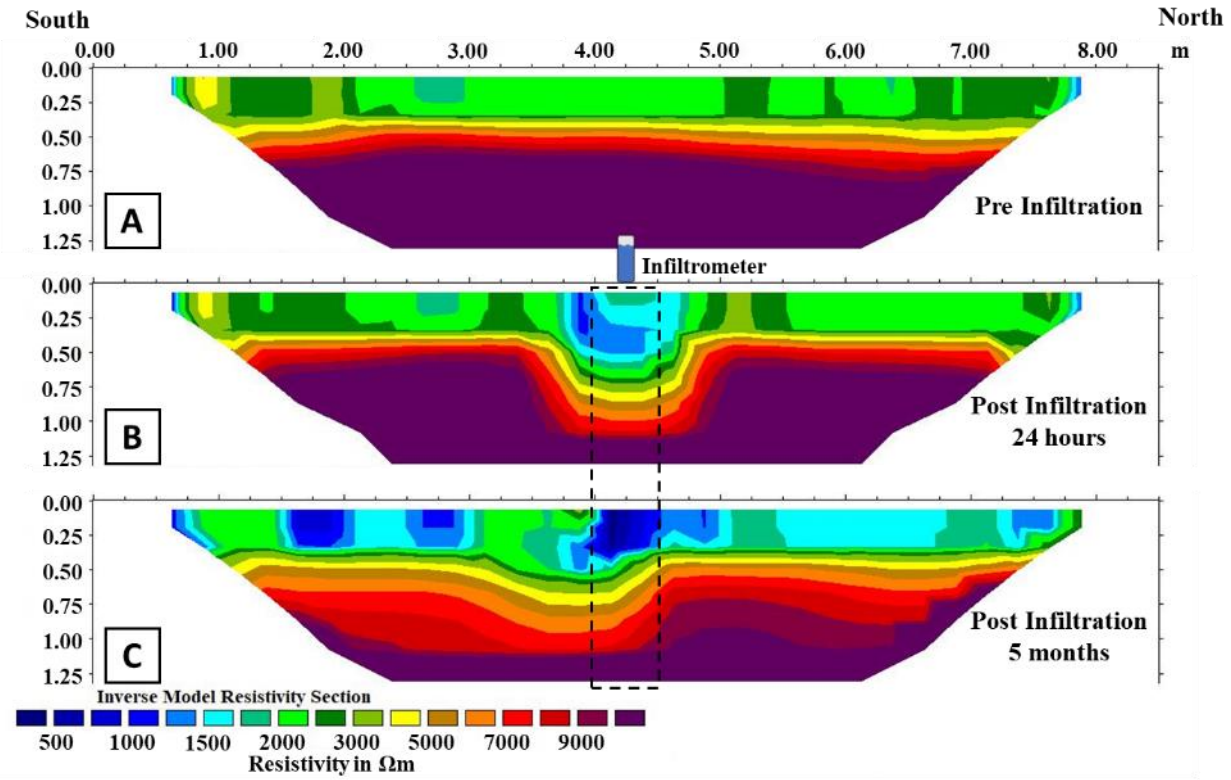

*Figure A.26: Seasonal monitoring of the electrical resistivity after five months in the **south-to-north** direction, where A) is the pre-infiltration condition before the April 2021 infiltration experiment (data collected by K. Swager), B) are the results after 24 hours from an injection of a 76 L NaBr solution (data collected by K. Swager), and C) are the results after five months from the initial injection.*

A.3.2.2 Electrical Resistivity Profiles for the Short-Term Infiltration Experiment

For the short-term infiltration experiment, ERT surveys were conducted pre-infiltration and 1 hour, 24 hours, and 72 hours after injecting a 40 L sodium bromide solution. The pre-infiltration conditions show small pockets of resistivity around 1000 Ωm near the surface and horizontal layers with a bend in the resistivity contour layers approximately 1.75 m west of the infiltration center after a depth of 0.3 m (Figure A.27A). The image presents decreased resistivity in the west direction and continues past a 1.0 m depth. One hour after an injection of the sodium bromide

solution, the plume from the solution is visible with a width of 1.5 m and depth of 0.6 m. The resistivity significantly decreases with depth west of the infiltration center, resulting in bends in the contour layers and creating a larger area of lower resistivity (Figure A.27B). The results after 24 hours are nearly identical to the profile one hour after the injection, with very slight resistivity decreases in small areas near the surface (Figure A.27C). After 72 hours, the results are still nearly identical to the previous two profiles. However, the resistivity decreases near the surface in the east direction until a depth of 0.3 m and in the west direction past a 1.0 m depth (Figure A.27D). While this spread is most likely the result of the sodium bromide injection, it is plausible that the results in Figure A.27D were influenced by a precipitation event of 35.3 mm that fell in the early morning hours before collecting the data for the 72-hour post-infiltration survey (precipitation data from NOAA).

The pre-infiltration resistivity results in the south-to-north direction show more variations in the depth and shape of the contour layers as well as pockets of low resistivity in the north direction (Figure A.28A). These contour layers are more horizontal, with a bend that starts 3.0 m north of the infiltration center. One hour after infiltration, the plume is heavily visible at a depth of 0.5 m and a width of 1.5 m (Figure A.28B). The resistivity has also decreased with depth by 2000 Ωm. Again, the results after 24 hours are nearly identical to those after one hour, with minor decreases in resistivity in small pockets near the surface (Figure A.28C). After 72 hours, the most notable changes in the profile are near the surface, where the resistivity has decreased in the south direction by 500 to 1000 Ωm and by 500 Ωm in the north direction. There is also a slight decrease in resistivity at a depth of 0.75 m (Figure A.28D). Again, the decreased resistivity near

the surface and the pockets to the north of the injection point may be influenced by the precipitation event shortly before the data collection.

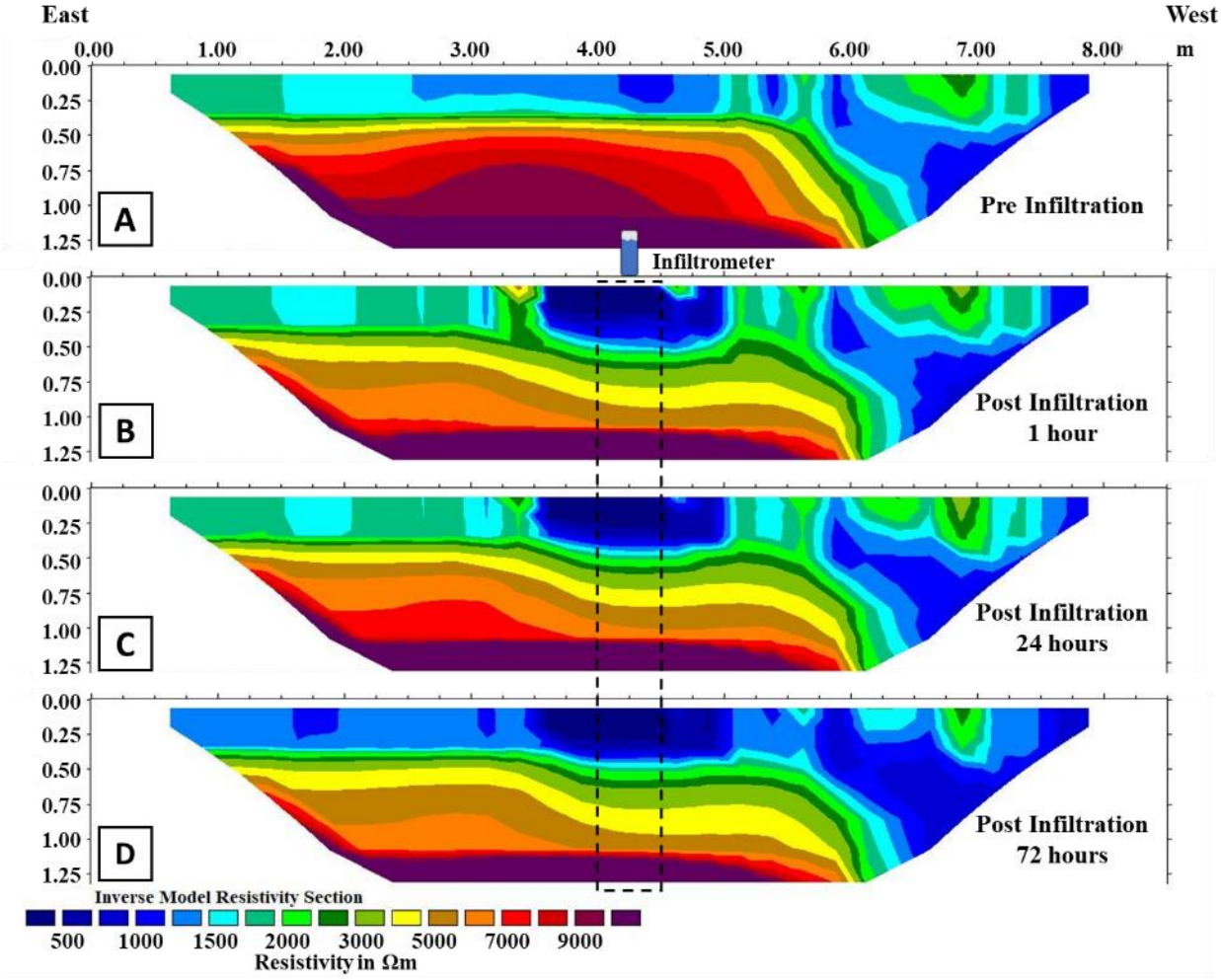

*Figure A.27: The 72-hour monitoring of the electrical resistivity in the **east-to-west** direction, where A) is the pre-infiltration condition before the short-term infiltration experiment, B) are the results after 1 hour from an injection of a 40 L NaBr solution, C) are the results after 24 hours, and D) are the results after 72 hours from the initial injection.*

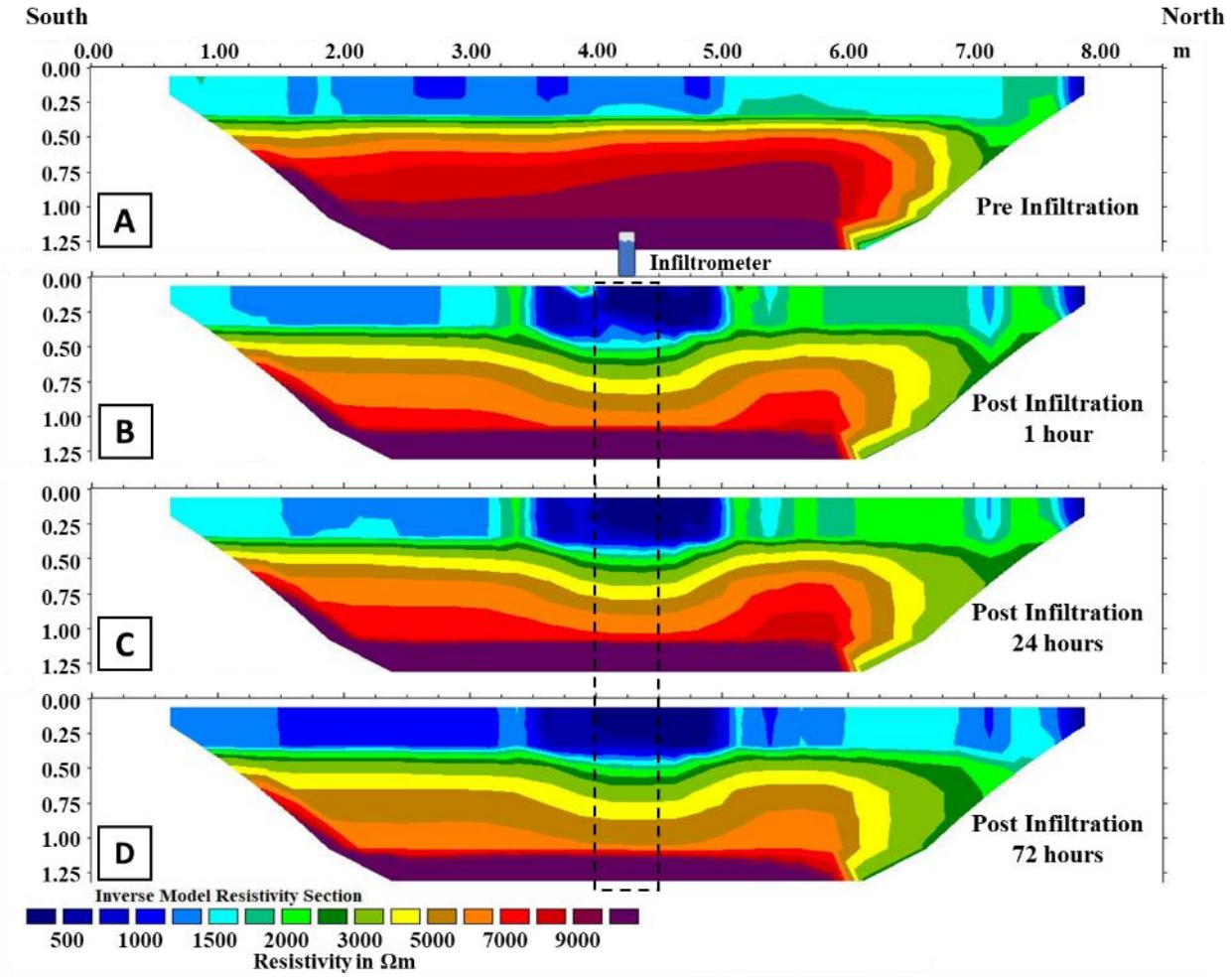

*Figure A.28: The 72-hour monitoring of the electrical resistivity in the **south-to-north** direction, where A) is the pre-infiltration condition before the short-term infiltration experiment, B) are the results after 1 hour from an injection of a 40 L NaBr solution, C) are the results after 24 hours, and D) are the results after 72 hours from the initial injection.*

A.3.3 GPR Imaging

The GPR imaging from the short-term infiltration experiment shows a pre-infiltration condition in the north-to-south and west-to-east directions, coinciding with approximately where the water table is about 2.3 m deep near Field 19. However, one hour after the sodium bromide solution injection, the signals at this depth and 4 to 6 m deep significantly reduce or completely

disappear near the center of the injection area (Figure A.29). This attenuation is likely due to increased soil conductivity caused by increased pore fluid salinity and saturation in the subsurface from the solution. The plume width from the GPR results also matches the plume width from the ERT results, with an approximate size of 1.5 m.

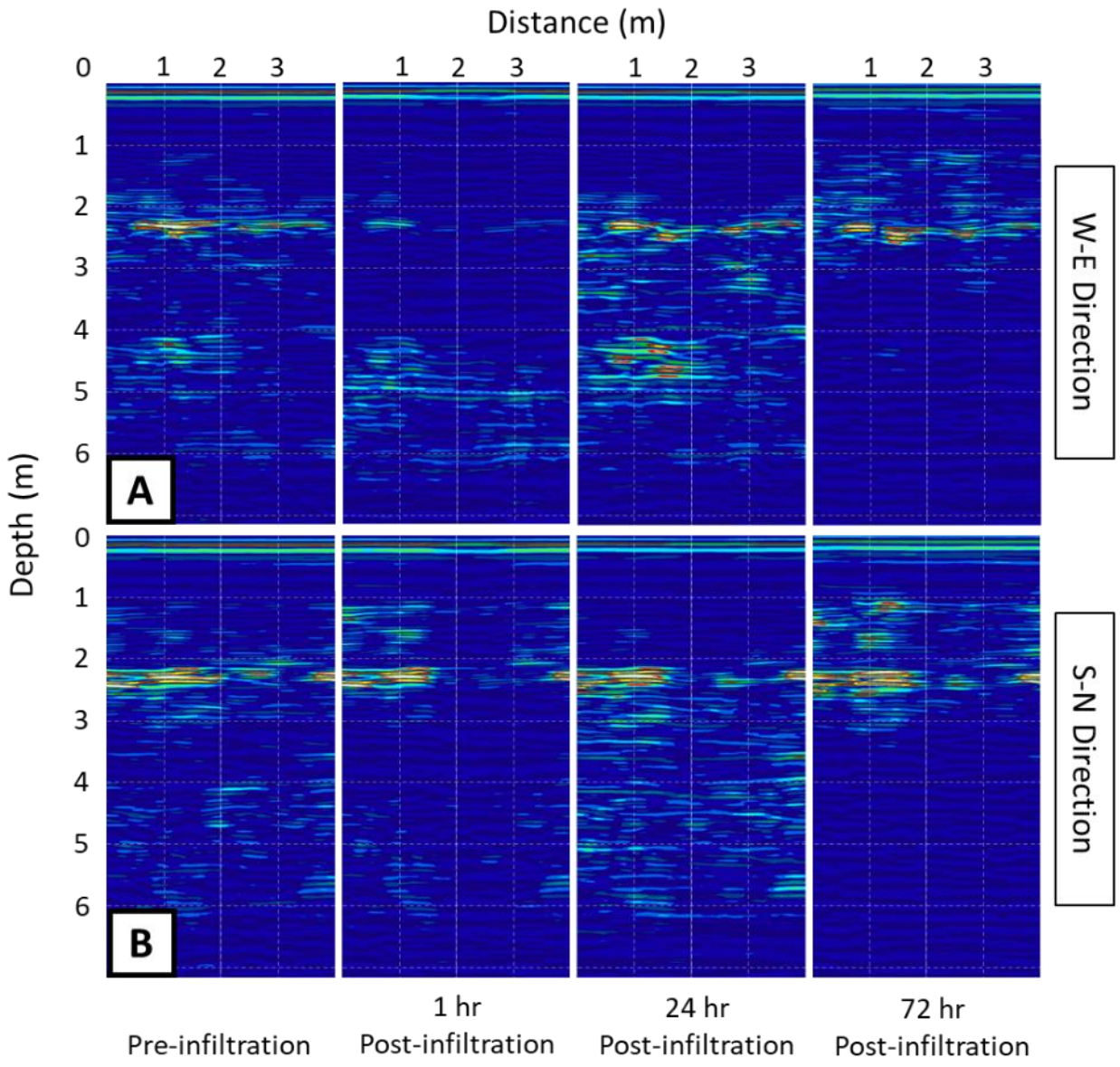

Figure A.29: GPR imaging results in the A) west-to-east direction and the B) south-to-north direction through the center of the 72-hour, short-term infiltration experiment.

The signals in the west-to-east direction are almost nonexistent along the 4 m line, with the signals strongly retained on the left side of the injection point in the south-to-north direction. This pattern suggests an almost immediate solution flow path in the southwest direction, similar to the plume direction from the ERT results. The signals return one day after the infiltration, with conditions returning to almost pre-infiltration conditions after three days. However, the signals remain mostly absent past 3 m deep after three days. This observation suggests that the infiltrated solution is still present past the water table.

GPR results were also obtained during the April 2021 infiltration experiment by Swager 2021. Data was collected before the infiltration and one hour and 24 hours after infiltration in both the north-to-south and west-to-east directions. The changes seen from these results were also very similar to what is seen in Figure A.29, where the conditions of the subsurface return to almost pre-existing conditions before infiltration.

A.3.4 Nitrate and Sodium Bromide Concentrations with Depth

Soil cores were extracted around the infiltration areas in September 2021 and again in May 2022 to monitor the seasonal changes in the soil water chemistry after initial infiltration experiments. In addition, soil cores were also extracted in August 2022 one hour, 24 hours, and 72 hours after an infiltration experiment to monitor the soil water chemistry of the subsurface up to 72 hours from infiltration. The soil cores were continuously tested every 10 cm for the full depth of the core. Data points shown in the following graphs are concentrations of nitrate or bromide ions that were detectable and measurable by the HPIC instrumentation in the samples for each depth.

The following results do not include and are not compared with the concentrations of nitrate and bromide data from the soil cores previously collected during the initial infiltration experiments. This is because the range of noise from that data appears to indicate that the results were erroneous. Therefore, the concentration data from the initial time of injections will not be presented. However, the data collected and analyzed monitoring the chemical changes in the soil since the initial infiltration will be presented in this section and discussed later in this study.

A.3.4.1 Bromide Concentrations from the Seasonal Infiltration Experiments

Bromide results of the seasonal monitoring from the injection of the sodium bromide solution include data ranging from five to nineteen months after the initial infiltration experiments. There are large concentration spikes at depths of approximately 80 cm and 120 cm in the northern section of the seasonal experiment area (Figure A.30A). In comparison, the southern portion of the seasonal experiment area shows more minor variations in concentration spikes at depths of approximately 30 cm, 100 cm, and 160 cm (Figure A.30B).

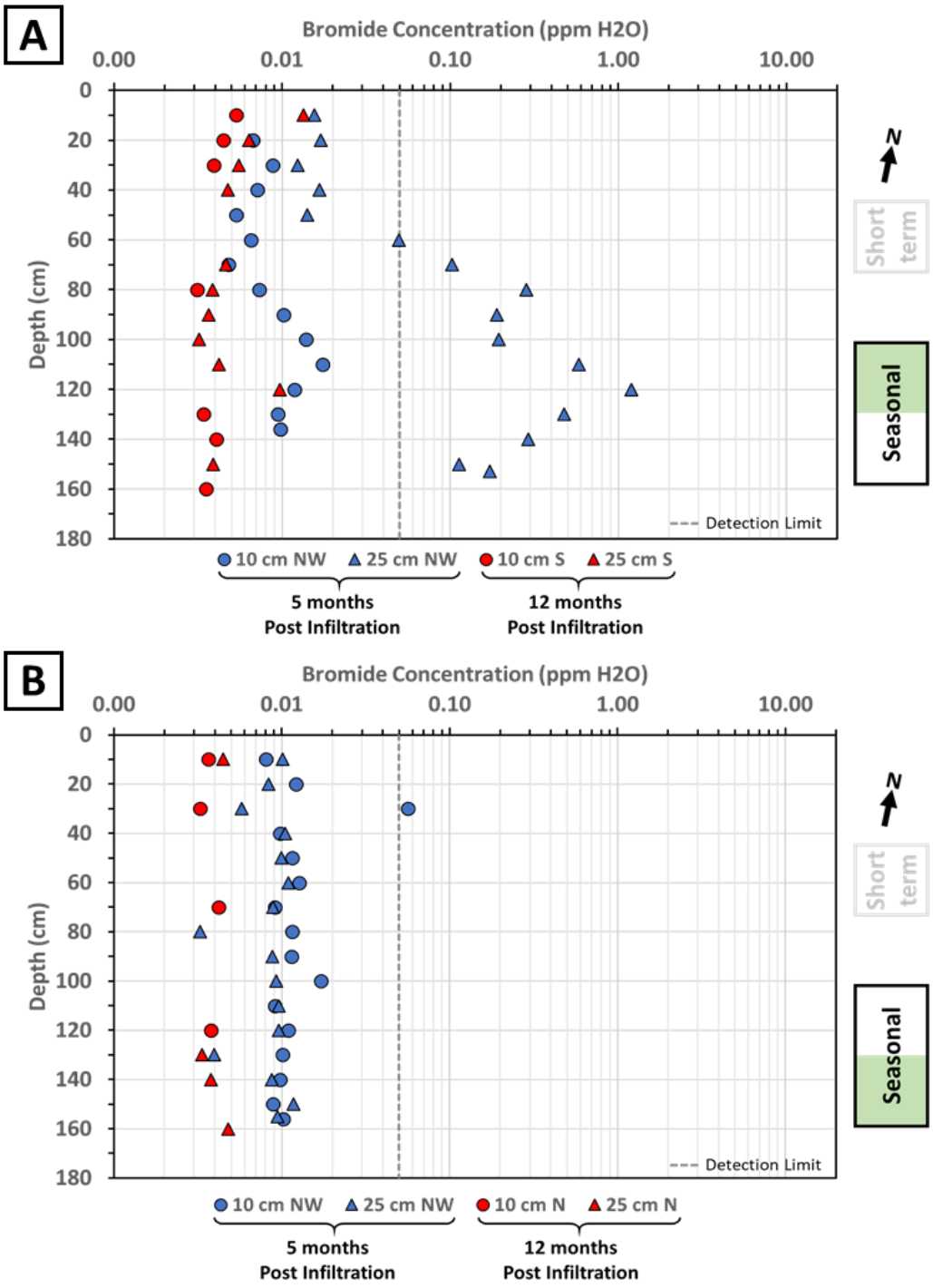

Figure A.30: Bromide concentration results A) 5 months and 12 months post infiltration from an infiltration experiment in April 2021 and B) 11 months and 19 months post infiltration after an infiltration experiment in October 2020. Distances correspond to the length from the center of the infiltration area.

The concentrations in these areas are also slightly higher the farther away from the center of the infiltration area where the solution was injected. However, the results show that the soil's bromide concentration decreases significantly over the experiments, with an almost constant trend 11 months post-infiltration and very minimal to undetectable concentrations 19 months post-infiltration.

Although the results from another seasonal infiltration experiment conducted on the testing site in September 2020 will not be presented in this study, chemical analyses were still conducted on the soil cores collected at similar times using the same testing procedures. Therefore, it is important to note that the bromide concentration results from this area also reflect a decreasing concentration with depth with data spikes at approximately 60 cm, 110 cm, and 150 cm.

A.3.4.2 Nitrate Concentrations from the Seasonal Infiltration Experiments

The nitrate concentration in the subsurface was also monitored to observe the changes in concentration versus depth throughout a farming season on the field. Fertilizer for each growing season is typically applied from May through July (Table A.5 in Appendix B). The samples collected in September 2021 reflect the subsurface conditions of nitrate contamination two months after the last application of fertilizer to Field 19 for the 2021 farming season, while the samples collected in May 2022 reflect the conditions one week before the first application of fertilizer for the 2022 farming season. The samples collected in September 2021 had the highest nitrate concentration values, over 10 ppm. These values were only seen in the first 10 cm below the surface and ranged from 12.4 to 15.7 ppm (Figure A.31).

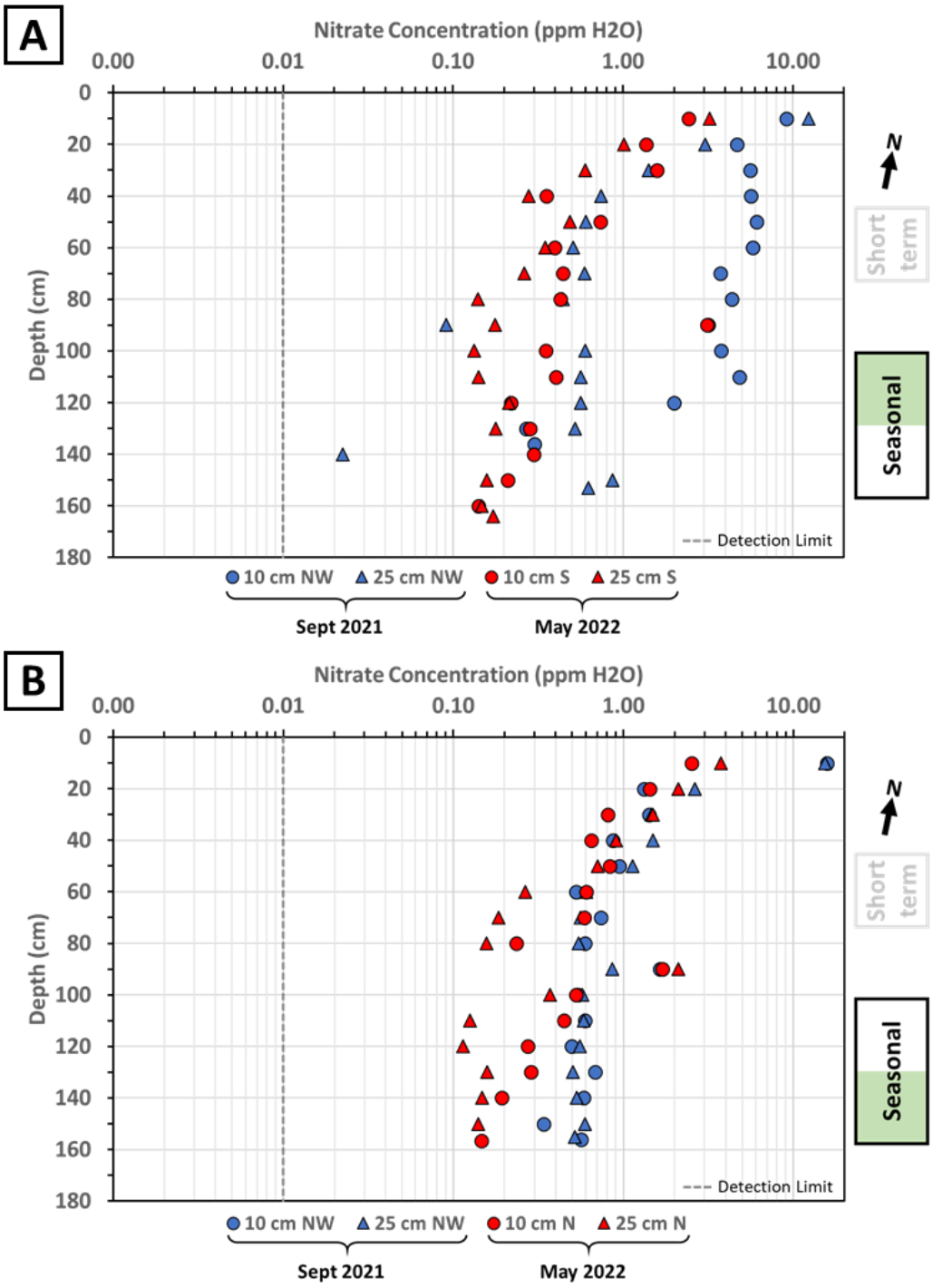

Figure A.31: Nitrate total concentration results from soil samples collected in A) September 2021, two months after the last application of fertilizer to Field 19, and in B) May 2022, one week before the first fertilizer application for the farming season.

The nitrate concentrations from the samples collected in May 2022 are relatively the same as their curves, both showing a decrease in concentration with depth and distance from the center of the infiltration area. However, concentration spikes in both data sets from each sample collection. These spikes happen at a depth of approximately 90 to 110 cm and again at 140 to 150 cm.

Again, since we used the same chemical analysis testing procedures for a seasonal infiltration experiment done in September 2020, it is essential to note the nitrate concentration results. The concentrations also decreased with depth and had a maximum value of nitrate 10 cm below the surface, with the highest concentration being 8.1 ppm in September 2021 and 4.2 ppm in May 2022. Concentration spikes were also observed at approximately 50 to 60 cm, 90 to 100 cm, and around 160 cm.

A.3.4.3 Bromide Concentrations from the Short-Term Infiltration Experiment

Another infiltration experiment was conducted in August 2022 to monitor the short-term changes in the subsurface up to 72 hours after infiltration. Soil samples were analyzed from core extractions taken at one hour, 24 hours, and 72 hours after the initial infiltration. Figure A.32 shows the results from each of these analyses. The data appears scattered, however, showing a general decrease in concentration in short-depth ranges. The highest bromide concentrations recorded one hour after infiltration were 25.7 ppm and 29.7 ppm at 10 cm and 50 cm west from the infiltration center, respectively, at a depth of 10 cm. After 24 hours, the concentrations began to decrease near the surface to 18.4 ppm and 11.8 ppm, with a significant decrease in

concentration after 72 hours—the graph's scattered appearance results from concentration spikes at various depths. The 24-hour and 72-hour analysis data is absent 100 cm north and south of the infiltration center. This is likely a result of a low concentration undetectable by the instrumentation. There is also very sparse data after a depth of 110 cm, and the result of the noise in the data could be the result of the 0.05 ppm detection limit. All the concentrations recorded below this depth are from 100 cm west of the infiltration center. This absence of data may suggest that the tracer traveled westward and disappeared at this distance after 24 hours.

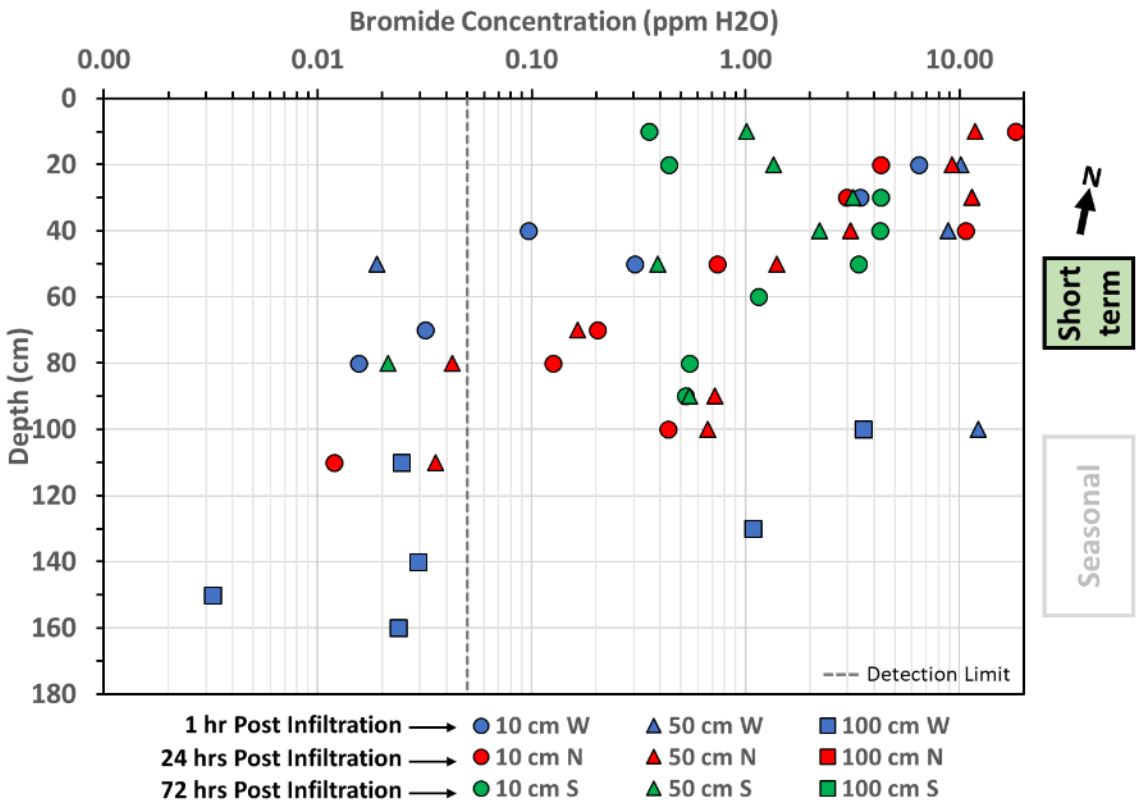

Figure A.32: Bromide concentration results from the 72-hour monitoring of an infiltration experiment.

There are many concentration spikes in these results, notable at approximately 100 cm for the one-hour analysis, 30 to 40 cm and 90 to 100 cm in the 24-hour analysis, and 30 cm and 90 cm in the 72-hour analysis.

Soil samples were also analyzed in the observed fingerings and dark/saturated pockets of soil collected during excavation after 72 hours. The excavation started approximately 40 cm west of the infiltration center and continued 15 cm west of the infiltration center. The locations of the samples collected are shown in Figure A.33, along with the bromide concentration results.

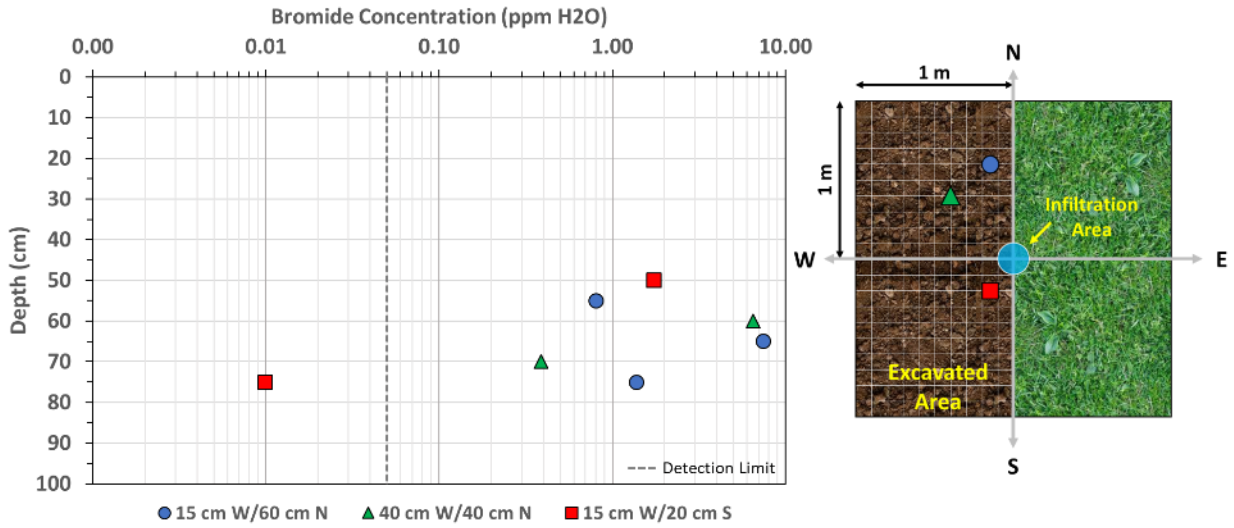

Figure A.33: Bromide concentration results of the fingerings and dark-colored/saturated pockets of soil samples collected during the soil excavation of the short-term infiltration experiment.

After 72 hours, the concentrations detected in the fingerings or soil pockets decreased with depth. However, there is an observed spike of 7.5 ppm at a depth of 50 cm in the sample northwest of the infiltration center.

A.3.4.4 Nitrate Concentrations from the Short-Term Infiltration Experiment

The nitrate concentrations were also analyzed at different times after initial infiltration. Although no nitrate was injected during these infiltration experiments, and the samples were collected one month after the last application of fertilizer to the field, the results still varied slightly. Generally, the trends for each analysis post-infiltration are consistent with a gradual decrease in concentration with depth (Figure A.34). For example, the highest concentration of 3.1 ppm is seen 50 cm south at a depth of 10 cm. This value was recorded 72 hours after initial infiltration and is consistent with the highest concentration values seen in the seasonal infiltration experiments at this depth (3.2 ppm and 3.7 ppm).

A significant concentration spike is observed at a depth of 100 cm, and other minor spikes at 70 to 90 cm and again at 150 to 170 cm. These results are also consistent with the concentrations from the seasonal experiment, where spikes were observed at approximately the same depths. However, over half of the recorded values for each analysis from the short-term experiment fall below 0.1 ppm. This is unusual because almost all recorded nitrate concentrations from the seasonal experiment exceed this threshold. Since the results from this short-term experiment are from samples collected one month after the last application of fertilizer to Field 19, it could be hypothesized that the nitrate concentrations would be higher than that of samples collected before the start of a farming season before any fertilizer has been spread.

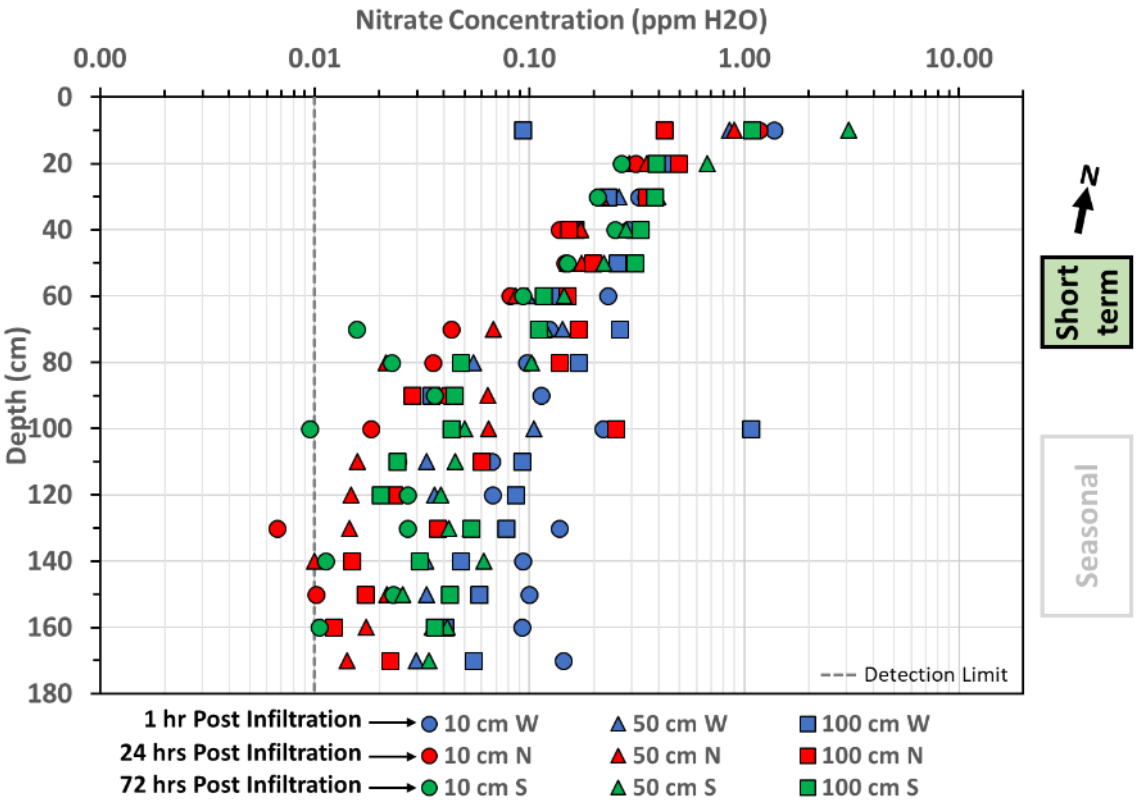

Figure A.34: Nitrate concentration results from soil samples analyzed in August 2022, one month after the last fertilizer application for the 2022 farming season.

Although the nitrate was tested in the same time intervals as the bromide analyses, Figure A.34 does not accurately represent the long-term effects of nitrate contamination with depth. The data from Figure A.34 was replotted using the minimum, median, and maximum values from all the data points at each depth. Because nitrates in the vadose zone result from a long-term effect, Figure A.35 shows a more logical approach to visualizing nitrate contamination with depth.

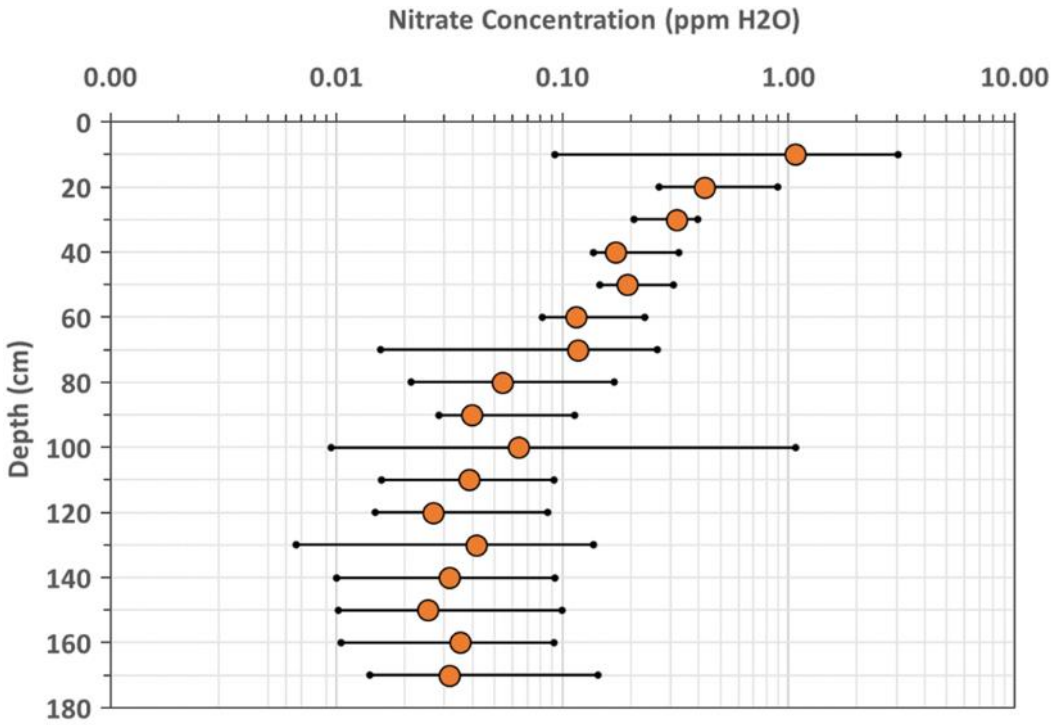

Figure A.35: Nitrate concentration data using the minimum, median, and maximum values in Figure A.34 to show the long-term changes of nitrate with depth.

The nitrate concentrations analyzed from the fingerings and soil pockets seen during the excavation show minimal increased concentrations in depths of approximately 65 to 75 cm (Figure A.36) but generally decrease with depth.

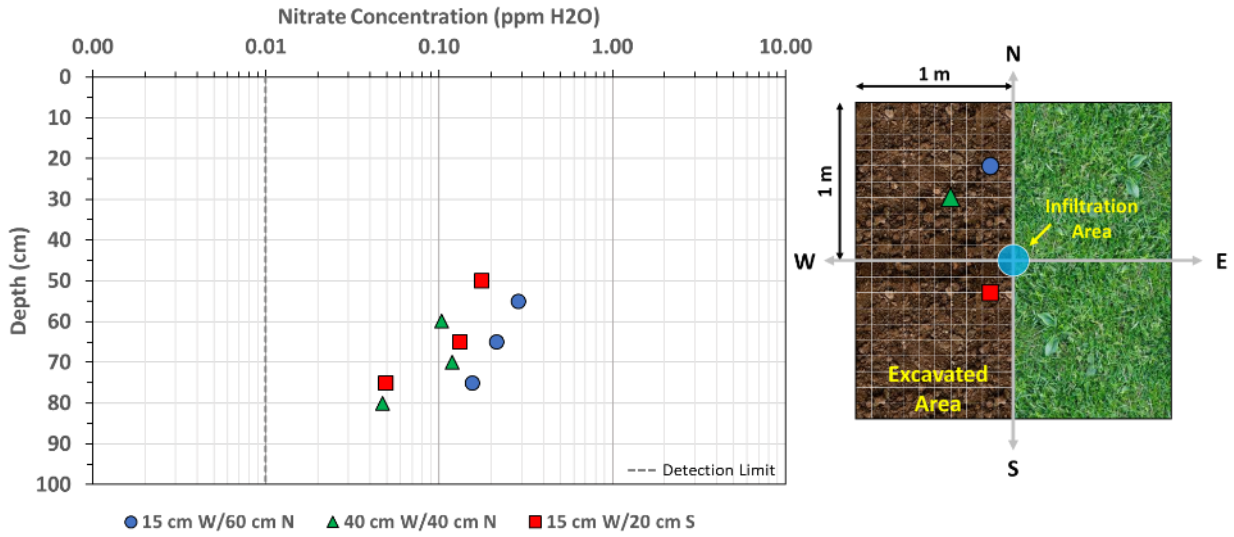

Figure A.36: Nitrate concentration results of the fingerings and dark-colored/saturated pockets of soil samples collected during the soil excavation in August 2022.

A.3.5 Ground-Truthing

After the 72-hour monitoring period of the short-term infiltration experiment, an excavator was used to dig a soil pit across the infiltration area to observe if the dyed tracer solution was visible at any depth in the subsurface. The excavation showed fingering, assumed from the infiltration from the appearance of the darker color from the dye, in depths as far down as 80 cm (Figure A.37). The fingering was assumed to be caused by roots and other heterogeneities, as there were subtle changes in the soil composition.

Figure A.37: Fingering shown at multiple depths (>55 cm) after excavating the short-term infiltration area.

A.4. Discussion

This research aimed to investigate contaminants' transport processes in the vadose zone by using geophysical methods and chemical analyses to evaluate the changes in the subsurface from different infiltration mechanisms. The site chosen for fieldwork was initially anticipated to exhibit a uniform infiltration pattern through clean sand, causing a vertical plume with limited lateral spreading. However, subsequent geophysical surveys and laboratory findings indicated that the soil stratigraphy and initial conditions were more intricate than expected. The sodium bromide solution used in the study seemed to accumulate at interfaces of finer-grained soils in the top 1.4 meters of the soil before moving into coarser-grained sediments and eventually reaching the water table. This suggests the presence of multiple soil layers with varying textures that promote the solution's retention and lateral flow.

The resistivity data indicated a two-layer system, with the upper 0.5 m of soil having lower resistance and higher resistive sediments underneath. The resistivity pre-infiltration also showed a clear horizontal interface at approximately 0.5 m. The resistivity increased from 3,000 Ωm to over 9,000 Ωm, indicating a change in the soil texture as the particles become coarser with depth. However, the GPR data showed clear reflectors at approximately 2.0 m, which could indicate the water table. The lack of attenuation from the surface to this depth was not apparent enough in the GPR signals to indicate the varying layers detected using ERT. The ERT results from the seasonal infiltration experiment 24 hours after injection show areas of decreased resistivity at a maximum depth of 1.0 m west and south of the injection point. After five months, the plume is still visible with minimal curvature changes to the electrical resistivity contour lines beneath. The

contour lines appear to be returning to a somewhat horizontal orientation, similar to the contour lines of pre-infiltration conditions, with a slight bend of decreased resistivity in the south direction. In the short-term infiltration experiment, the results also show the resistivity significantly decreasing with depth west and south of the infiltration center after injection. However, while most of the reduced resistivity is observed in the south and west directions, there are also slight decreases in the north and east directions after 72 hours. These results suggest that the plume spreads laterally after three days, reaching a maximum depth of 0.5 m.

The data for both experiments consistently shows that the low resistivity plume created after the sodium bromide solution injection stays in the soil's upper layers (0.5 to 1.0 m), laterally spreading in each direction to a maximum plume width of 1.5 m. This depth extent from the plume correlates with the sharp increases in the bromide concentration data from the soil chemistry analysis. The average data spikes are observed at 30 to 40 cm depth and again at 110 to 120 cm. Furthermore, the plume from the seasonal experiments penetrated almost 0.5 m deeper than the short-term one. This behavior is supported by the hydraulic conductivity values for each infiltration area, with the short-term experiment having the highest hydraulic conductivity of 14.4 m/day and the seasonal experiment having values as low as 7.1 m/day. Therefore, it is expected that the plume created from the short-term experiment should take longer to reach the groundwater table. Since these results model the increased salinity in the soil created from the sodium bromide solution, we can infer a flow path in the southwest direction.

The results of the GPR imaging from the short-term infiltration experiment reveal exciting findings. Before infiltration, the GPR signals show a consistent pattern that aligns with the approximate depth of the water table. However, significant changes are observed in the GPR signals after injecting the sodium bromide solution. One hour after the infiltration, the signals of the water table and at 4 to 6 meters deep show a significant reduction or complete disappearance near the center of the injection point. Further analysis of the GPR signals reveals that the changes are more prominent in the west-to-east direction. The signals are almost nonexistent along the entire 4-meter line and are strongly retained only on the left side of the injection point in the north-to-south direction. This pattern suggests the infiltrated solution's almost direct flow path in the southwest direction.

The temporal changes in the GPR signal over time also provide interesting insights. For example, one day after the infiltration, the signals start to return, and after three days, the conditions in the subsurface almost return to pre-infiltration conditions. However, the signals remain mostly absent beyond 3 meters deep even after three days, indicating that the infiltrated solution may still be present in the subsurface below the water table. These results suggest that the impacts of the infiltrated solution may persist in the subsurface even after a few days.

The seasonal monitoring of bromide concentrations showed large concentration spikes at depths of approximately 80 cm and 120 cm and more minor variations in concentration spikes at depths of roughly 30 cm, 100 cm, and 160 cm. The concentrations in these areas were slightly higher the farther away from the center of the infiltration area where the solution was injected, indicating

a spatial variability in the bromide movement in the subsurface. In addition, the trend of decreasing bromide concentrations with time was observed in the seasonal infiltration experiment areas, with almost constant concentrations 11 months post-infiltration and very minimal to undetectable concentrations 19 months post-infiltration. The results suggest that bromide moves through the subsurface and attenuates over time.

Similarly, the nitrate concentration results from the seasonal monitoring showed a decrease in concentration with depth. The samples collected in September 2021 show the highest concentration near the surface, with concentration spikes at 30 cm and 90 cm. This is expected as the analysis was done two months after the last application of fertilizer to the field. The samples collected in May 2022 were lower in nitrate concentration near the surface but followed the same trend with depth as the samples from September 2021. The decrease in concentration during this time is most likely a result of no fertilizer being applied to the field for over a year. The nitrate concentration results from the short-term experiment highlighted the concentration of nitrate vs. distance and identified the retention depths of higher concentrations. The concentration generally decreased significantly with depth. However, the highest concentrations observed were in the west direction and the lowest in the north direction. Since the flow can be assumed in the southwest direction, the nitrate travels in the same direction.

The results from these soil water chemistry measurements highlight the dynamic nature of subsurface water chemistry and the complex interactions between soil, water, and chemical constituents. The observed spatial and temporal variability in nitrate and bromide concentrations

suggests that these chemicals can move through the subsurface and undergo transformations or attenuations over time, leading to changes in their concentrations. The sparsity of the bromide concentration data points from the short-term infiltration experiment also highlights the possible heterogeneities in the soil, especially in a depth past 1 m. In addition, the concentration spikes observed at various depths indicate that there may be preferential flow paths or localized areas of higher concentrations in the subsurface, which could have implications for nutrient management and water quality protection in agricultural fields.

The organic content is higher near the surface of the soil sample and significantly decreases with depth. However, there are spikes in organic content at approximately 70 cm, 110 cm, and 160 cm depths, corresponding to the same depths where concentration spikes were observed in the chemical analyses of nitrate and bromide. These observations suggest a potential correlation between organic content and chemical concentrations in the soil. The hydrophobicity analysis classifies the soil sample outside the infiltration testing site as hydrophilic to strongly hydrophobic, with shorter WDPT times indicating higher hydrophobicity. In contrast, the sample inside the infiltration testing area is classified as hydrophilic to slightly hydrophobic, with significantly higher WDPT times in the first 10 cm of soil. This could suggest that the hydrophobicity of the soil decreases in the downgradient direction. However, only the first 10 cm of the soil provided usable data, so this method may not be a reliable analysis for comparison. The grain size distribution data showed textural layers in the soil, with coarser layers at 30 cm and 160 cm and finer-grained layers at 40 cm, 100 cm, and 140 cm. The observations of fingering and dark pockets of soil in the subsurface after the infiltration of the dyed sodium bromide

solution are most likely attributed to roots and other heterogeneities in the soil, indicating potential spatial variability in soil composition. Overall, the results suggest that there are minor textural variations in the soil with depth, which are correlated with changes in hydraulic conductivity, grain size distribution, organic content, and chemical analysis of the soil. The results from these tests support the theory of spatial variability within the soil, indicating a more complex transport process in the vadose zone.

The difference in the chemical results may be related to the localized injection of the bromide solution vs. the uniform spreading of nitrate fertilizer in the field. The area used for injection into the middle of the experimental infiltration areas represents a smaller portion that may not precisely reflect the spreading and runoff an entire farm field may experience in a recharge event. The duration of the compounds' application could also have played a role in the difference in results because the application of the solution was made rapidly. In contrast, the application in the real world may be gradual. Finally, even though the site is characterized as homogeneous, there were still minor soil heterogeneities that could explain why spikes of higher concentration were seen at the boundaries. These reasons emphasize the complex nature of the processes but help to understand what changes can be made to future experiments to yield more finite results.

A.5. Conclusion and Recommendations

This research continued a study investigating a constant-head ring infiltration plume using near-surface geophysical methods. The infiltration process encountered textural boundaries in the soil, resulting in an attenuated plume rather than a homogeneous infiltration column. Results from GPR and ERT surveys indicated stratigraphy in the soil structure, which was still observable in the subsurface over time. The initial hypothesis of a two-layer system with a capillary barrier, proposed by Swager (2021), was based on electrical resistivity surveys. However, since the hypothesis contradicted tracer concentrations, water content, and grain size distribution data after laboratory monitoring and field tests, a new hypothesis was created, suggesting a multi-layer soil structure with multiple textural boundaries that could potentially slow down plume progression.

The site was assumed to be a homogenous sandy soil deposit. However, we have seen very subtle changes in the soil, such as from fine sand to coarse sand, which may be the boundaries that prevent the plume from the infiltration experiment from spreading. The fingering suggests that these small pockets of discoloration at or slightly above/below the subtle boundary changes that we can see contribute to the retention of the solution injected at the site. In addition, the concentration spikes of nitrate and bromide at similar depths may also indicate subtle boundary changes in the subsurface, which could contribute to the decrease and diffusion of the plume after both infiltration experiments. However, the varying depths we see in these concentration spikes have too broad of a range (i.e., an 80 to 120 cm depth) to make a direct assumption of fine-scale heterogeneities contributing to clear textural boundaries.

This research has several unresolved aspects, including a comprehensive comprehension of the spatial and temporal heterogeneity, the timeframe of natural rainfall infiltration, the mass transport behavior of the sodium bromide tracer relative to fluid flow, and the source of the geophysical signals. There are many approaches to gaining a deeper understanding of the heterogeneity of the site. While the electrical resistivity and GPR surveys indicate some lateral continuity of resistivity profiles and GPR reflectors, a higher-resolution analysis of these features is needed. To achieve this, additional soil cores from outside the testing area, including within the farm field and towards the nearby river, can be examined to better comprehend the spatial variation and continuity of grain size horizons. Furthermore, to enhance the understanding of heterogeneity with depth, more soil samples from different depths should be tested for permeability and water content to understand the hydraulic behavior of the soil better. It would also be beneficial to conduct further tests to determine if the sands in the established horizons possess distinctive properties beyond grain size. To obtain long-term data on moisture content and water behavior in the soil due to precipitation, soil sensors that measure water content, electrical resistivity, and temperatures could be installed at different depths in the subsurface.

The concentration of the bromide may benefit from being increased, as the highest concentration recorded after the August 2022 experiment was 29.7 ppm one hour after infiltration and decreased significantly to the highest value recorded of 1.0 ppm 72 hours later. The initial concentration of bromide in the sodium bromide solution was about 2,000 ppm, and we saw the highest bromide concentration at approximately 30 ppm one hour after infiltration.

This immense difference in the initial bromide concentration of the solution and what we were seeing in the soil water chemistry of the samples one hour after infiltration indicates a vast dispersion and dissipation of bromide ions shortly after injection. Because this difference is so significant, it may be worth increasing the initial concentration of the sodium bromide solution to gain a better insight into the behavior of the solution over time. In addition, the increase in concentration might increase the electrical resistivity signals, further highlighting spatial variations in the layers. However, the existing solution may have disrupted the signals that could have come from freshwater, making it difficult to interpret whether the preferential flow assumed was the high salinity solution or the freshwater being pushed from the infiltration experiment.

The challenges faced in this research underscore the difficulties in investigating unsaturated flow processes in the field due to their temporal and spatial variations at different scales. The different sensitivities and resolutions of the techniques used in this study and the potential impact of data processing on results further complicate the comparison of findings. Invasive methods were crucial in supporting geophysical signals, as they can be complex to interpret and may not provide small-scale observations that can influence system responses. Forward modeling of ERT and GPR signals in response to hydrologic processes could enhance geophysical data analysis. The GPR data also contains valuable delay-time and attenuation information that could be further analyzed to gain insights into infiltration dynamics. Incorporating soil moisture sensors for monitoring field characteristics and understanding temporal variations in water content could be a potential avenue for future research.

Continuing this research, we could better comprehend preferential flow behavior from directional plume development and identify where contaminants might be retained according to the composition of the soil layers on the near-surface. Soil heterogeneities played a significant role in the directional behavior of pollutants and were mostly dictated by the grain size distribution and soil water content. These findings have implications for understanding the timeline of contaminant infiltration in agricultural environments and help further understand the effect of subsurface heterogeneities in infiltration mechanisms.

A.6. References

Advanced Geosciences, Inc. (AGI). (2017). Dipole-dipole array: electrical resistivity methods, part 3. URL: https://www.agiusa.com/dipole-dipole%E2%80%8B-%E2%80%8Barray%E2%80%8B [Accessed March 27, 2023]

Anderson, M. P. and Woessner, W. W. (1991). Chapter 12: Advanced Topics. In Applied Groundwater Modeling: Simulation of Flow and Advective Transport (pp. 316-341). Academic Press. https://doi.org/10.1016/B978-0-08-088694-7.50017-1

Angulo-Jaramillo, R., Vandervaere, J. P., Roulier, S., Thony, J. L., Gaudet, J. P., and Vauclin, M. (2000). Field measurement of soil surface hydraulic properties by disc and ring infiltrometers. Soil and Tillage Research, 55(1-2), 1–29. https://doi.org/10.1016/s0167-1987(00)00098-2

Annan, A.P. (2005). GPR methods for hydrogeological studies. In Y. Rubin and S.S. Hubbard (Eds.), Hydrogeophysics (pp. 185-214). Springer.

ASTM. (2014). The importance of particle size distribution is emphasized in the proposed ASTM soil and rock standards. URL: https://newsroom.astm.org/importance-particle-size-distribution-emphasized-proposed-astm-soil-and-rock-standards [Accessed March 29, 2023]

ASTM Standard D6913/D6913M, 2021, “Test Methods for Particle-Size Distribution (Gradation) of Soils Using Sieve Analysis,” ASTM International, West Conshohocken, PA, 2003, https://doi.org/10.1520/D6913_D6913M-17

Bot, A. and Benites J. (2005). Chapter 5: Creating drought-resistant soil. In The importance of soil organic matter: Key to drought-resistant soil and sustained food production (pp. 35-40). Food and Agriculture Organization of the United Nations.

Buckingham, E. (1907). Studies on the movement of soil moisture. US Department of Agriculture, Bureau of Soils (No. 38). URL: https://ia802908.us.archive.org/0/items/studiesonmovemen38buck/studiesonmovemen38buck.pdf

Cates, R. (1991). Drinking water and groundwater quality in the lower Wisconsin River Valley (Report No. DNR-078). Wisconsin Department of Natural Resources. URL: https://www.wri.wisc.edu/wp-content/uploads/DNR-078.pdf

Cey, E.E. and Rudolph, D.L. (2009). Field study of macropore flow processes using tension infiltration of a dye tracer in partially saturated soils. Hydrological Processes, 23(12), 1768–1779. https://doi.org/10.1002/hyp.7302

Clayton, L. and Attig, J. W. (1990). Geology of Sauk County, Wisconsin. Wisconsin Geological and Natural History Survey. URL: https://wgnhs.wisc.edu/catalog/publication/000317

Clean Wisconsin. (2022). Protecting drinking water from nitrate pollution. URL: https://www.cleanwisconsin.org/our-work/water/nitrates/#:~:text=Research%20shows%20that%20in%20Wisconsin,access%20to%20clean%20drinking%20water. [Accessed January 31, 2023]

Davis, S. N., Thompson, G. M., Bentley, H. W., and Stiles, G. (1980). Ground-water tracers - a short review. Ground Water, 18(1), 14-23. https://doi.org/10.1111/j.1745-6584.1980.tb03366.x

Doerr, S. H. (1998). On standardizing the 'water drop penetration time' and the 'molarity of an ethanol droplet' techniques to classify soil hydrophobicity: A case study using medium textured soils. Earth Surface Processes and Landforms, 23(7), 663-668. https://doi.org/10.1002/(SICI)1096-9837(199807)23:7%3C663::AID-ESP909%3E3.0.CO;2-6

Electrical resistivity tomography (ERT). (2020). Geophysical Survey Company - TerraDat (UK) Ltd. URL: https://www.terradat.co.uk/survey-methods/resistivity-tomography/ [Accessed February 14, 2023]

Environmental Protection Agency (EPA). (2009). National Primary Drinking Water Regulations. EPA 816-F-09-004. EPA. URL: https://www.epa.gov/ground-water-and-drinking-water/national-primary-drinking-water-regulations [Accessed February 1, 2023]

Everett, M. E. (2013). Near-surface applied geophysics. Cambridge University Press.

Farthing, M.W. and Ogden, F.L. (2017). Numerical solution of Richards' equation: A review of advances and challenges. Soil Science Society of America Journal, 81(6), 1257-1269. https://doi.org/10.2136/sssaj2017.02.0058

Flury, M. and Papritz, A. (1993). Bromide in the natural environment: Occurrence and toxicity. Journal of Environmental Quality, 22(4), 747-758. https://doi.org/10.2134/jeq1993.00472425002200040017x

Fritz, J. S. and Gjerde, D. T. (2000). Ion chromatography. Wiley-VCH.

Green, C. T., Fisher, L. H., and Bekins, B. A. (2008). Nitrogen fluxes through unsaturated zones in five agricultural settings across the United States. Journal of Environmental Quality, 37(3), 1073-1085. https://doi.org/10.2134/jeq2007.0010

Gotkowitz, M. B., Zeiler, K. K., Dunning, C. P., Thomas, J. C., and Lin, Y. F. (2005). Hydrogeology and simulation of groundwater flow in Sauk County, Wisconsin. Wisconsin Geological and Natural History Survey.

Haddad, P. R. and Jackson, P. E. (1990). Ion chromatography - principles and applications. Journal of Chromatography Library, 46, 1-776. https://doi.org/10.1016/s0301-4770(08)61159-8

Haeni, F. P., McKeegan, D. K., and Capron, D. R. (1987). Ground-penetrating radar study of the thickness and extent of sediments beneath Silver Lake, Berlin and Meriden, Connecticut (Report No. 85-4108). United States Geological Survey. URL: https://pubs.usgs.gov/wri/1985/4108/report.pdf

Hazen, A. (1893). Some physical properties of sands and gravels with special reference to their use in filtration. 24th Annual Report, Massachusetts, State Board of Health.

Jol, H. (2009). Ground penetrating radar theory and applications. Elsevier Science.

KBGPR Surveys (2023). Module 3.4: GPR resolution. URL: https://kbgprsurveys.co.uk/gpr-training/module-3-4-gpr-ground-penetrating-radar-resolution/ [Accessed March 31, 2023]

Laine, D. (2021). Nitrate contamination - the NR 151 Draft Rule in Wisconsin. River Alliance of Wisconsin. URL: https://wisconsinrivers.org/nitrate-groundwater-nr151/ [Accessed January 26, 2023]

Lassabatere, L., Di Prima, S., Bouarafa, S., Iovino, M., Bagarello, V., and Angulo-Jaramillo, R. (2019). BEST-2K method for characterizing dual-permeability unsaturated soils with

ponded and tension Infiltrometers. Vadose Zone Journal, 18(1), 1-20. https://doi.org/10.2136/vzj2018.06.0124

Liu, X., Chen, J., Cui, X., Liu, Q., Cao, X., and Chen, X. (2017). Measurement of soil water content using ground-penetrating radar: A review of current methods. International Journal of Digital Earth, 12(1), 95-118. https://doi.org/10.1080/17538947.2017.1412520

Murthy, V. N. S. (2002). Geotechnical engineering: Principles and practices of soil mechanics and foundation engineering. CRC Press.

Natural Resources Conservation Service (NRCS). (2000). Soil Quality Resource Concerns: Hydrophobicity. United States Department of Agriculture. URL: https://www.fs.usda.gov/Internet/FSE_DOCUMENTS/stelprdb5293766.pdf

Neyamadpour, A., Wan Abdullah, W. A., Taib, S., and Neyamadpour, B. (2010). Comparison of Wenner and dipole–dipole arrays in the study of an underground three-dimensional cavity. Journal of Geophysics and Engineering, 7(1), 30-40. https://doi.org/10.1088/1742-2132/7/1/003

Ochsner, T. (2019). Chapter 4: Soil water flow. In Rain or shine: An introduction to soil physical properties and processes (pp. 97-111). Oklahoma State University Libraries. https://doi.org/https://doi.org/10.22488/okstate.21.000000

Olorunfemi, I. (2014). Soil hydrophobicity: An overview. Journal of Scientific Research and Reports, 3(8), 1003-1037. https://doi.org/10.9734/jsrr/2014/7325

Preene Groundwater Consulting (PGC). (2014). Assessing hydraulic conductivity of soils from particle size data. URL: https://www.preene.com/blog/2014/08/assessing-hydraulic-conductivity-of-soils-from-particle-size-data [Accessed March 29, 2023]

Sensors & Software (S&S). (2023). What is ground penetrating radar (GPR)?. URL: https://www.sensoft.ca/blog/what-is-gpr/ [Accessed March 31, 2023]

Swager, K. (2021). Time-lapse geophysics and characterization of an infiltration experiment in unsaturated Wisconsin alluvial sediments [Unpublished master's thesis]. University of Wisconsin-Madison.

Thermo Fisher Scientific (TFS). (2018). Thermo Scientific Dionex IonPac IC column selection guide. URL: https://mz-at.de/fileadmin/user_upload/Brochures/thermo_ic-column-selection-guide.pdf

Tindall, J. A., Kunkel, J. R., and Anderson, D. E. (1999). Chapter 8: Unsaturated water flow in soil. Unsaturated zone hydrology for scientists and Engineers (pp. 183-199). Prentice Hall.

Nimmo, J. R. (2005). Part 13: groundwater, 150 unsaturated zone flow processes. In M. G. Anderson and J. J. McDonnell (Eds.), Encyclopedia of Hydrological Sciences (pp. 2299-2322). John Wiley & Sons, Ltd. https://doi.org/10.1002/0470848944.hsa161

Utsi, E. C. (2017). Chapter 1: Fundamentals of GPR operation. In Ground penetrating radar: Theory and practice (pp. 1-11). Butterworth-Heinemann.

University of Wisconsin-Stevens Point (UWSP). (2023). Well Water Quality Viewer: Private Well Data for Wisconsin. Center for Watershed Science and Education. URL: https://gissrv3.uwsp.edu/webapps/gwc/pri_wells/. [Accessed on March 27, 2023]

Ward, M. H. (2009). Too much of a good thing? Nitrate from nitrogen fertilizers and cancer. Reviews on Environmental Health, 24(4), 357-363. https://doi.org/10.1515/reveh.2009.24.4.357

Wisconsin Department of Health Services (WDHS). (2020). Nitrate in private wells. URL: https://www.dhs.wisconsin.gov/water/nitrate.htm [Accessed on December 7, 2022]

Wisconsin Department of Natural Resources (WDNR). (2022). Geology: Lower Wisconsin state riverway. URL: https://dnr.wisconsin.gov/topic/lands/lowerwisconsin/geology [Accessed February 13, 2023]

Weiss, J. (2004). Handbook of Ion Chromatography. Wiley-VCH.

Wilderer, P. A., Leibundgut, C., and Seibert, J. (2011). Chapter 2.09 - Tracer hydrology. In Treatise on water science (pp. 215-234). Elsevier Science.

Witten, A. J. (2014). Handbook of geophysics and archaeology. Routledge.

Part B: Evaluation of Geophysical Techniques for the Determination of Bedrock Depth

B.0. Abstract

We studied different near-surface geophysical surveys as measurement techniques to comply with the requirement of Wisconsin's N.R. 151 *Maximum liquid manure application rates for Silurian bedrock as a function of depth.* We evaluated ground penetrating radar, electrical resistivity, electromagnetics, and seismic refraction techniques. We assessed penetration depth, sensitivity, ease of deployment and interpretation, and implementation cost. Each method has pros and cons that might help regulators and farmers decide on selecting one type of sensor over others. We found that electrical resistivity, while it can be relatively slow to deploy, is a geophysical technique that allows reaching the depth of penetration and the needed resolution by changing electrode separation; the collected data has a high signal-to-noise ratio, a single person can deploy and operate the instrument, it is a relatively cheap instrument, and the interpretation is relatively simple. If a higher data collection rate is desired, we recommend using electromagnetic sensors. However, the instruments require careful and frequent calibrations, and users should carefully when designing and running the surveys to maintain data quality.

B.1. Depth to Bedrock Measurements

To comply with regulation Wisconsin's N.R. 151 (https://docs.legis.wisconsin.gov/code/admin_code/nr/100/_151.pdf), farmers and regulators need to determine the depth of bedrock across farms, as shallower bedrock depths limit the amounts of manure that can be spread on the field (Table B.1). Traditionally, farmers use a push rod to measure the depth to bedrock based on depth or refusal. However, the technique can only assess bedrock depths to

about 1.5 m (5 ft.), it is localized (i.e., it can give shallow depths deposits when the rod hits erratic boulders or higher depths when the rod hits sinkholes on Karst formations), and it is a technique that is physically intensive on the operator.

Table B.1. Maximum liquid manure application rates for Silurian bedrock as a function of depth (after N.R. 151)

Soil Texture	0.6 to 0.9 m depth (L/Ha/yr)	2 to 3 ft. depth (gal/ac/yr)	0.9 to 1.5 m depth (L/Ha/wk)	3 to 5 dt. depth (gal/ac/wk)	1.5 to 6 m (L/Ha/wk)	5 to 20 ft. depth (gal/ac/wk)
Sand	58725	6,750	58725	6,750	117450	13,500
Sandy Loam	117450	13,500	117450	13,500	234,900*	27,000*
Loam	117450	13,500	117450	13,500	234,900*	27,000*
Silt Loam	117450	13,500	117450	13,500	234,900*	27,000*
Clay Loam	117450	13,500	117450	13,500	174,000*	20,000*
Clay	58725	6,750	58725	6,750	117450	13,500

*It is anticipated that this rate would exceed the UW A2809 annual (crop year) application rate

So, we evaluated several geophysical techniques to assess their implementation in farming practices as alternatives to push-rod measurements. We tested electrical resistivity, electromagnetic surveys, ground penetrating radar, and seismic refraction methods. We modeled the survey techniques, collected and interpreted field data, evaluated field deployment methodologies, and assessed the interpretation easiness. All those studies were implemented to develop recommendations for the most efficient measurement methodologies.

In addition, we tested the proposed techniques in different Wisconsin regions to generalize our analyses and observations. Based on our results, we advanced two geophysical methods, i.e., electrical resistivity tomography and electromagnetism, as the most efficient methodologies to determine bedrock depths in farm parcels. We justify our recommendations on the range of penetration, resolution, instrumentation cost, easiness of operation, and interpretation.

B.2. Geophysical Measurements

B.2.1 Electrical Resistivity Tomography

Electrical Resistivity Tomography (ERT) is used to image the electrical resistivity distribution of near-surface environments. This technique injects electrical currents into the ground through metal electrodes, creating a voltage field (Keary et al. 2002). The created voltage field is sensed with a range of electrode pairs on the boundaries of the medium (Figure B.1). This process repeats for a large combination of current and voltage electrodes (Figure B.2). A typical configuration of electrodes is the dipole-dipole array (Figure B.2). This configuration was used in our surveys as it provides a good compromise between horizontal resolution and depth coverage. The resolution quality of the technique is further controlled by the spacing 'a' between electrodes (Zonge et al. 2005, Neyamadpour et al. 2010) at the expense of the depth of the surveying, giving a maximum separation 'n·a' between a pair of current and voltage electrodes (Figure B.2).

The resistivity ρ of a material describes the resistance to conduct electricity (Witten 2014). In soils and rocks, resistance is inversely proportional to the pore fluid's porosity, degree of saturation, and electrical conductivity and is directly proportional to the particle size (Attia et al. 2007). Figure B.3 summarizes the range of electrical resistivity for common rocks and soils. Note that a resistivity of about 1000 Ωm provides a practical contrast between the resistivity of most soils, sediments, and rocks. We initially considered this contrast to detect the rock depth using electrical resistivity surveys, although this value might range depending on the local weathering conditions.

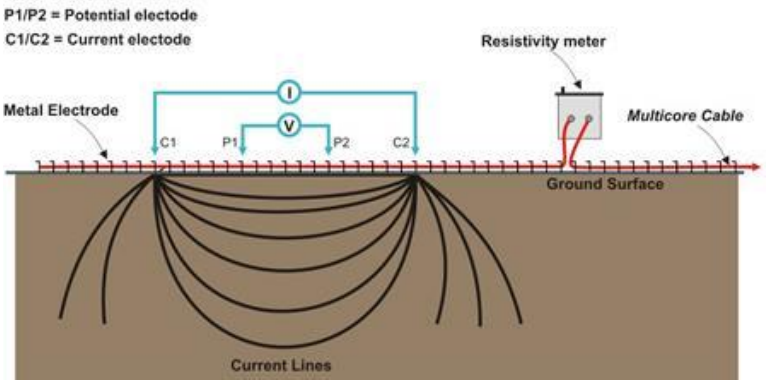

Figure B.1: General resistivity principle of electrical resistivity tomography (after ERT 2020).

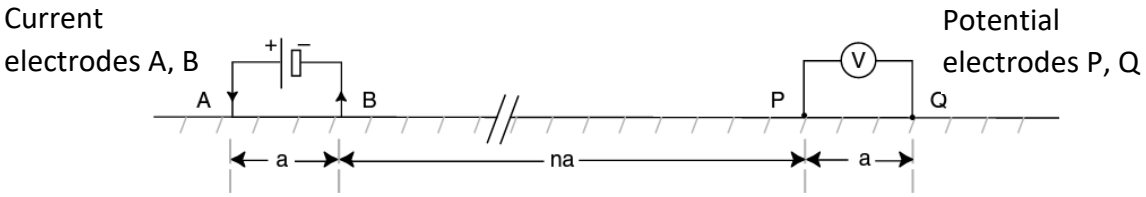

Figure B.2: Arrangement of a dipole-dipole electrical resistivity array (Everett 2013).

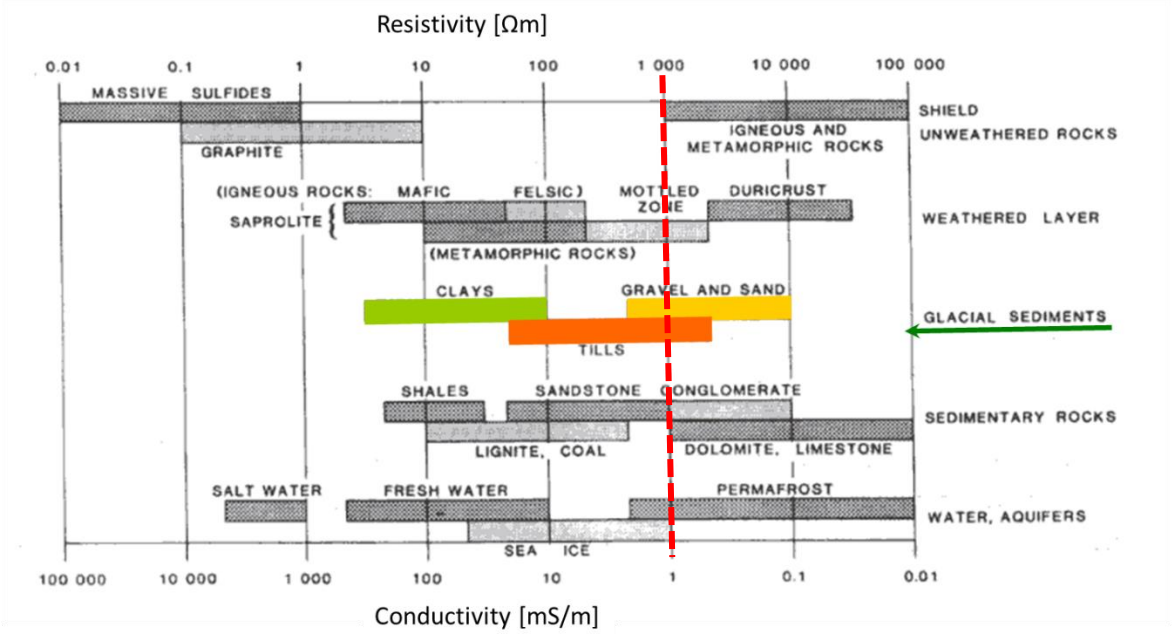

Figure B.3: Range of electrical resistivity in common soils and rocks (after Sharma 1997).

Using the notation presented in Figure B.2, the voltage difference ΔV measured across current electrodes P and Q, and the electrical current I applied between electrodes A and B can be used to calculate the apparent resistivity ρ_a as:

$$\rho_a = \pi(n+1)(n+2)na\frac{\Delta V}{I} \quad \text{B.1}$$

where n is the factor that indicates the separation between the pairs of current and voltage electrodes, and the measured apparent resistivity of the soil is the resistivity that a homogenous soil would have for the given array geometry; however, most soils show resistivity distributions and the measure of the apparent resistivity changes with the array geometry. So, to capture that resistivity distribution, measurements are repeated for all current and potential electrode pairs, resulting in enough data to obtain resistivity distribution images of the near subsurface (Everett 2013). This technique uses electrical resistivity tomography to locate the bedrock depth across farm fields *electrically*. We indicate that the depth of bedrock is located *electrically* because we determine the interface using electrical contrasts. In the case of hydrogeological studies, this electrical contrast is typically related to contrast in hydraulic conductivity (EPA 2023). It is important to note that the technique can determine the bedrock depth below an erratic boulder or the presence of filled sinkholes. In this way, electrical resistivity tomography solves one of the main drawbacks of using push rods to determine the depth of bedrock.

B.2.2 Electromagnetism

Electromagnetic geophysical instruments operate by the induction of electromagnetic fields in the subsurface. Induction describes how electromagnetic forces from a transmitter affect its surroundings without the device being in contact with the medium. The electromagnetic instrumentation includes an AC electrical current generator, transmitter and receiver coils, notch filters, data acquisition systems, and a GPS receiver.

The time-varying electric current is run through the transmitter coil during the electromagnetic surveying. The current produces a primary time-varying magnetic field as represented by Ampere's law. This law describes the magnetic field strength B_p resulting from an electric current I as:

$$\nabla \times \mu B_p = I \qquad \text{B.2}$$

where μ is the magnetic permeability of the medium being excited, ∇ is the gradient operator, and $\times$ is the cross product. The primary magnetic field then induces a electrical field E in the ground, a process that Faraday-Lenz's Law of Induction governs this response:

$$\nabla \times E = -\frac{\partial B_p}{\partial t} \qquad \text{B.3}$$

Eq. B.3 describes how a time-varying magnetic field B induces time-varying electric fields E that opposes the change generated by the time-varying magnetic field. If the material has electrical conductivity σ, the electric fields create secondary currents I_s (=σ·E) in the subsurface. The electrical currents I_s formed in the subsurface are called eddy currents. These eddy currents, in turn, produce a secondary magnetic field (B_s) and induce a current in the receiving coil (again, described by Faraday-Lenz's Law).

The voltage in the receiving coil is the vector sum of the primary and secondary magnetic fields. The primary and secondary field sinusoidal signals differ in phase, with the secondary field being a function of the ground conductivity. Under the low-induction number regime (i.e., the coil separation s is much smaller than the skin depth $S_d = (\pi \cdot f \cdot \mu_0 \cdot \sigma)^{-1/2}$, where ε is the dielectric permittivity of the medium, μ_0 is the magnetic permeability of the free space, and f is the

frequency of the time-varying current), the ratio of the secondary and primary fields can be used to solve for the apparent conductivity σ_a of the ground using this equation (McNeill980; Callegary et al. 2007): $\sigma_a \approx \frac{2}{\pi f \mu_0 s^2}\left(\frac{B_s}{B_p}\right)$.

The critical question regarding applying the technique to spreading manure on farm fields (i.e., the N.R. 151 regulation) across Wisconsin is the depth sensitivity of the method. The answer to that question depends on the instrument and the orientation of the coils.

This study used two different EM instruments: Geonics EM-31 and Dualem-42. These instruments are portable and sensitive to depths of around 6 m and deeper (well within the range of interest of the N.R. 151 regulation). The Geonics EM-31 instrument with 3.7 m coil separation operates in two modes (i.e., horizontal dipole and vertical dipole) by rotating the instrument by 90 degrees to change the direction of the magnetic dipole (Figure B.4). Depending on the dipoles' orientation and elevations, the volume below the instrument changes and has different sensitivity functions. Those effects are modeled with the functions R's for the cumulative weight distributions:

$$\text{the } R_h(z) = \sqrt{4z^2 + 1} - 2z \text{ horizontal dipole} \quad \text{B.4}$$

$$R_v(z) = \frac{1}{\sqrt{4z^2+1}} \text{ vertical dipole} \quad \text{B.5}$$

$$R_{perp}(z) = 1 - \frac{2z}{\sqrt{4z^2+1}} \text{ perpendicular dipole} \quad \text{B.6}$$

where z is the normalized depth of the layer interface concerning the instrument height concerning the dipole separation s. The profiles vs. normalized depth for these equations and their derivatives ϕ, are presented in Figure B.5.

These equations provide models to calculate the measured apparent conductivity σ_a in horizontally layered systems (McNeill 1980; Burger et al. 2006):

$$\sigma_a = \sigma_1\big(1 - R_i(z_1)\big) + \sigma_2 R_i(z_1) \textit{ for a two-layer system} \quad \text{B.7}$$

$$\sigma_a = \sigma_1\big(1 - R_i(z_1)\big) + \sigma_2\big(R_i(z_1) - R_i(z_2)\big) + \sigma_3 R_i(z_2) \textit{ for a three-layer system} \quad \text{B.8}$$

Eqs. B.7 and B.8 apply to the electromagnetic sensor sitting on the ground. However, McNeill (1980) and Milson (2010) indicate that changing the elevation of the sensor above the ground also provides information about conductivity distribution and layer thickness.

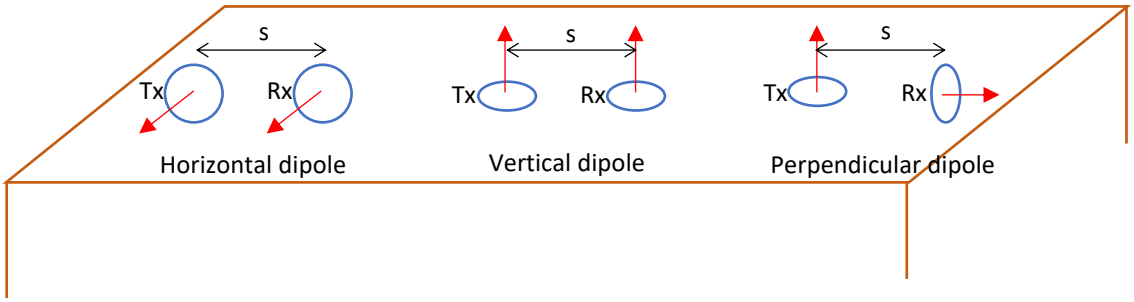

Figure B.4. Horizontal dipole, vertical dipole, and perpendicular modes (Adapted from McNeill, 1980). Geonics EM-31 uses horizontal and vertical dipole configurations, and Dualem-42 uses vertical and perpendicular dipole configurations.

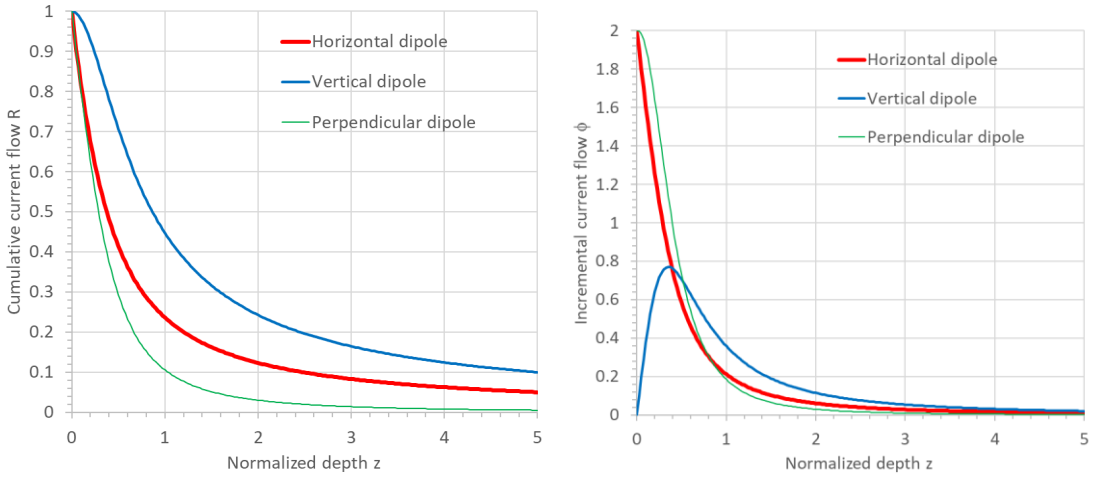

(a) (b)

Figure B.5. (a) Cumulative current flow R and (b) the incremental current ϕ (i.e., the derivative of R) as a function of the normalized depth z for vertical, horizontal, and perpendicular dipole modes (adapted from McNeill 1980; Fetterman and Labson 2005; Milson 2010; Dualem 2023).

We tested that possibility by assuming that the air between the instrument and the ground can be considered a zero-conductivity layer in the equations for apparent conductivity. Then, for a case of a homogenous conductivity layer, the two-layer system equation applies, and the normalized depth is $z_1 = h/s$, where h is the sensor elevation, $\sigma_1 = 0$ S/m is the conductivity of the air, and σ_2 is the conductivity of the homogenous subsurface. For the case of a two-layer subsurface, the three-layer systems equation applies. Then $z_1 = h/s$ and $z_2 = (h+d)/s$, where d is the depth of the interface in the subsurface, and σ_1, σ_2, and σ_1 are the conductivities of the air, first subsurface layer, and second subsurface layer. The results of applying these models match the data from McNeill's (1980) Figure 14, modified into Figure B.6.

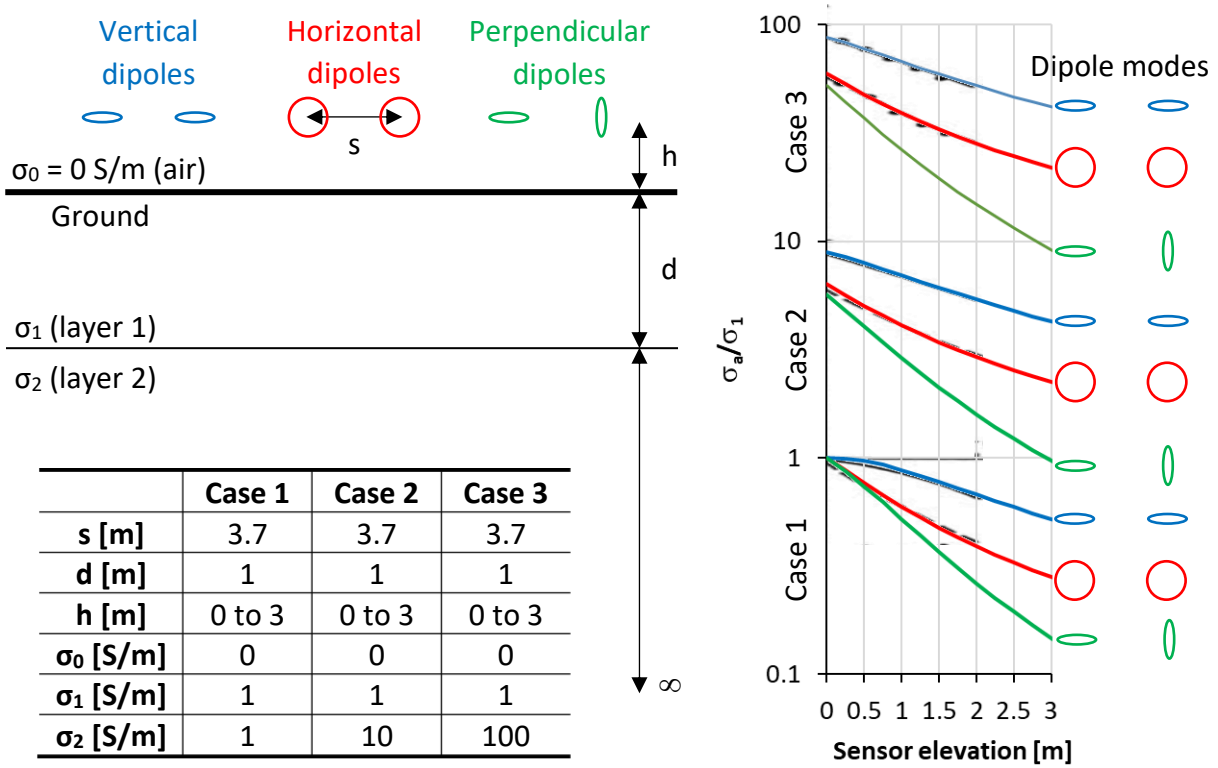

	Case 1	Case 2	Case 3
s [m]	3.7	3.7	3.7
d [m]	1	1	1
h [m]	0 to 3	0 to 3	0 to 3
σ_0 [S/m]	0	0	0
σ_1 [S/m]	1	1	1
σ_2 [S/m]	1	10	100

Figure B.6: Model response of a two-layer system for different sensor elevations. The black points and lines results correspond to vertical and horizontal dipoles' data in Figure 14 of McNeill (1980). In our study, we extended the results for the perpendicular dipole mode.

B.2.3 Ground Penetrating Radar

Ground Penetrating Radar (GPR) is a geophysical technique that sends electromagnetic (EM) pulses into the subsurface. These pulses reflect, refract, scatter, and diffract when they encounter electromagnetic heterogeneities withing a host medium. A complete GPR kit includes a high-speed data acquisition system, digital electronics that create EM signals, and 10 MHz to 2 GHz transmitting and receiving antennas. The antennas are usually located at a fixed distance and are moved simultaneously across the ground surface while collecting data. The received EM pulses from anomalies with contrasting electromagnetic properties, such as those associated with changes in soil or rock properties, buried structures, cavities, or water tables (Haeni et al. 1987, Everett 2013, Witten 2014), are captured. GPR uses the amplitude and travel times of the arriving reflected and diffracted EM waves to create images of electromagnetic anomalies within the subsurface (Annan 2005 – Figure B.6).

Collected signals are plotted as traces on a radargram in real-time using the survey's elapsed time and the antenna pair's horizontal locations. Since these signals mainly rely on soil permittivity, heterogeneities in the subsurface can be inferred at different depths (Witten 2014, Liu et al. 2017). The radargram can then be converted from time to depth to model the results of a subsurface profile (Figure B.7).

GPR surveys are commonly used in geologic investigations to determine the location and properties of buried objects, structures, materials, subsurface cavities, and heterogeneities within near-surface sediments (Utsi 2017).

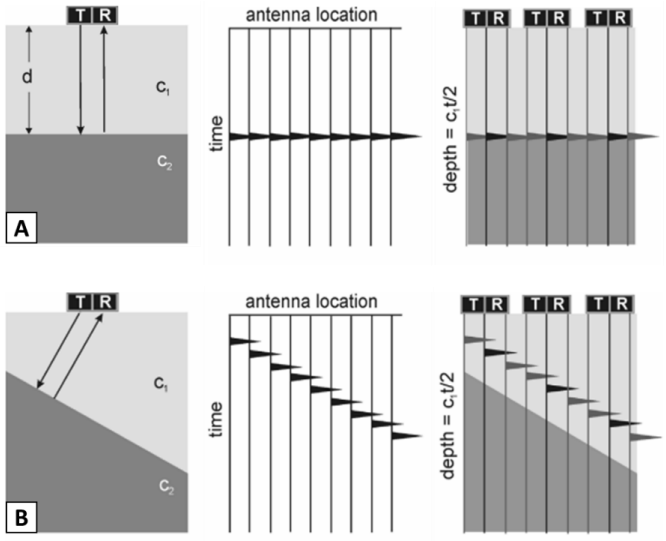

Figure B.7: A) Example of the concept and results created from a GPR system for a horizontal interface and a B) sloping interface. The radargram is converted from time to depth to model the subsurface geometry (after Witten 2014).

As the EM waves propagate, they interact with the subsurface's electrical conductivity and dielectric permittivity changing their velocity. So, the interpretation of the data depends on the distribution of those properties, including assessing the depth of the anomalies. GPR signals show the two-way travel time t of the reflected waves created from subsurface interfaces and anomalies. So, to determine the depth d (assuming collocated transmitted and receiving antennas), by knowing the EM subsurface speed V of the subsurface:

$$\mathrm{d} = \frac{Vt}{2} \qquad \text{B.9}$$

The EM wave speed V and attenuation α are dependent on the relative real dielectric permittivity ε'_r and the effective conductivity σ of the medium, and the frequency f of the deployed antennas (Santamarina et al. 2001):

$$V = \frac{c_o}{\sqrt{\frac{\varepsilon'_r}{2}\left[\sqrt{1+\left(\frac{\sigma}{2\pi f \varepsilon'_r \varepsilon_o}\right)^2}+1\right]}} \text{ EM wave speed} \quad \text{B.10}$$

$$\alpha = \frac{2\pi f}{c_o}\sqrt{\frac{\varepsilon'_r}{2}\left[\sqrt{1+\left(\frac{\sigma}{2\pi f \varepsilon'_r \varepsilon_o}\right)^2}-1\right]} \text{ EM wave attenuation} \quad \text{B.11}$$

where $c_o=3\cdot10^8$ m/s is the speed of light in free space, $\varepsilon_o=8.85\cdot10^{-12}$ F/m is the dielectric permittivity of the free space, and ε''_r is the relative real dielectric permittivity. Both relative real dielectric permittivity and electrical conductivity are functions of porosity degree of saturation and mineralogy. In addition, electrical conductivity is a function of the pore fluid conductivity and specific surface area (Santamarina et al. 2005).

If the conductivity of the medium decreases to zero, these two equations simplify to:

$$V = \frac{c_o}{\sqrt{\varepsilon'_r}} \quad \text{B.12}$$

$$\alpha = 0 \quad \text{B.13}$$

Those simplifications are typically used to interpret near-surface geophysical data and indicate that GPR signals do not undergo material attenuation and that speed is independent of the antenna frequency. While these assumptions are valid in simple interpretations, they limit understanding of the use of GPR in a medium with moderate electrical conductivity. For example, both resolutions $R=\lambda/2$ and penetration depth ($\sim S_d$) are controlled by both the antenna frequency and the electrical conductivity of the medium, where $\lambda=V/f$ is the wavelength, and $S_d=1/\alpha$ is the skin depth (Figure B.8).

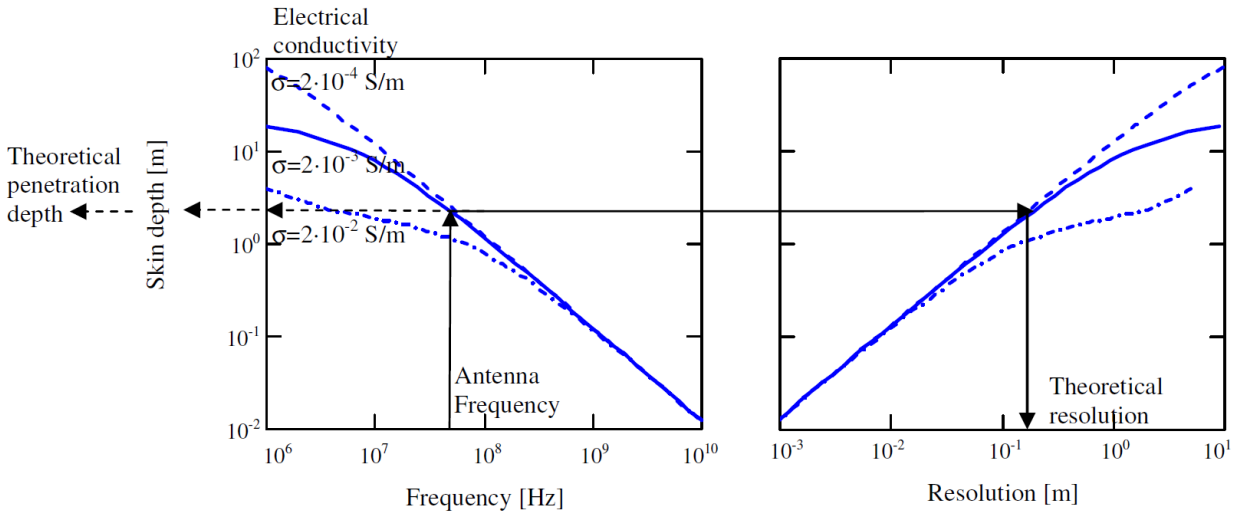

Figure B.8: Theoretical resolution and penetration depth for GPR systems under different frequencies and electrical conductivity medium (Lowry et al. 2009).

Because the transmitting and receiving antennas are assumed to be located at a point, the amplitude of the waves attenuates as the wavefront increases, known as geometric spreading, and it is independent of the propagating frequency (Annan 2005, Witten 2014). However, material attenuation is frequency-dependent on materials with moderate to high electrical conductivity. So, material attenuation and image resolution characteristics are why selecting antenna frequencies is essential while conducting GPR surveys. Different antenna frequencies are used to reach varying depths or achieve different resolutions depending on the soil conditions. Lower frequencies are generally used for deeper surveys but produce coarse resolutions, while higher frequencies are used for shallower investigations and finer resolutions (Jol 2009). The GPR results are processed and analyzed to create two-dimensional or three-dimensional subsurface images. This geophysical survey method was used throughout the experiments to assess the soil permittivity directly below and around the injection site of each infiltration experiment.

B.2.4 Seismic Refraction

Seismic refraction is a seismic geophysical technique used in layered media with seismic velocity increasing with depth. By creating seismic waves and monitoring first arrivals along both directions a line of geophones (Figure B.9), geophysicists can determine the velocity of different layers (V_1, V_2, V_i…), the depth to refractors (based on the delay times t_i and t'_i), and dipping angles γ. In the case of this study, the significant increase in seismic wave velocity from surface sediments to bedrock makes seismic refraction a natural technique. The challenge, however, is to evaluate the surface and bedrock with uneven topography.

A few techniques use the first arrivals (or head waves) from both seismic sources to map the undulating bedrock-sediment interface (Keary et al. 2002; Pelton 2005). The methods are known as the *plus-minus method* and the *generalized reciprocal method*. These techniques use the sum and the difference of arrival travel time of the head waves arriving at a geophone from sources in opposite positions. The difference between the techniques is in the assumptions made and the fidelity of the results; in this document, we discuss the plus-minus method. However, the generalized reciprocal method can be used to further validate and constrain the application of the plus-minus method.

The *plus-minus method* uses the sum and the difference of the travel times from refracted (head) waves at a geophone coming from oppositely located seismic sources (Keary et al. 2002; Pelton 2005). Based on the configuration presented in Figure B.10, we define the reciprocal time (i.e., the travel time of the head wave from source A to B or from source B to A), the travel time from source A to geophone G, and the travel time from source B to geophone G.

$$t_{AB} = \frac{L}{V_2} + t_{iA} + t_{iB} \text{ reciprocal time} \qquad \text{B.14}$$

$$t_{AG} = \frac{x}{V_2} + t_{iA} + t_{iG} \text{ travel time from source A to geophone G} \qquad \text{B.15}$$

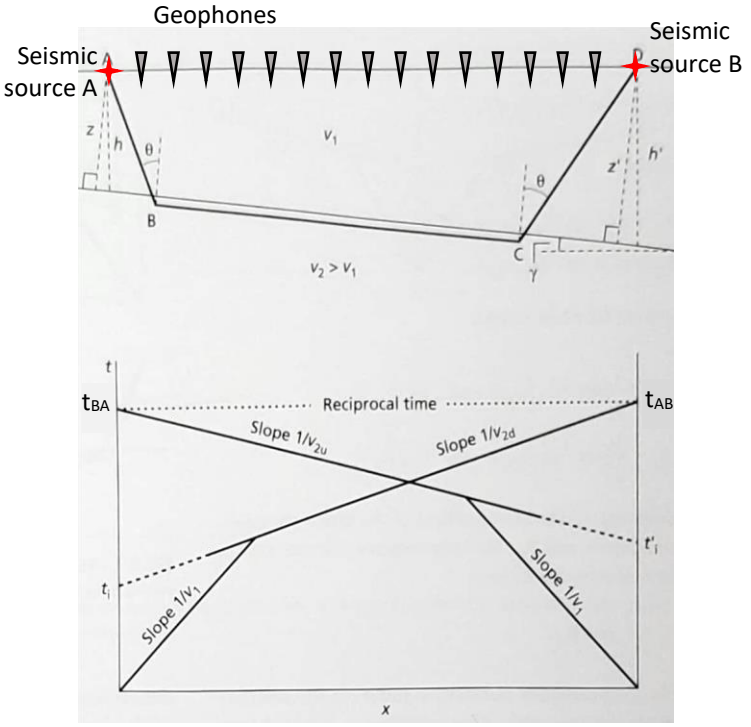

Figure B.9: Typical down and up seismic refraction surveys (after Kearey et al. 2002)

$$t_{BG} = \frac{L-x}{V_2} + t_{iG} + t_{iB} \qquad \textit{travel time from source B to geophone G} \qquad \text{B.16}$$

where t_{iA}, t_{iB}, and t_{iG} are the delay times under the sources A and B, and under geophone G. V2 is the velocity of the second layer, x is the distance from source A to geophone G, and L-x is the distance from source B to geophone G. We then define the plus time t_G as:

$$t_G = \frac{1}{2}(t_{AG} + t_{BG} - t_{AB}) \qquad \textit{plus time} \qquad \text{B.17}$$

By replacing this equation with the terms for the different travel times:

$$t_G = \frac{1}{2}\left(\frac{x}{V_2} + t_{iA} + t_{iG} + \frac{L-x}{V_2} + t_{iG} + t_{iB} - \frac{L}{V_2} - t_{iA} - t_{iB}\right) \qquad \text{B.18}$$

We can solve for the delay time under the geophone G:

$$t_G = t_{iG} = z_G \frac{\sqrt{V_2^2 - V_1^2}}{V_2^2 \cdot V_1^2} \qquad \text{B.19}$$

where V_1 is the velocity of the top layer. We use that Eq. B.19 to estimate the distance h_G from the geophone to the refractor:

$$z_G = t_G \frac{V_2^2 \cdot V_1^2}{\sqrt{V_2^2 - V_1^2}} \qquad \text{B.20}$$

In this equation, velocity V_1 is determined from the direct arrival travel time, but V_2 is unknown. To solve the velocity of the refractor, we define the minus time t_V:

$$t_V = \frac{1}{2}(t_{AG} - t_{BG} + t_{AB}) \qquad \textit{minus time} \qquad \text{B.21}$$

By replacing this equation with the terms for the different travel times:

$$t_V = \frac{1}{2}\left(\frac{x}{V_2} + t_{iA} + t_{iG} - \frac{L-x}{V_2} - t_{iG} - t_{iB} + \frac{L}{V_2} + t_{iA} + t_{iB}\right) \qquad \text{B.22}$$

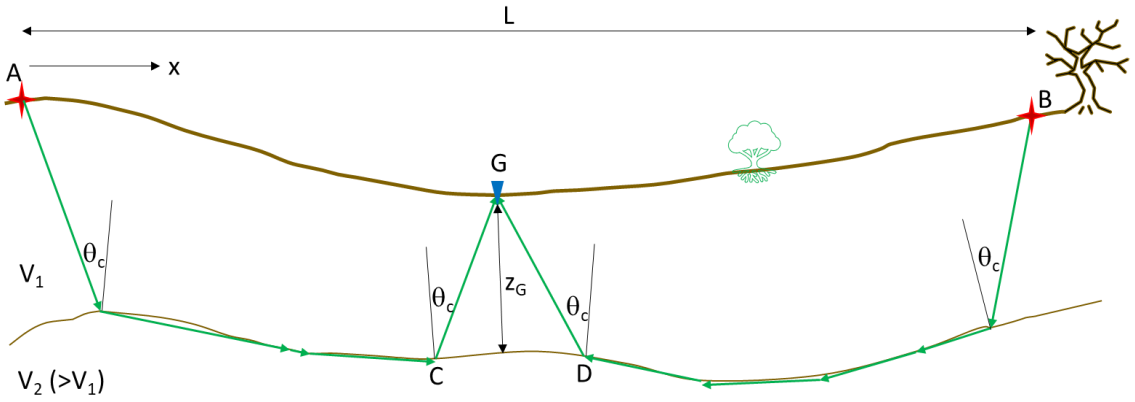

Figure B.10: Geometry for interpreting the plus-minus method for an undulating refractor.

We obtain the linear equation:

$$t_V = \frac{x}{V_2} + t_{iA} \qquad \text{B.23}$$

So, if we plot the minus time t_V for multiple geophone positions, the slope of the curve is the inverse of the refractor velocity V_2. So, using the plus and minus times definitions, the profile of the undulating refractor can be determined.

It is important to note that plus and minus times are defined from refracted travel arrivals, and the operator can evaluate that by analyzing the t_V vs. x plot when it deviated from a straight line is an indication that the travel times may be within the crossover distance and must be rejected (Kearey et al. 2002). Furthermore, this is an approximation, as x does not truly represent the path of the refracted wave along the interface. The generalized reciprocal method addresses this and other problems (Pelton 2005).

B.3. Modelling

To evaluate the application of the different geophysical techniques, we performed several numerical models to assess the sensitivity of the methods to several field scenarios, including depth sensitivity, resolution, and invertibility. We used multiple techniques, including electrical resistivity tomography, electromagnetism, and ground penetrating radar.

B.3.1 Electrical Resistivity Tomography

We used the RES2DMOD program (Loke 2016), a Rapid 2D resistivity and I.P. forward modeling that uses finite-difference and finite-element methods to model responses to electrical resistivity survey. We created different scenarios in the software to evaluate electrical resistivity response and assess the invertibility of the dipole-dipole array results. For the modeling, we used 24 electrodes with 5-m electrode dipole separation. This selection matches the type of array typically used with the IRIS Syscal Kid Switch instrument. We varied the depth to bedrock from

0.2 m, 0.4 m, 1.0 m, 2 m, 4.0 m, and 10.0 m to test the typical depths considered in N.R. 151 (surface to 20 ft or 6 m). We used electrical resistivity of 100 Ωm for the top sediments and 2000 Ωm for the dolomite bedrocks. The inverted results are documented in Figures B.11 and B.12.

Figure B.11 summarizes the results for 1-m dipole-dipole electrode separations, and Figure B.12 presents the results for 5-m dipole-dipole electrode separations. In both sets of cases, data were modeled at a maximum level separation n-9 to match the characteristics of the IRIS Syscal Kid Switch instrument. In addition, the data include 2.5% noise to make the analyses more realistic.

These results highlight some of the limitations of the ERT and the IRIS Syscal Kid Switch instrument. Individually, the 1-m m and 5-m electrode separation dipole-dipole configurations cannot detect the sediment-bedrock interface when it is less than the electrode separation, and they reach a limit of image depth of about 2.5 times the electrode separation. This limitation can be relaxed if operators collect data using multiple electrode separations. For this example, if both a = 1.0 m and a = 5.0 m are collected at the site. In this case, the depth to bedrock could be imaged from 1.0 m to about 12.0 m with the combined dataset. The results are presented in Figure B.13. The combined electrode separation allows a sense of bedrock depth from 1.0 m to about 10.0 m and allows imaging of the depth of the sediment bedrock within those ranges.

While this approach would solve the problem of imaging a more comprehensive bedrock range, it is costly. Please note that 24 electrodes with either 1 m or 5 m separations require 153 independent measurements and about 50 minutes for the measurement cycle to complete with the IRIS Syscal Kid Switch (it takes about 20 seconds per measurement with this instrument). These surveys cover about 20 m with a 1-m electrode separation and about 100 m with a 5-m electrode separation. However, if the 1-m and 5-m electrode configurations are combined, the

time for data collection dramatically increases. Covering the whole 115 m of survey length of the 5-m electrode separation requires many more 1-m electrode separation measurements. The simulation presented in Figure B.13 resulted from 1134 independent measurements, which would require about 6.3 hours to complete with the IRIS Syscal Kid Switch instrument (without accounting for positioning the electrodes)

Furthermore, based on the range of bedrock depths specified by N.R. 151 (i.e., from 0.6 m - 2 ft to 6 m – 20 ft, we could further extrapolate the results and make the case that the optimal combination of electrode separations would include 0.6 m and 3.0 m. The 0.6-m electrode separation would cover depths from around 0.6 m to 1.5 m, and the 3.0-m separation could cover depths between 3 m and 8 m. Similarly, to the results presented in Figure B.13, the combined measurement would allow imaging of the whole range of depth specified by N.R. 151. The drawback of this approach is that it would require a larger number of electrodes.

Assuming a square 16-ha (40-acre) lot, the sides are 400 m (~1300 ft), it would take about ten full days of electrical resistivity surveying to image it under the requirements by N.R. 151. Of course, the speed of data collection could be improved using more extensive and sophisticated instrumentation than the Iris Syscal Kid Switch used in this example.

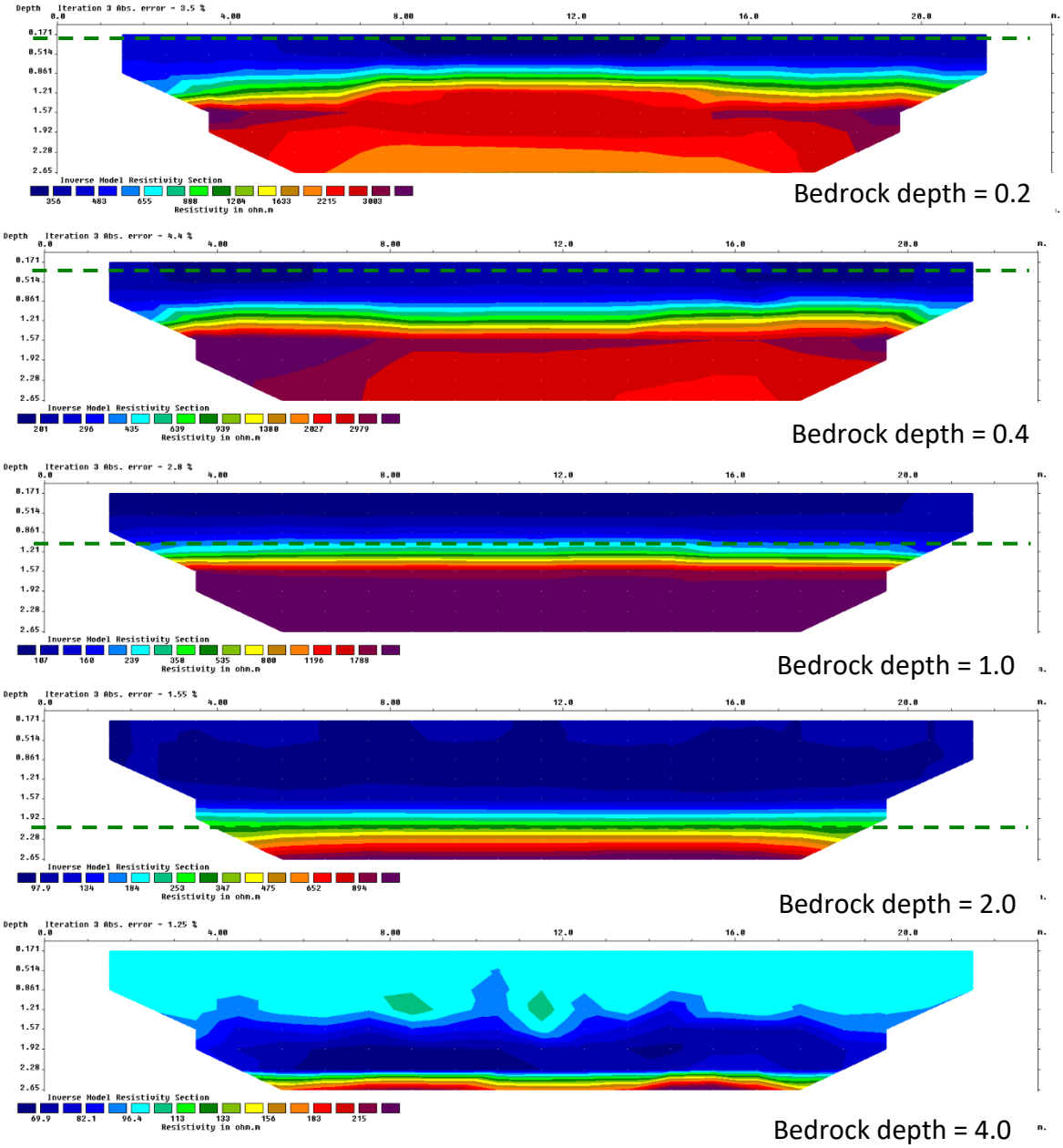

Figure B.11. RES2DINV-inverted results for 1-m dipole-dipole electrode separation modeled data with a two-layer subsurface system (100 Ωm top layer and 2000 Ωm bottom layer). The green line indicates the bedrock depth in the model (The color scale is different for each panel).

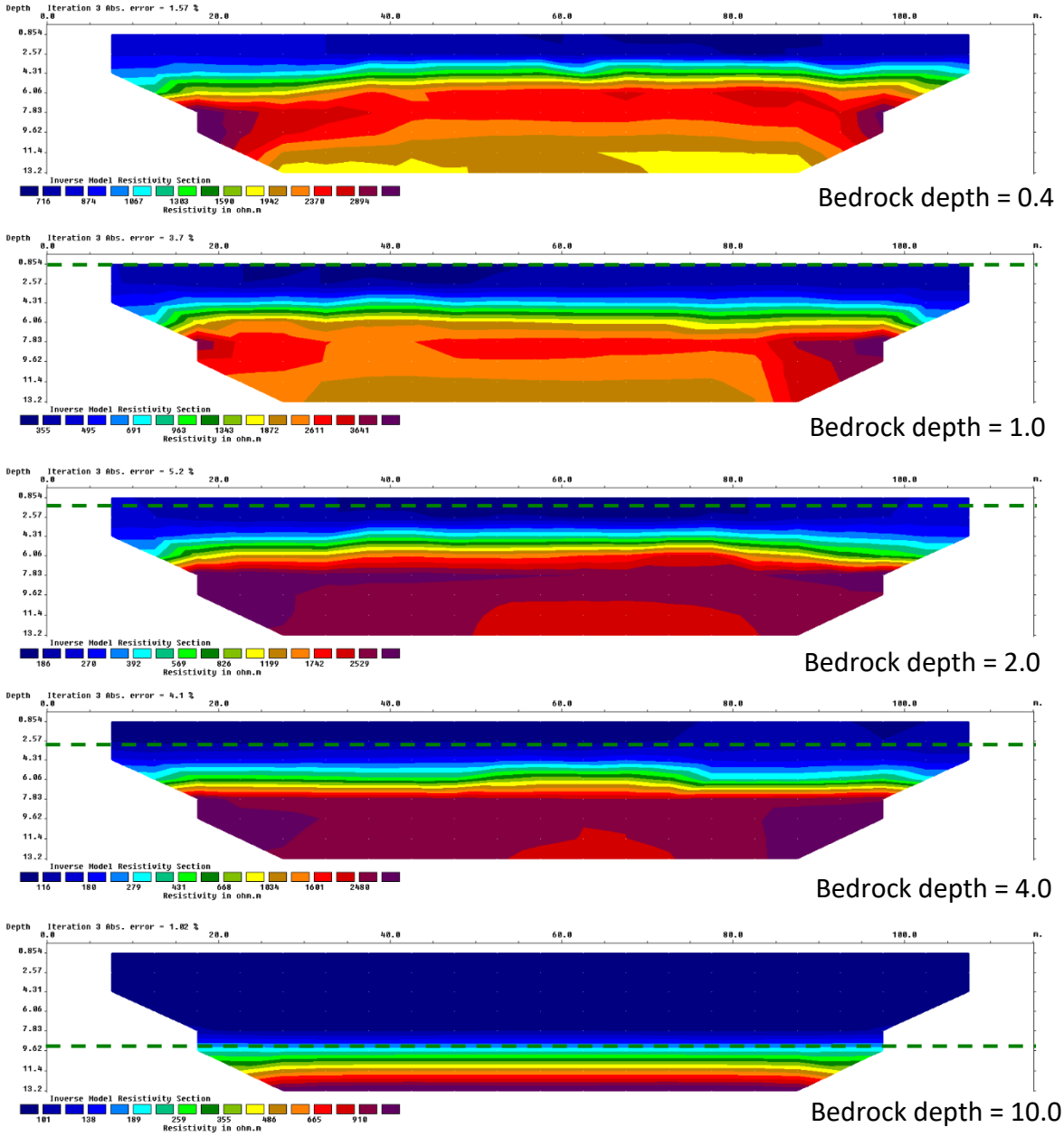

Figure B.12. RES2DINV-inverted results for 5-m dipole-dipole electrode separation modeled data with a two-layer subsurface system (100 Ωm top layer and 2000 Ωm bottom layer). The green line indicates the bedrock depth in the model (The color scale is different for each panel).

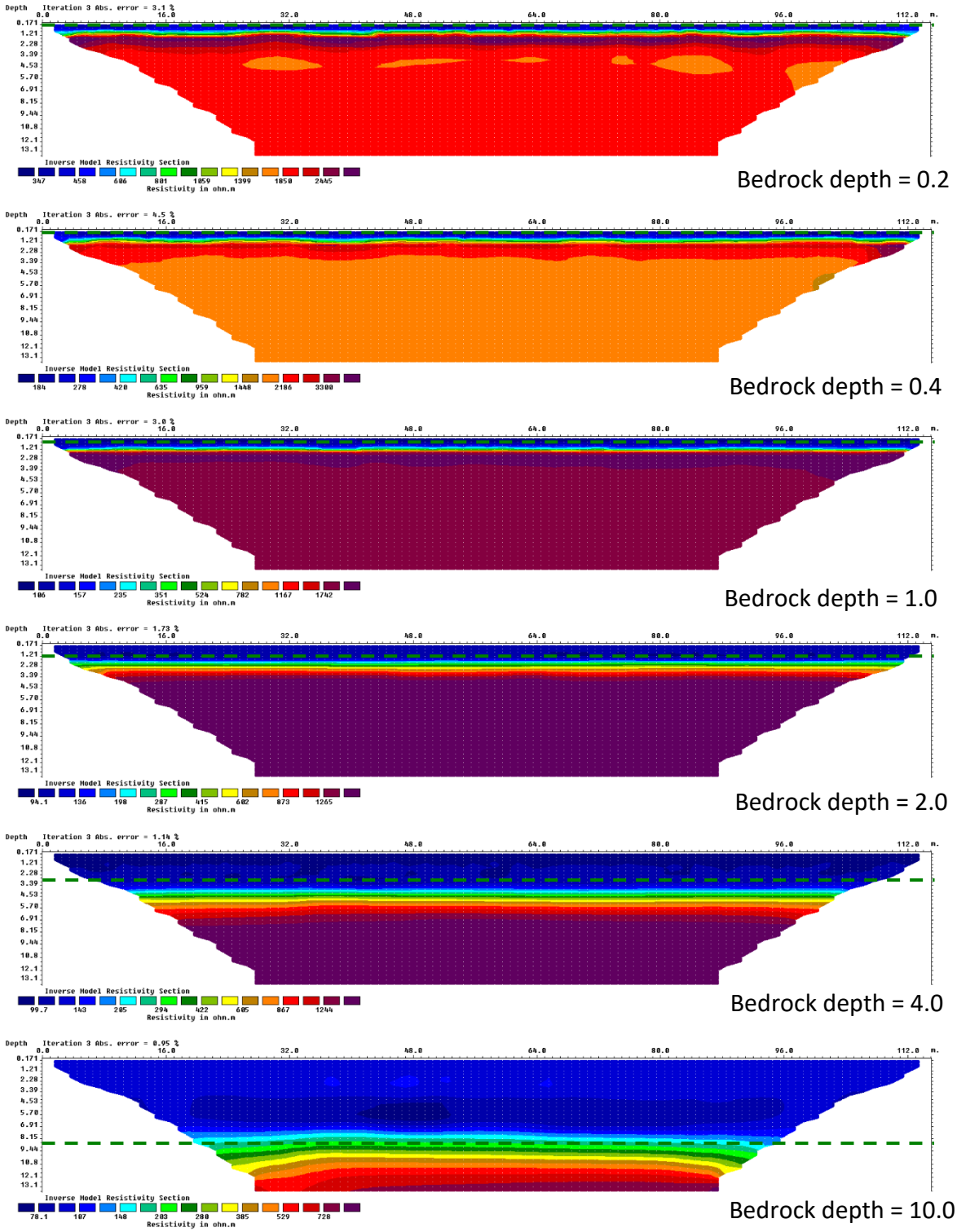

Figure B.13. RES2DINV-inverted results for combined 1-m and 5.0-dipole-dipole electrode separations modeled data with a two-layer subsurface system (100 Ωm top layers and 2000 Ωm bottom layer). The green line indicates the bedrock depth in the model (The color scale is different for each panel).

B.3.2 Electromagnetism

We used the weight function of the electromagnetic responses for vertical and horizontal dipoles available with the Geonics EM-31 instrument. This instrument has a pair of electrodes at 3.7 m separation and two coils in a plane. The orientation and elevation of the coils can be controlled by rotating the instrument 90 degrees along its axis and positioning it at different heights. In this way, they can collect four different measurements and try to solve the three unknown parameters: conductivity of the sediment layer σ1, conductivity of the bedrock σ2, and the depth of the interface.

We implemented the solution in a MATLAB script and evaluated the invertibility for the whole range of bedrock interest in N.R. 151. The used input data and the inverted depth results are presented in Figure B.14 for modeled measurement noise of 0.5%, 2.0%, and 5.0% (The conductivity values for the sediment and the bedrock were modeled at 10^{-2} S/m and 210^{-4} S/m). The inverted results show that the noisy data can reproduce the bedrock depth. To further evaluate this effect, we present the modeled depth vs. inverted depth for increasing noise level in Figure B.15. Even with a 5.0 % noise level, the inverse solution reproduces the bedrock depth well. At 20.0 %, the error becomes more significant and increases beyond 3.0 m. These results show that, at least numerically, the Geonics EM-31 instrument, measured in two orientations (i.e., vertical and horizontal dipoles) and at two different elevations (i.e., 0.2 m and 1.0 m), provide the needed information to determine the depth to bedrock bases on electrical conductivity properly.

Modeled noisy data for all interface depths	Inverted results for all interface depths
0.5 % noise in the apparent conductivity data	
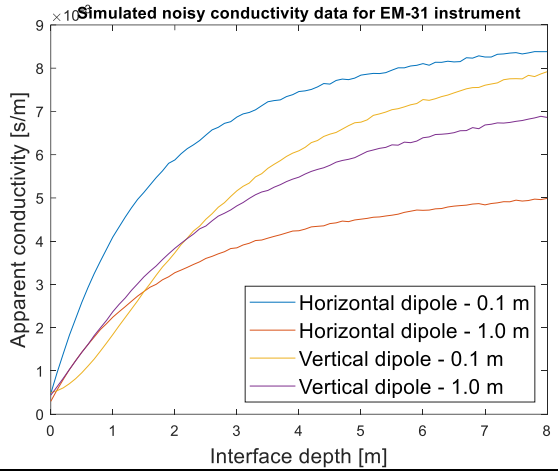	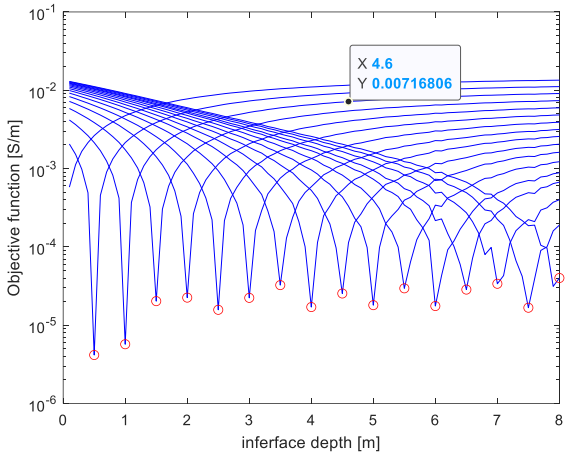
2.0 % noise in the apparent conductivity data	
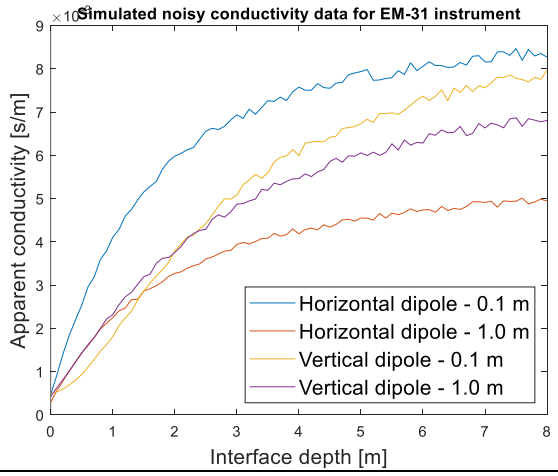	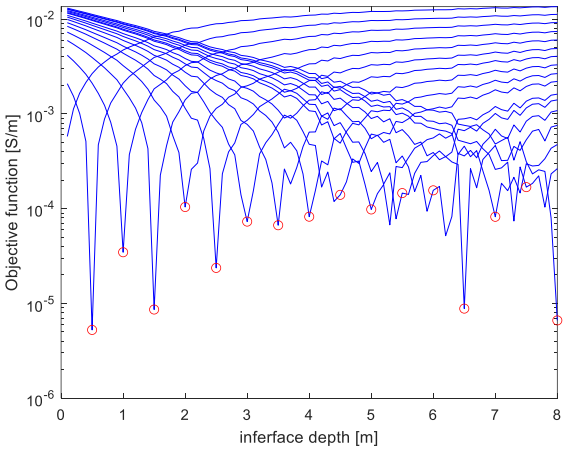
5.0 % noise in the apparent conductivity data	
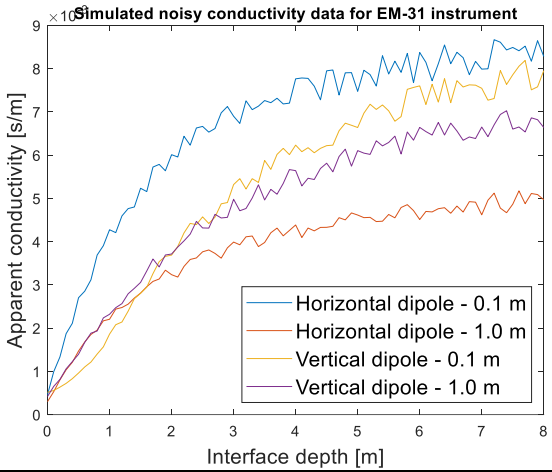	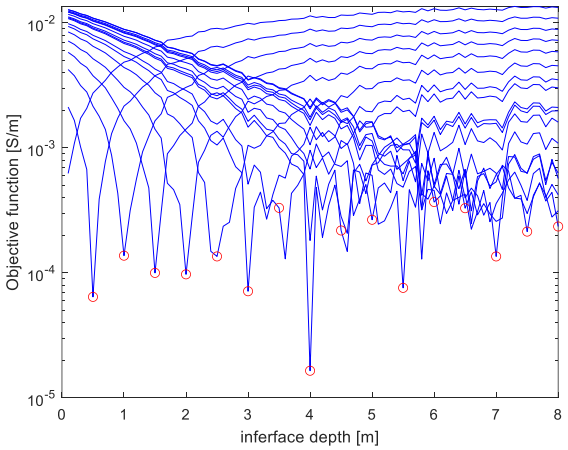

Figure B.14: Noisy apparent electrical resistivity data and inverted solution for different interface depths.

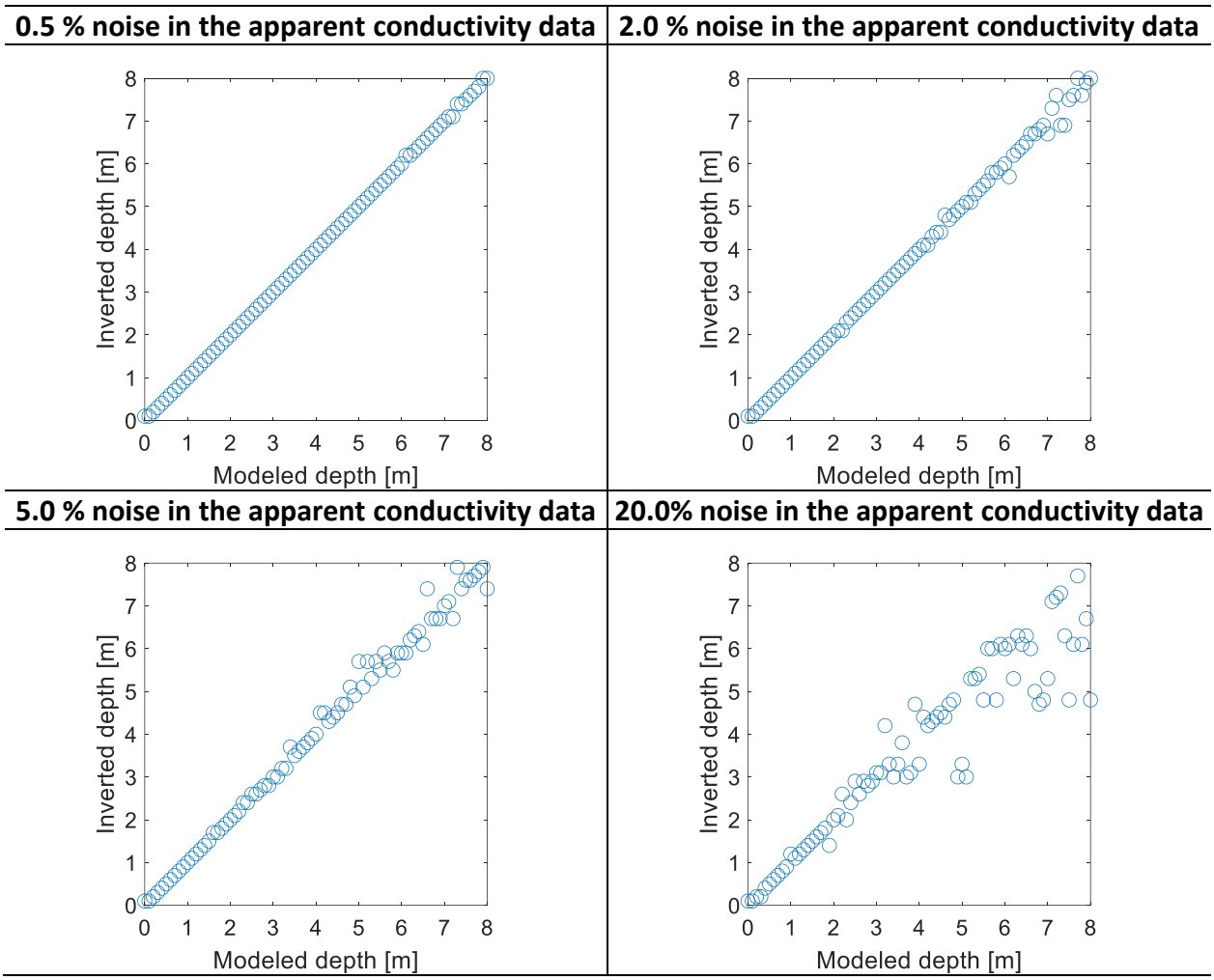

Figure B.15: Comparison of quality of the inverted data for different noise levels in the apparent electrical conductivity data.

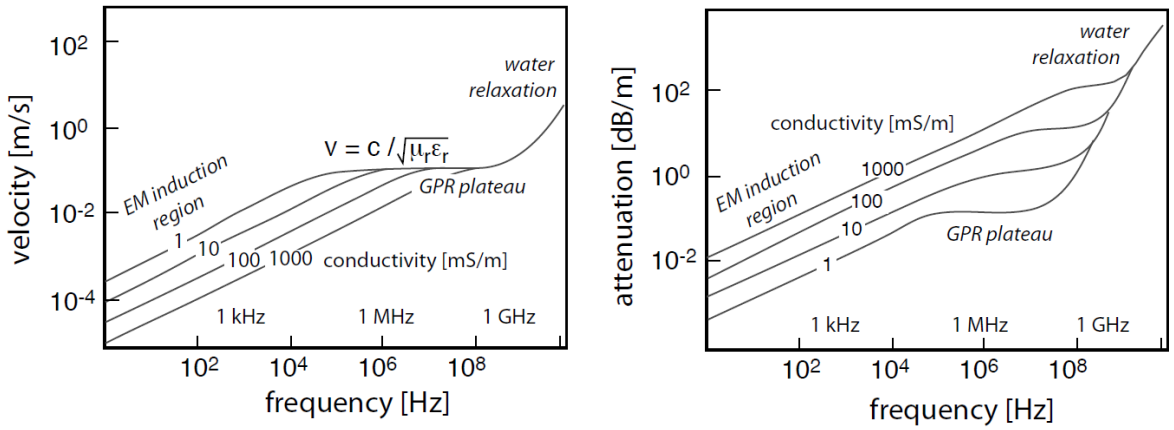

Figure B.16: Changes in EM wave velocity and attenuation with frequency and electrical conductivity (Everett 2013).

B.3.3 Ground Penetrating Radar

While GPR is a high-resolution geophysical technique that can yield fine-resolution images of the near surface, it is limited by the attenuation of electromagnetic waves in high electrical conductivity conductivities (Annan 2005). A rule of thumb indicates that the depth of penetration of GPR is:

$$d_{GPR\ Penetration}[m] = \frac{0.0035}{\sigma\left[\frac{S}{m}\right]} = 0.0035 \cdot \rho[\Omega m] \qquad \text{B.23}$$

where σ is the electrical conductivity of the host medium. This formulation assumes that the penetration depth is independent of the frequency of the GPR system. This assumption applies for low conductivity media (Figure B.16) fails as the conductivity increases:

$$d_{GPR\ Penetration} = S_d = \frac{1}{\alpha} = \frac{c_o}{2\pi f}\frac{1}{\sqrt{\frac{\varepsilon' r}{2}\left[\sqrt{1+\left(\frac{\sigma}{2\pi f \varepsilon' r \varepsilon_o}\right)^2}-1\right]}} \quad \text{EM wave attenuation} \qquad \text{B.24}$$

To model this effect, we used the conductivities within the range expected for sediments with dissolved salts expected in northwest Wisconsin to evaluate the penetration depth and the technique's potential to image bedrock depths. Results are presented in Figure B.17 conductivities from 0.0006 to 0.03 S/m (for clays and silts from for glacial sediments – data in Figure B.3) and assuming a relative dielectric permittivity ε'_r=10. Depending on the selected GPR antenna frequency and the conductivities of the sediments, the estimated depth of GPR penetration (as the inverse of attenuation) ranges from as low as 0.08 m to as high as 2 m. These results show the limitations of the GPR surveys as they fail to cover the whole range of depth considered in N.R. 151.

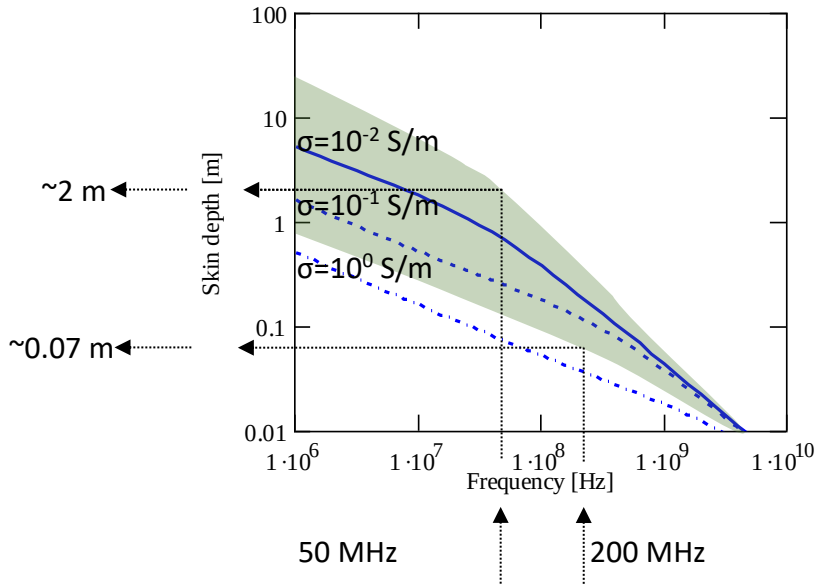

Figure B.17: Depth of penetration for different frequencies of GPR system in moderate to high conductivity environments. The shaded area corresponds to conductivities from 0.0006 to 0.03 S/m (for clays and silts from Figure B.3 for glacial sediments). Depending on the GPR antenna frequency and the sediments' conductivities, the expected penetration depth (as indicated by skin depth) would range from as low as 0.07 m to as high as 2 m.

B.4. Field Testing

We tested electrical resistivity, electromagnetic, ground penetrating radar, and seismic refraction on different areas of the state to assess the field applicability of near-surface geophysics to image the bedrock depth. We deployed these techniques in southcentral and northeast Wisconsin (Figure B.18). Those sites are in areas where carbonate rocks and Karst formation are present, including Silurian dolomites (Figure B.19). The locations include two sites, one site in Kewanee County another site in Door County, in northeast Wisconsin (Figure B.20), and three sites in southcentral Wisconsin: Dane, Columbia, and Jefferson Counties (Figure B.21). On these sites, we evaluated different topographies, depth to bedrock, and electrical conductivities of the sediment layers to be able assess the capabilities of the different techniques under different field

environments (e.g., bedrock depth and sediment conductivities). We also evaluated the time to collect data and the effort needed to reduce and interpret the results.

B.4.1 Instruments

We used four techniques and five different instruments for estimating depth to bedrock. The methods and instruments deployed included:

(a) Electrical resistivity tomography: For this research, we imaged the near surface with the IRIS Syscal Switch Kid (https://www.iris-instruments.com/syscal-kidsw.html). This is an electrical resistivity topographer with 24 electrodes and individual electrode pair separation not larger than 5 m. The cost of this type of system is about $25,000.

(b) Electromagnetic surveys: we deployed two different types of sensors:

- Geonics EM-31 (http://www.geonics.com/html/em31-mk2.html) electromagnetic sensor with 3.7-m separated coils and the ability to take measurements in vertical and horizontal dipoles. The cost of a new EM-31 instrument is about $40,000.
- Dualem-42 (https://dualem.com/products/#4) electromagnetic sensor with two pairs of vertical and perpendicular dipoles separated 1 m and 2 m apart. A new Dualem-42 instrument is about $48,000.

We collected data with the Geonics EM-31 at two different sensor elevations for each vertical and horizontal dipole to obtain four independent measurements. That means that a line needs to be walked four individual times. In contrast, the Dualem-42 instrument must pass through a line only once as it collects data using 2 and 4-m coil separation with horizontal and perpendicular dipole configurations. The data collection with the Dualem-42 is much more efficient.

(c) ground penetrating radar: we used the Sensor and Software pulseEKKO 100 system (https://www.sensoft.ca/products/pulseekkopro/overview-pulseekko/) with 50, 100, and 200 MHz antennas. A new pulseEKKO 100 is about $65,000.

(d) seismic refraction: we deployed three-component SmartSolo seismographs (https://smartsolo.com/cp-3.html). These autonomous seismographs include 5-Hz geophones, a data acquisition system, and a battery. The individual seismographs are synchronized using GPS clocks. Each SmartSolo instrument costs about $1,000 (plus the cost of a system to charge them and download the data). We use about 28 sensors in our studies.

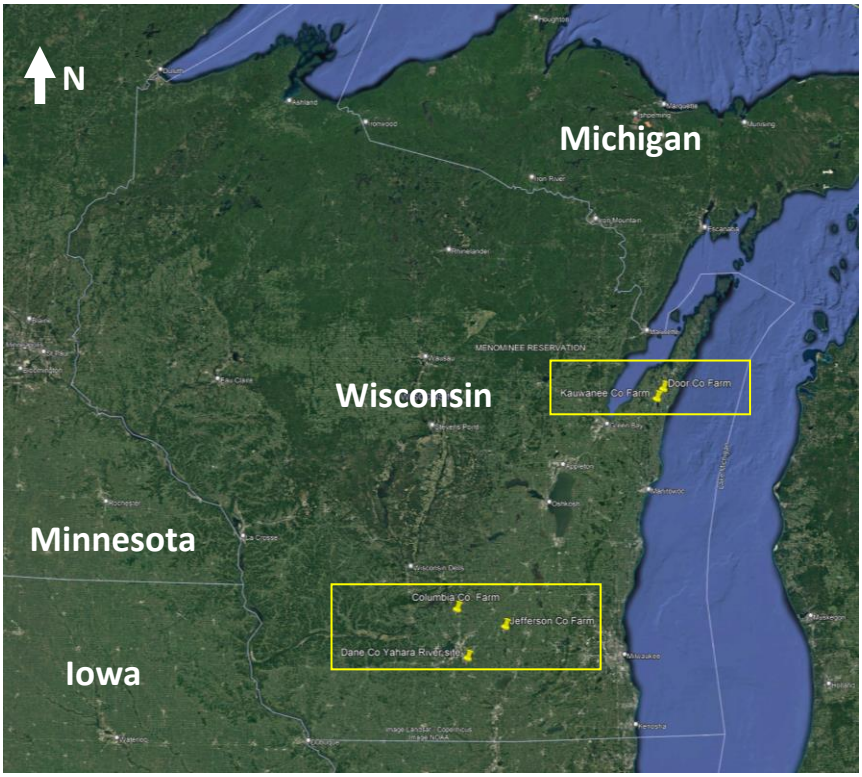

Figure B.18: Locations (in yellow pins) of the bedrock depth test sites across the northeastern and southcentral parts of Wisconsin (image source: Google Earth).

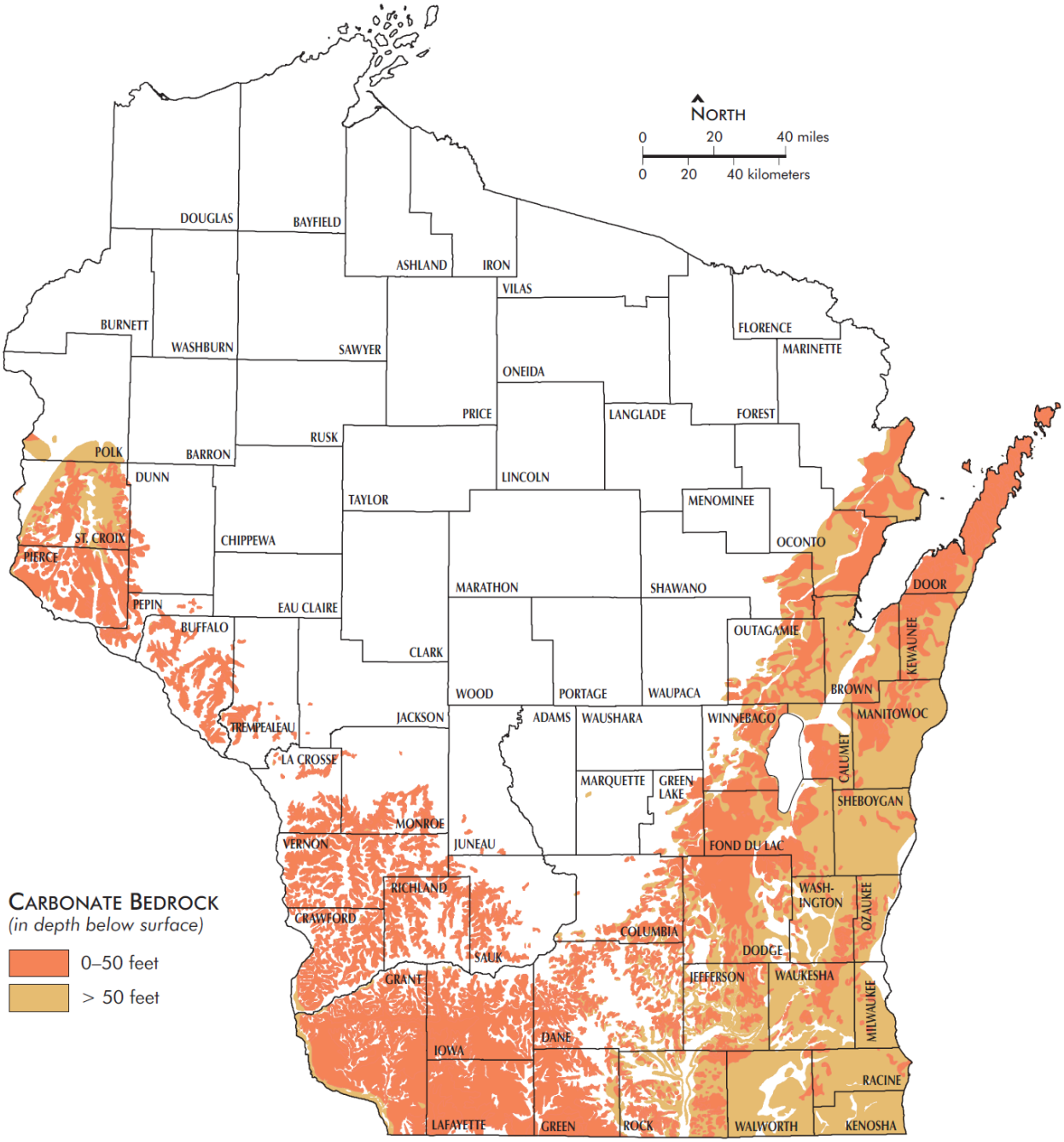

Figure B.19. Karst and shallow carbonate bedrock in Wisconsin (WGNHS 2006).

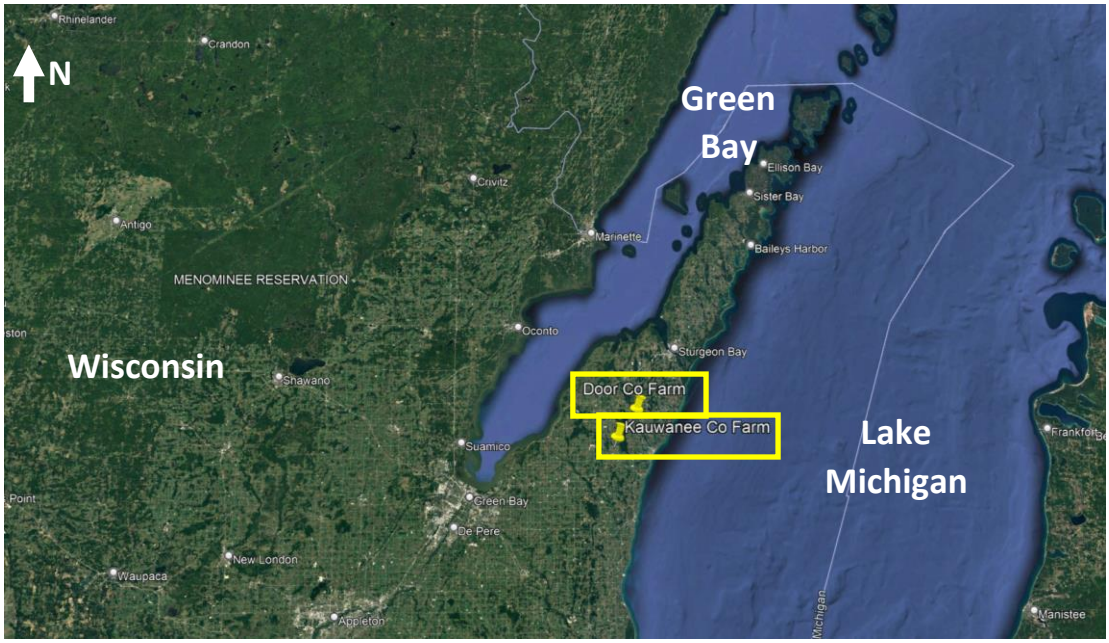

Figure B.20: Geographic locations of the field sites across Northeast Wisconsin (image source: Google Earth).

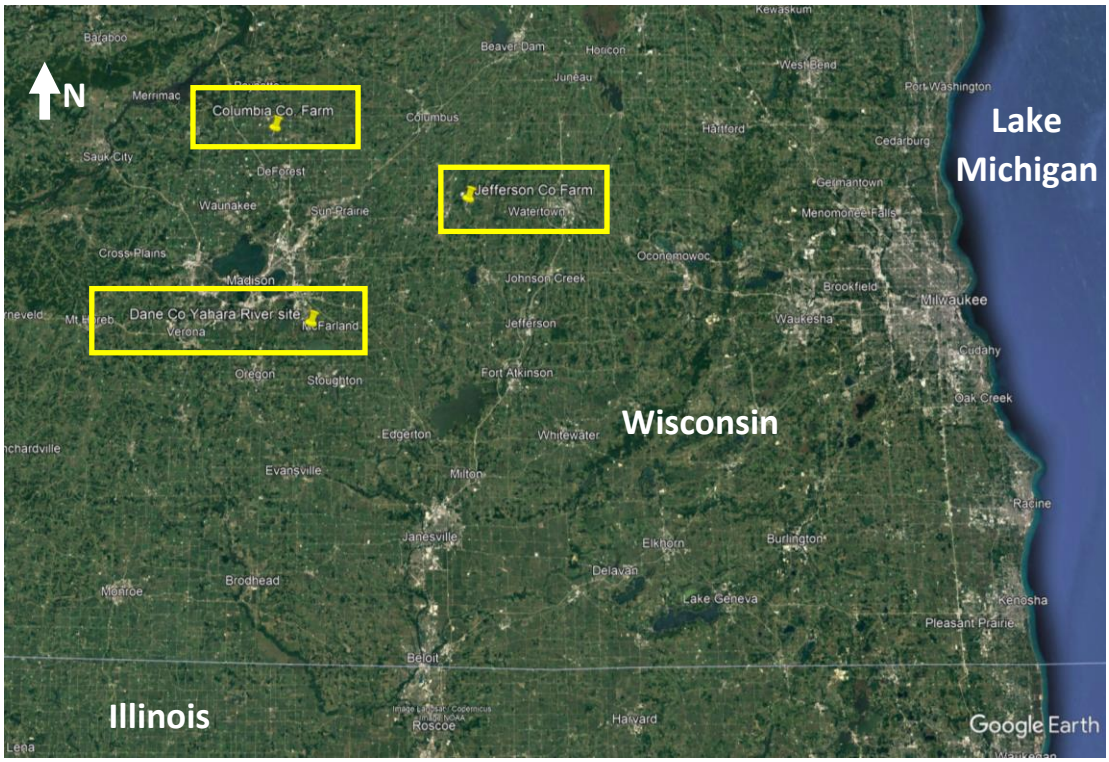

Figure B.21: Geographic locations of the field sites across Southcentral Wisconsin (image source: Google Earth).

B.4.2 Northeast Wisconsin: Kewaunee County Farm (Figure B.20)

We performed electrical resistivity imaging, electromagnetic measurements, and ground-penetrating radar surveys on a farm field in Kewaunee County. The field was surveyed, and outcrops and sinkholes were marked (Figure B.22) using a push probe survey (Figure B.23), showing the presence of bedrock close to the surface. Finally, Figure B.24 shows the surface topography along the survey line to compare the techniques.

We deployed several geophysical tools on the farm late in the Fall after the farmer had harvested the crop. At the testing we used the Iris Syscal Switch Kid electrical resistivity topographer (B.25), the Sensor and Software pulseEkko 100 MHz ground penetrating radar system (Figure B.26), the Dualem-42 electromagnetic sensor (Figure B.27), and EM-31 electromagnetic sensor (Figure B.28). Obtained results are consistent among each other and show that geophysical techniques can help in increasing the range of application of the manual push probes to beyond 0.9 m (36 in.), while being less physically demanding (Figure B.23). The comparison of the push probe data and the result from the electrical resistivity survey show that as the bedrock depth increases, the electrical resistivity decreases. This is caused by the difference between the dolomite rock's high electrical resistivity and the surface sediments' low resistivity.

The GPR pulseEKKO, the Dualem-42, and Geonics EM-31 surveys confirm the observations. The GPR survey (Figure B.26) captures the presence of shallow bedrock but loses its presence as the depth of bedrock increases. The situation is caused by two combined situations: the increase in electrical conductivity that decreases the depth of electromagnetic penetration and the increase in the depth of the bedrock. In our electrical resistivity results, the resistivity decreases from a

high of about 500 Ωm on the west of the survey to about 100 Ωm to the center and East of the survey line (Figure B.25). These values yield the rule-of-thumb depth of GPR signal penetration (Eq. B.23) as low as 0.35 m and as high as 1.75 m explaining in broad terms the limitation of the GPR technique in imaging the depth to bedrock across the survey line.

Figure B.22: Location of exposed bedrock and sinkholes at the surveyed Kewanee County farm in Northeast Wisconsin (modified after Hart et al. 2020).

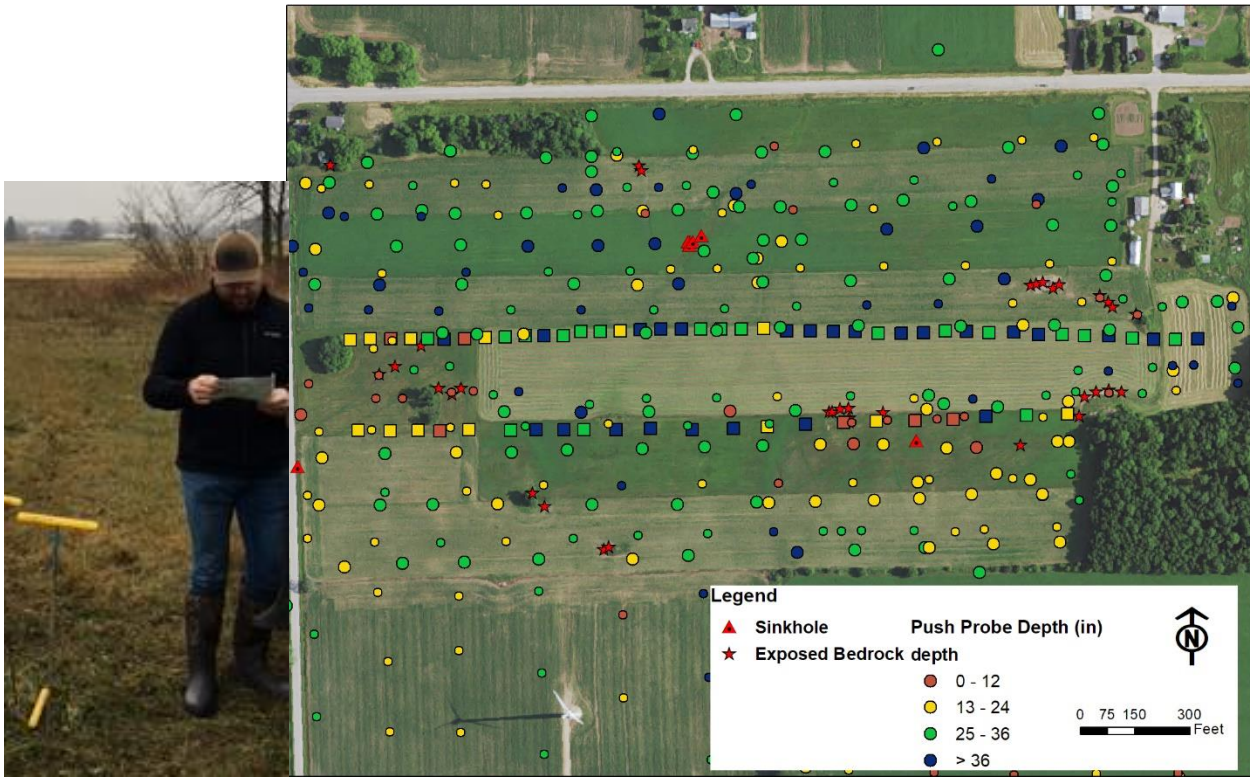

Figure B.23: Push probes and the summary of the manual push probe survey data collected at the Kewaunee County farm (pictures and data from Hart et al. 2020).

Similarly, the results from the Dualem-42 (Figure B.27) and Geonics EM-31 (Figure B.28) surveys show an increase in apparent electrical conductivity from West to East across the farmland, as both the depth to bedrock increase and the electrical conductivity of the sediments increases. Please note that the measurements presented in Figures B.27 and B.28 were collected with different instruments at different configurations, so the values the sensors yielded are not necessarily the same. However, both datasets show an increase in electrical conductivity from West to East. Please also note that the Dualem-42 instrument was mounted on a trailer behind an all-terrain vehicle to reduce the interference.

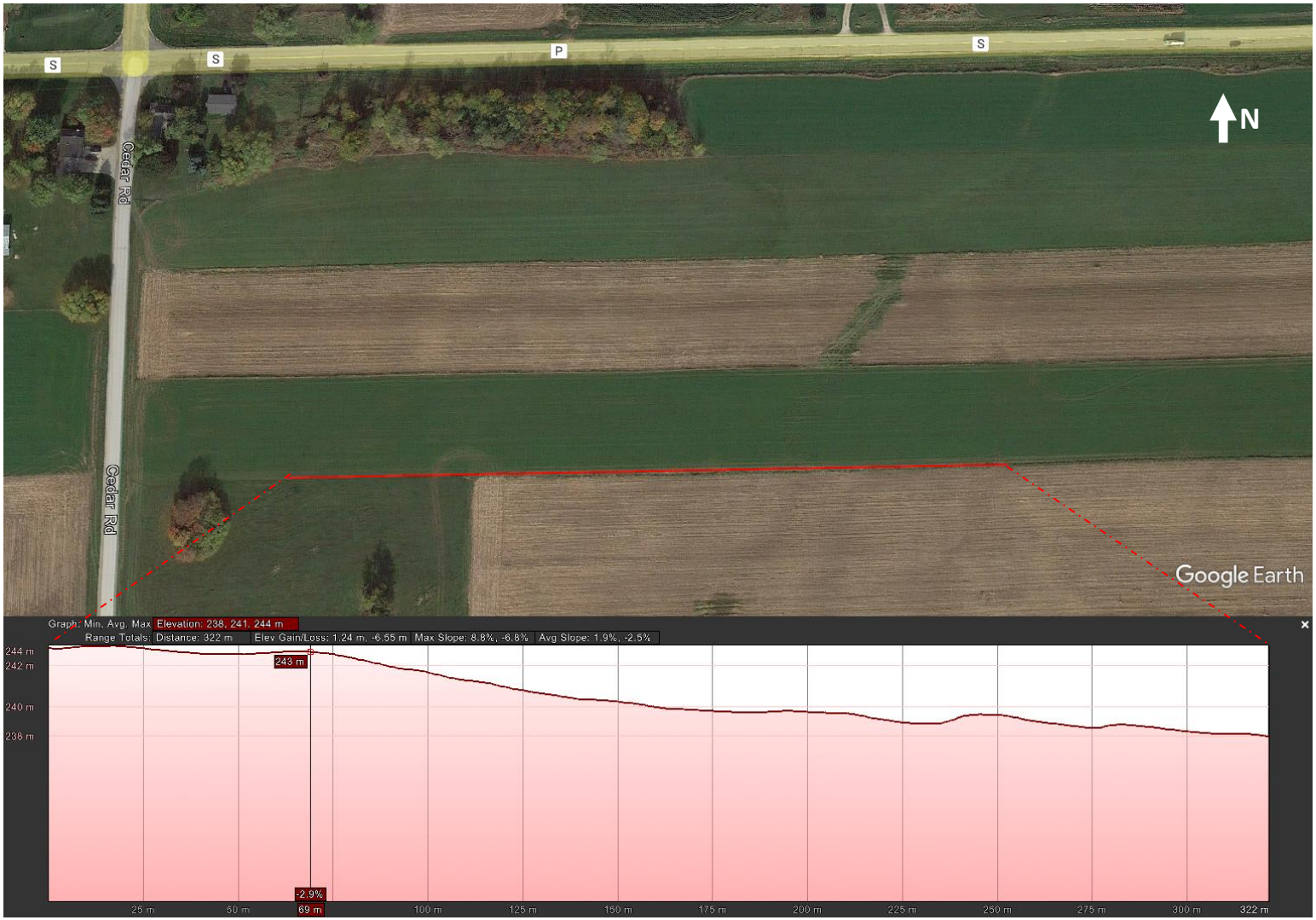

Figure B.24: Surface topography along the evaluated survey line (Source: Google Earth).

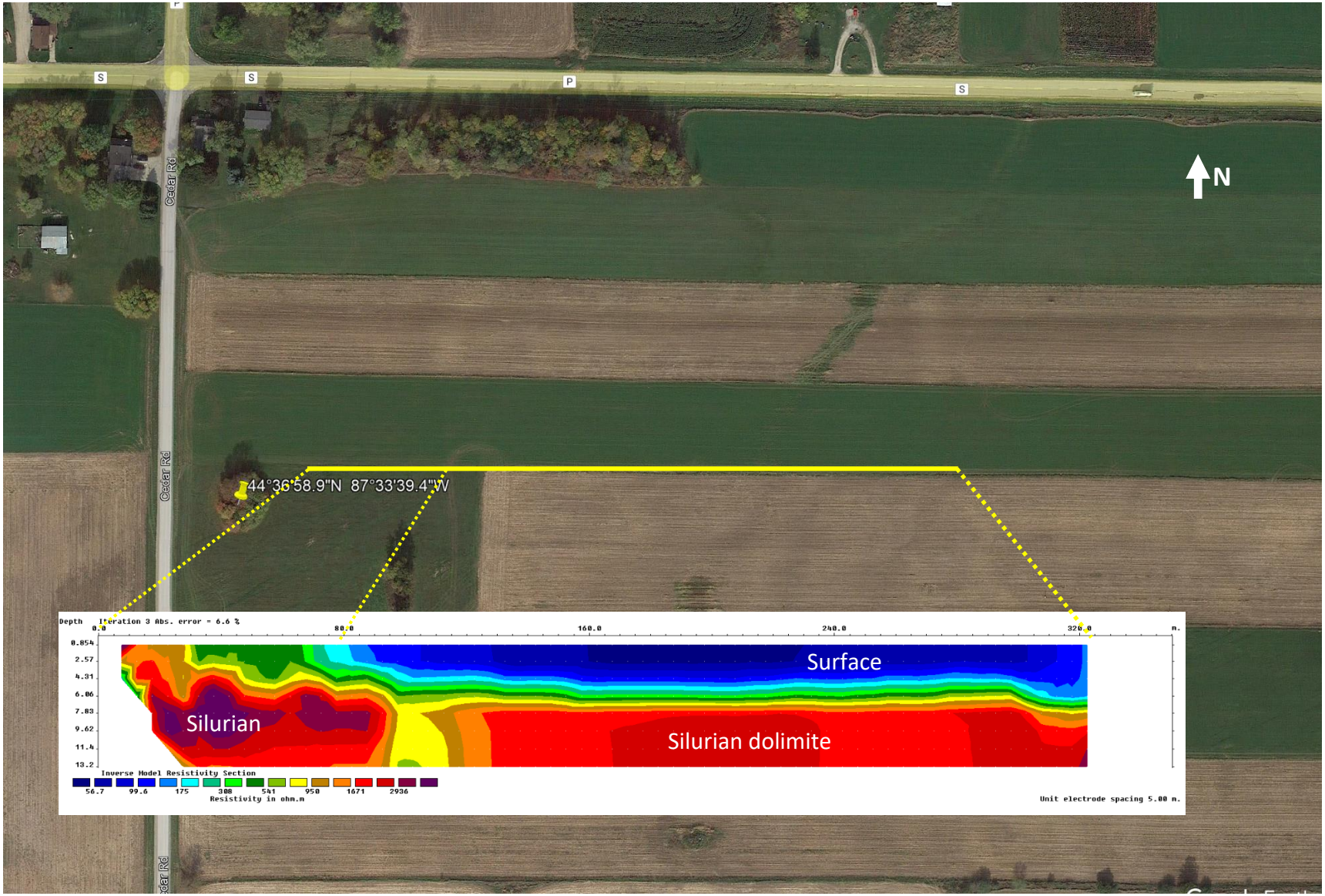

Figure B.25. Electrical resistivity tomography line parallel to the GPR survey line along the Kewaunee County farm.

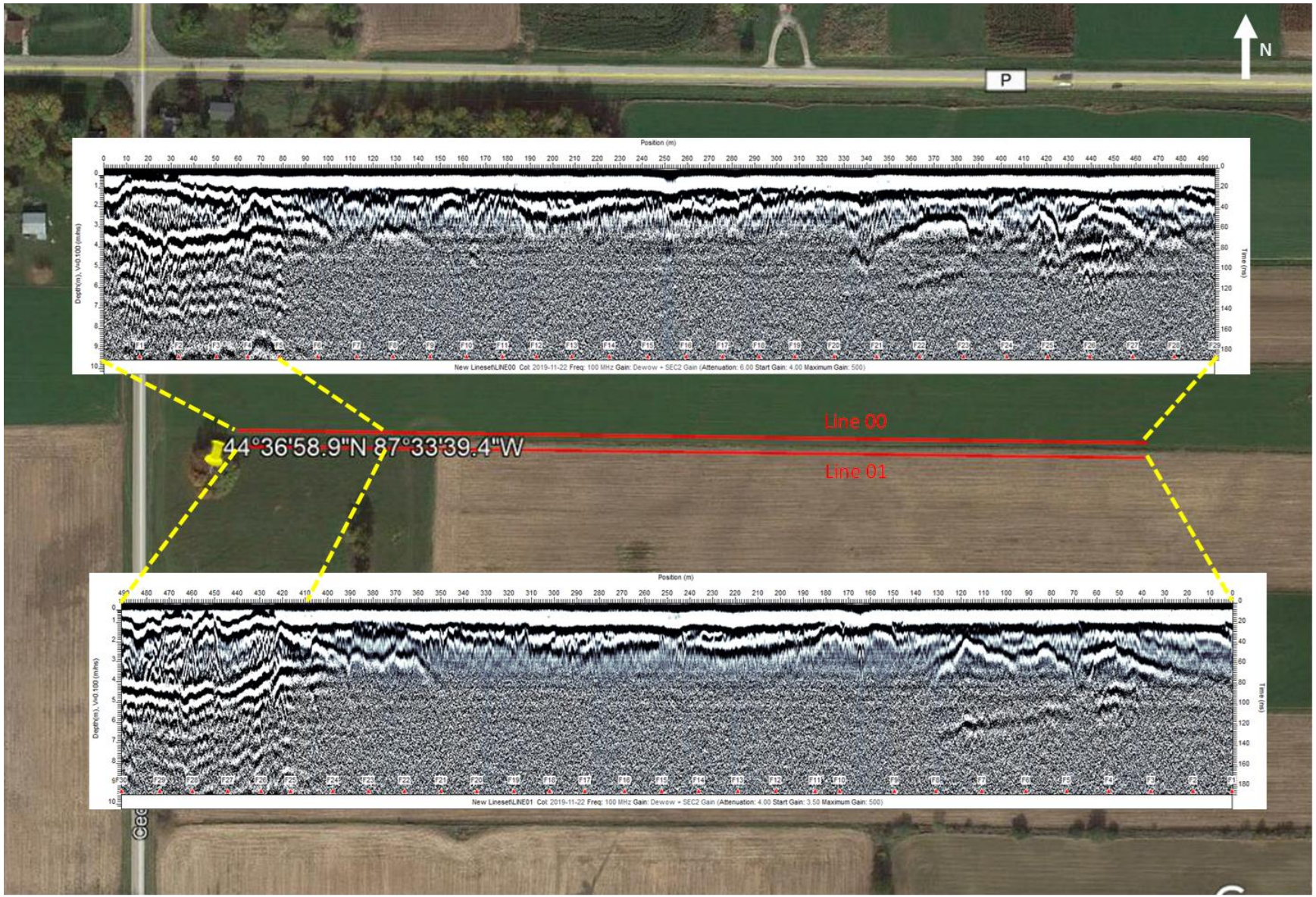

Figure B.26. GPR Lines using 100 MHz Antennae along a Kewaunee County Farm (Approximated locations).

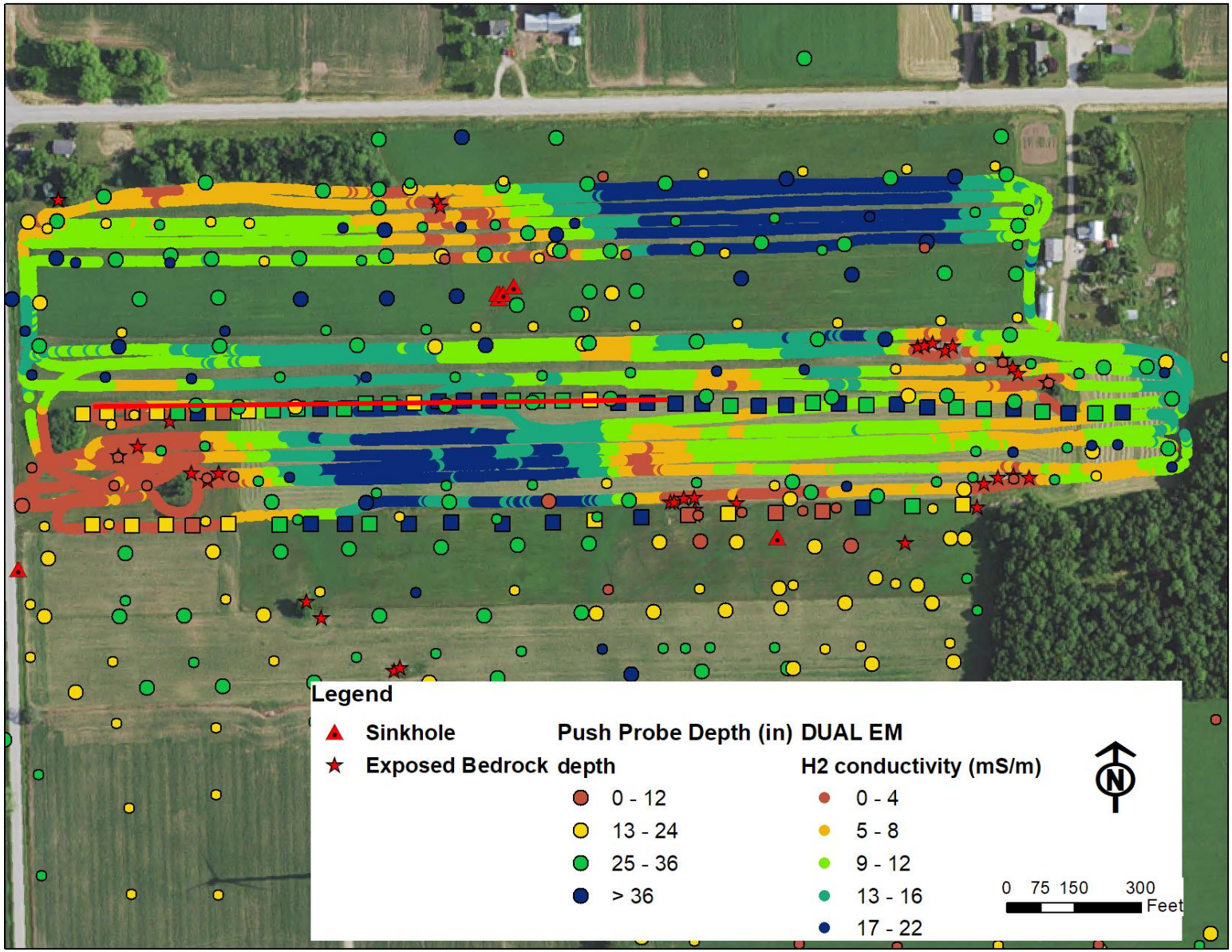

Figure B.27: Depth (in inches) using a push probe vs. the apparent electrical conductivity using the 2-m Dualem-42 instrument (data from Hart et al. 2020). The red line presented the approximate line of reference for all the surveys.

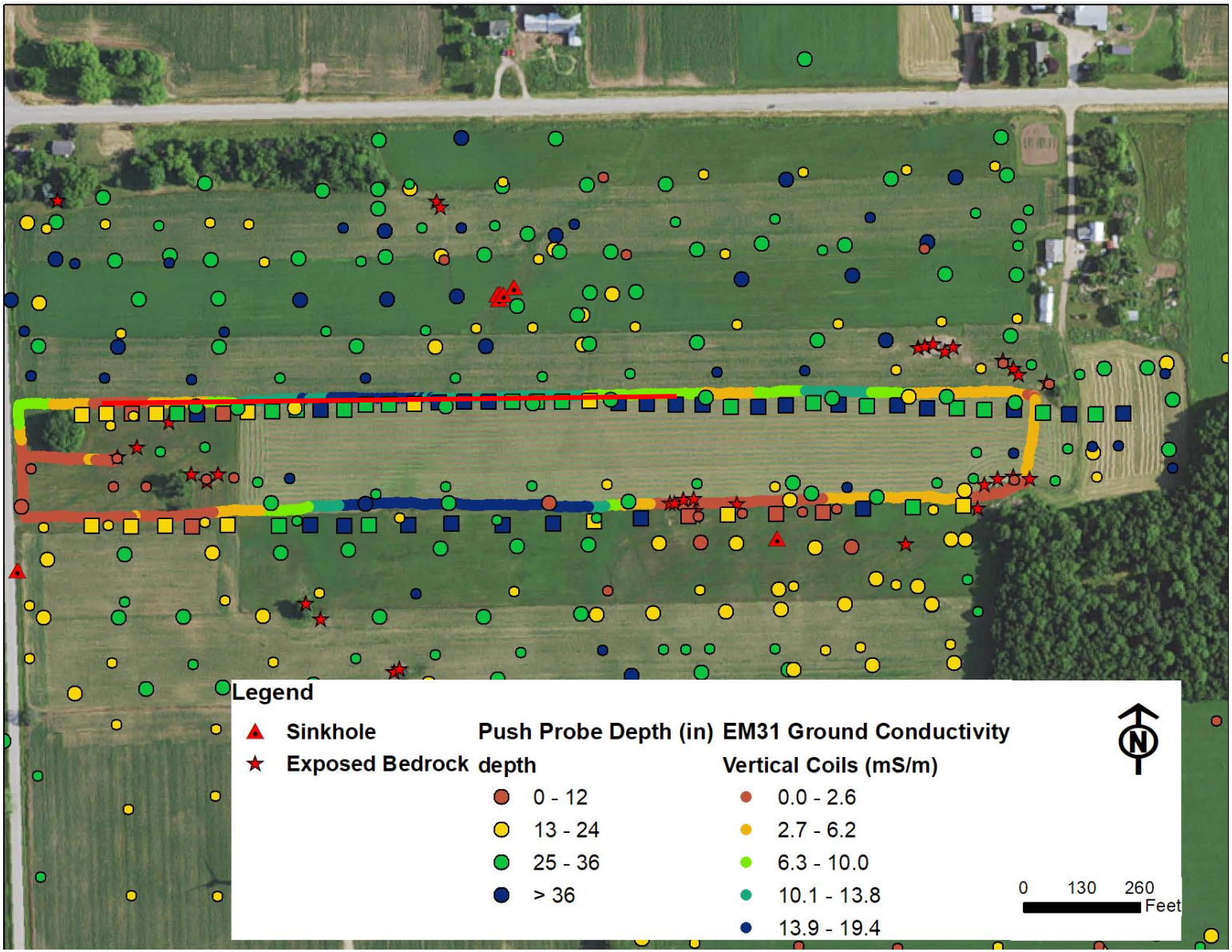

Figure B.28: Depth (in inches) using a push probe vs. the apparent electrical conductivity using the 3.7-m Geonic EM-31 instrument (data Hart et al. 2020). The red line presented the approximate line of reference for all the surveys.

B.4.3 Northeast Wisconsin: Door County Farm (Figure B.20)

Using an all-terrain vehicle (ATV) allows for the rapid collection of data in large areas (e.g., the typical 40-acre farms in Wisconsin). However, the problem with using an ATV is that the ferromagnetic material used in the frame and engine of the vehicle might mask or interfere with the response of the electromagnetic sensor, preventing the proper inversion of the measurements (Mitsuhata et al., 2022). This problem might be solved by pulling the electromagnet instrument by hand or by developing an array pulled by an ATV at a certain distance from the instrument.

To test this issue, we ran electromagnetic surveys using the Dualem-42 instrument on a fallow field in South Door County, WI (Figure B.29). We ran two different surveys. First, the Dualem-42 instrument was mounted on the back of an all-terrain vehicle (ATV - at a height of ~1.0 m), and second, on top of a sled (at a height of ~0.15 m) that was pulled by an operator walking across the field. It took about 35 minutes to collect the dataset with the instrument mounted on the ATV, as the measurements in all four configurations were collected simultaneously. The Dualem-42 survey is done by hand on top of a sled, allowing the collection of data to be inverted, but the process is much slower (it took about 20 minutes for a much smaller covered area). Figures B.30 and B.31 presented the results collected at the site. Figure B.30 presents the data located with GPS coordinates, while Figure B.31 presents the data as a function of the measurement sequence. Two things can be inferred from the data: (1) the presence of the instrument on the ATV completely masked the measurements (Figures B.30a and B.31), and (2) the vertical dipoles at 1 m separation for the sensor dragged on the sled is out of calibration: the data series are correlated, but the electrical conductivity results are negative for the 1-m separated vertical

dipoles (Figure B.31). Still the other three traces provide clues of the bedrock distribution under the farm. Two main sections are identified: measurements 75 to 500 (Segment 1), the electrical conductivity decreases with depth (i.e., the depth sensitivity decreases from the 2-m vertical dipole separation, 2-m perpendicular dipole, to 1 m perpendicular dipole as shown in Figure B.5a), indicating the presence of bedrock near the surface. Measurements 600 to 900 (Segment 2), the electrical conductivity increased with depth, possibly indicating the presence of the water table close to the surface.

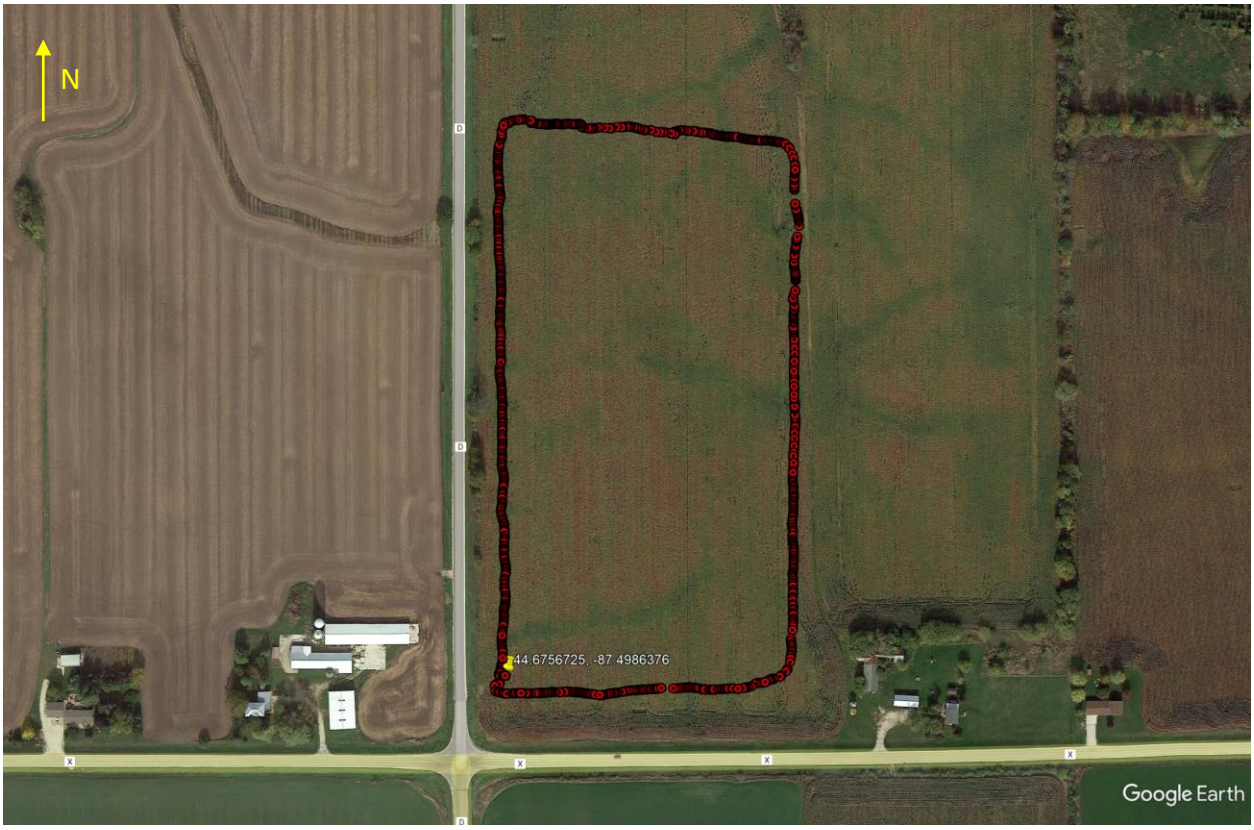

Figure B.29: Location of the electromagnetic survey in Door County, WI. The presented data corresponds to the survey collected with the dualEM-42 instrument pulled with a sled (Image: Google Earth).

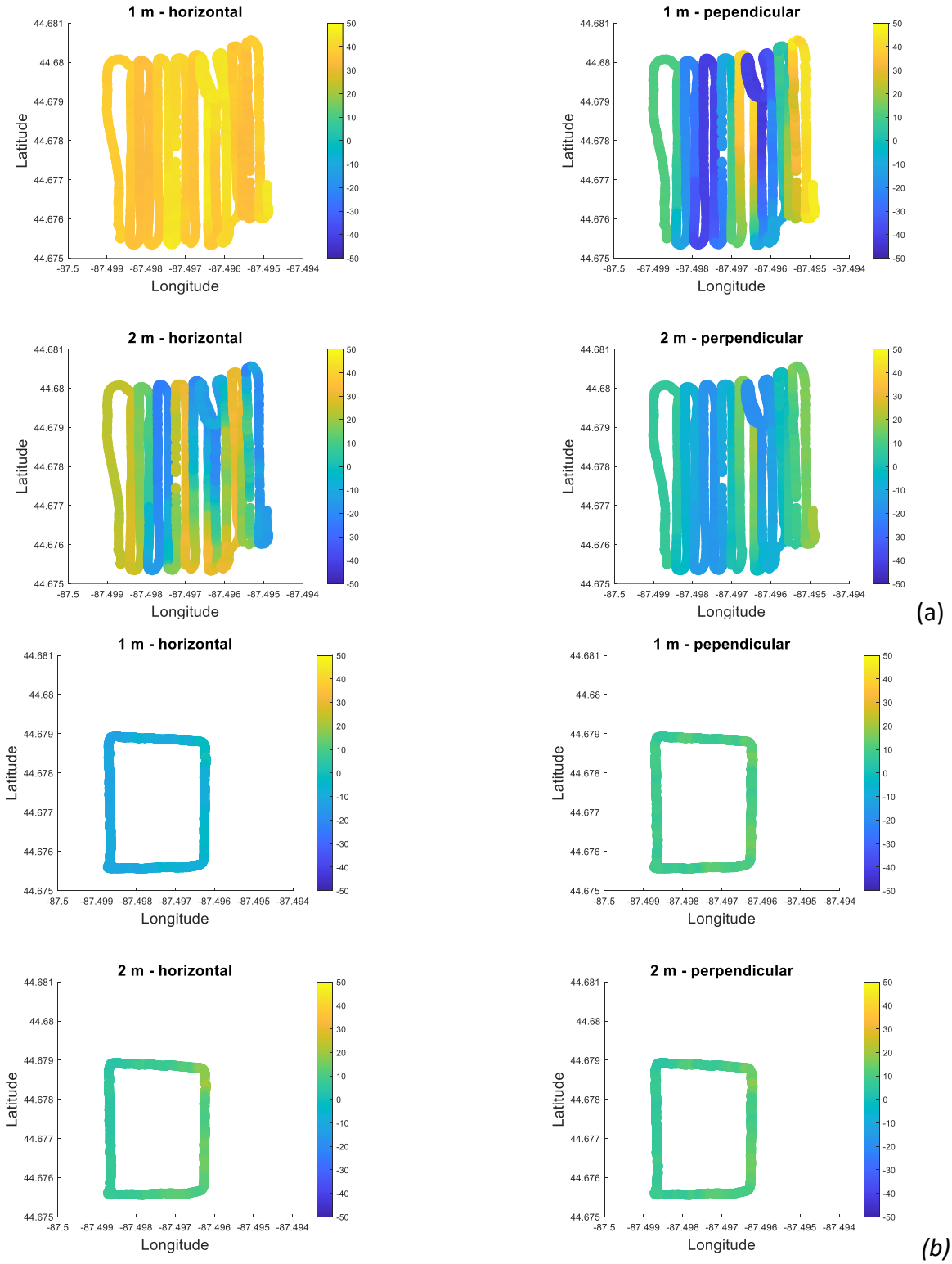

Figure B.30: Summary of the electromagnetic data collected from the Door County farm: (a) electrical conductivity for the Dualem-42 mounted on the back of an ATV about 1 m about the surface, (b) electrical conductivity for the Dualem-42 electromagnetics dragged on a sled just above the ground surface.

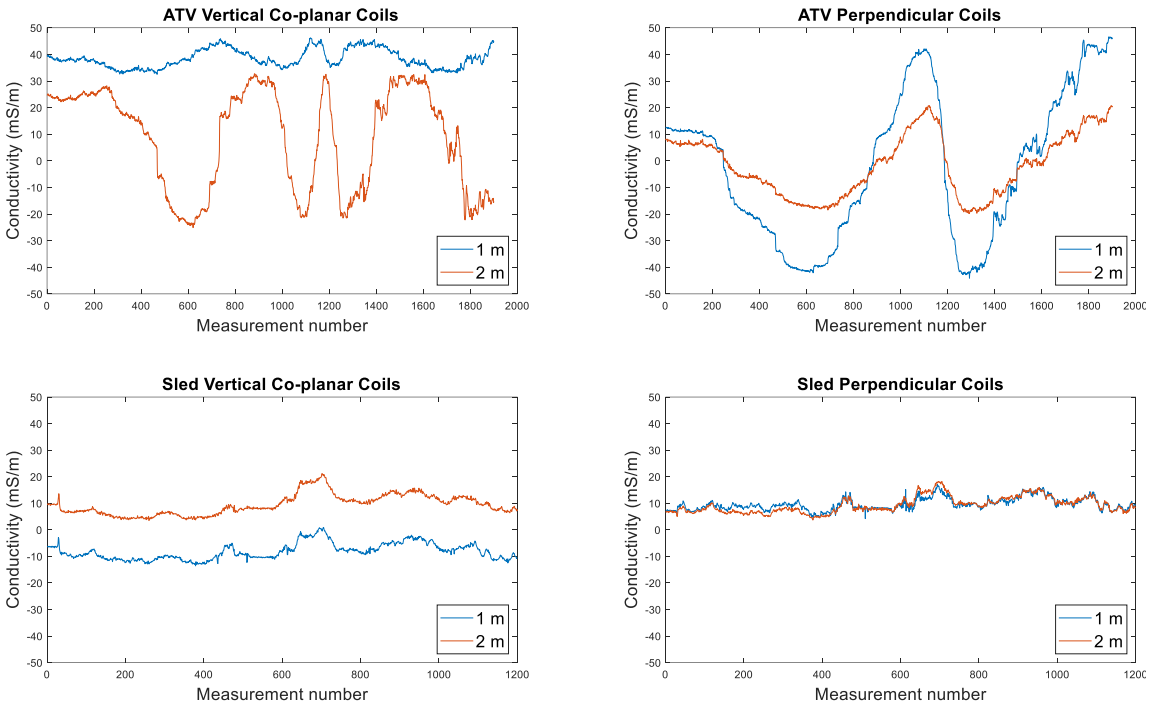

Figure B.31: Summary of the electromagnetic data collected from the Door County farm for the Dualem-42 mounted on the back of an ATV about 1 m about the surface, for the Dualem-42 electromagnetics dragged on a sled just above the ground surface.

Plotting all three remaining data series shows two segments where the magnitude of the configuration measurements flipped. We refer to these measurement sections as Segment 1 and Segment 2 (Figures B.32 and B.33). The two segments show a strong correlation between the 2-m vertical dipole apparent conductivity measurements and the surface elevation at the farm (Figure B.34a); however, the apparent conductivity gather with the 1-m perpendicular dipole is relatively constant (Figure B.32 and B.34b) as this configuration senses the shallow subsurface. One possible explanation for the Segment 1 results is that the higher elevation keeps the water table below the sensitive range of the configuration. As the elevation decreases, the water table gets closer to the sensor, and the apparent electrical conductivity increases. For this dataset, the electromagnetic sensor did not appear to sense the presence of the bedrock.

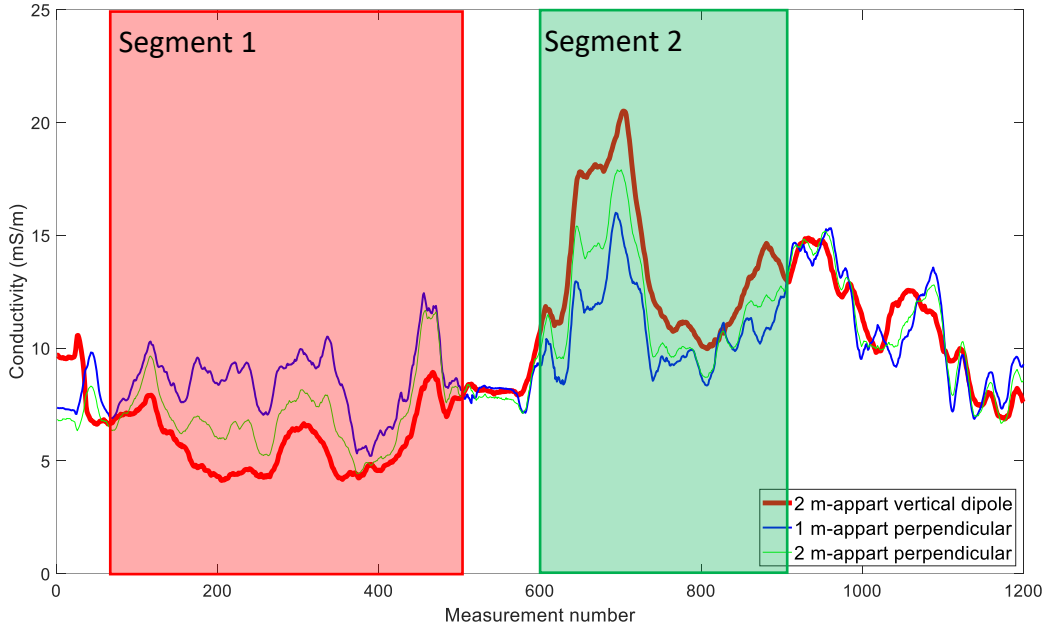

Figure B.32: Moving averaged data collected with Dualem-42 electromagnetics walked across the field.

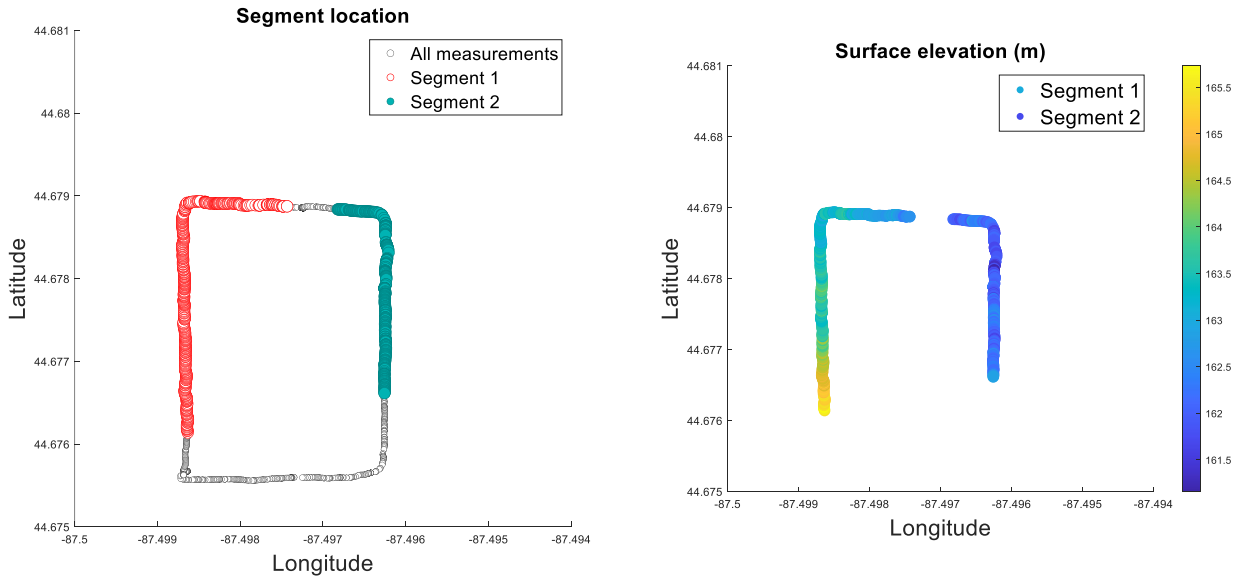

Figure B.33: Location and elevation of the segments.

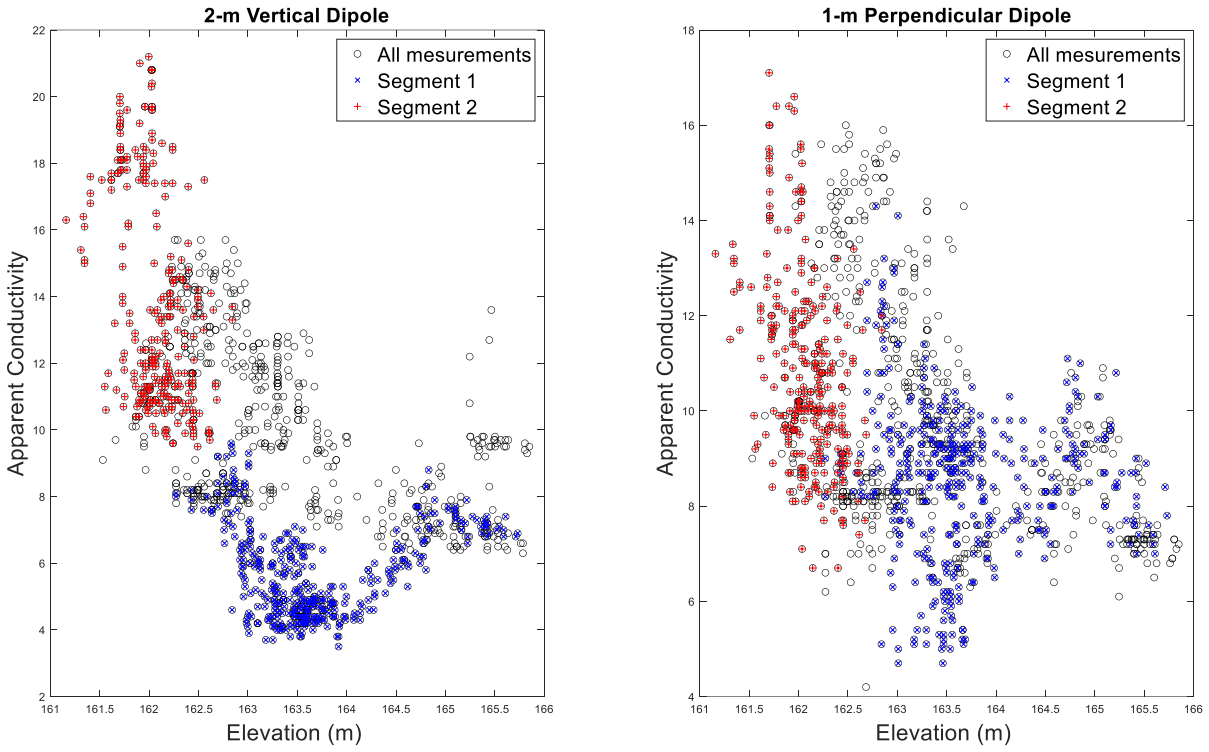

(a) (b)

Figure B.34: Effect of surface topography on the apparent conductivity measurements. (2) 2-m vertical dipole, and (b) 1-m perpendicular dipole.

B.4.4 Southcentral Wisconsin: Columbia County Farm (Figure B.21)

We collected GPR, electrical resistivity, and electromagnetic survey data across an experimental farm field belonging to UW-Madison's Arlington Experimental Station just East of the town of Leeds in Columbia County, WI (Figure B.35). We selected this site because it is located next to a rock quarry that leaves exposed to a change in the sediment thickness (Figure B.36), providing an opportunity to ground truth the geophysical results. The tested site was an experimental cornfield, and the top sediment was silty clay.

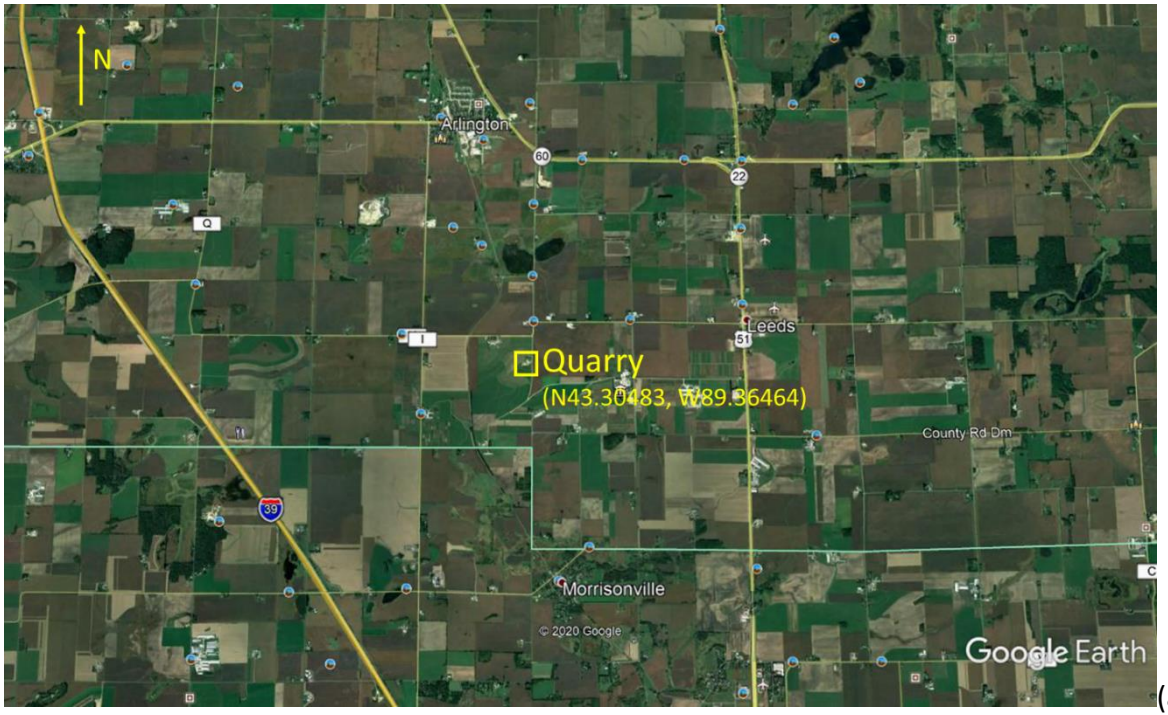

(a)

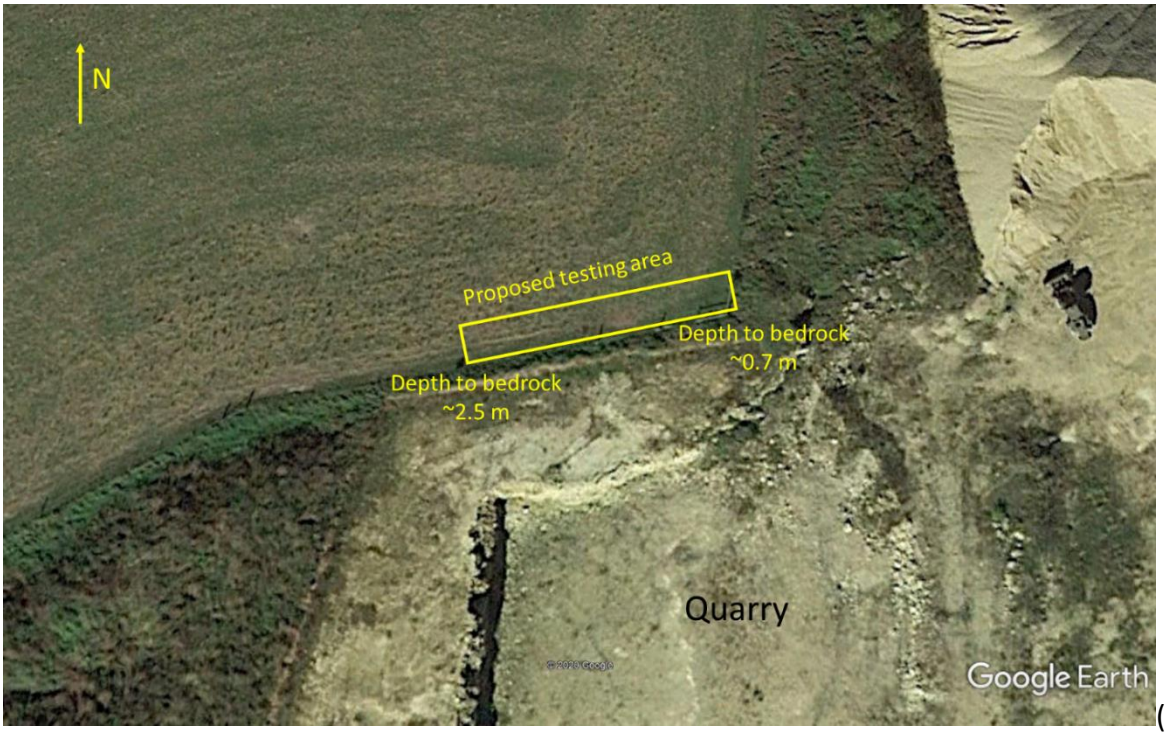

(b)

Figure B.35: (a) Location of UW-Madison's Arlington Experimental Station and (b) the location of the quarry where the survey took place (Images: Google Earth).

West East

(a)

(b)

Figure B.36: Image of the South face of the testing (a) East end of the tested area (depth to bedrock ~0.4 m), and (b) West end of the tested (depth to bedrock ~1.8 m). The sediment depth increases from east to west. Ms. Katherine Swager served as the scale for the photographs.

Figure B.37 shows the location and the summary process results of the 200 MHz GPR antenna results. The results were unsuccessful as there was high electrical conductivity in the soil at the site. Line 02 from East to West (Figure B.37) captures bedrock reflection between 1.0 m and 1.5

m. While imaging depth to bedrock using GPR is a simple, rapid technique, the quality of the images is highly dependent on the electrical conductivity of the surface soils. For reference, it took about 15 minutes to collect the GPR data after the instrument was assembled.

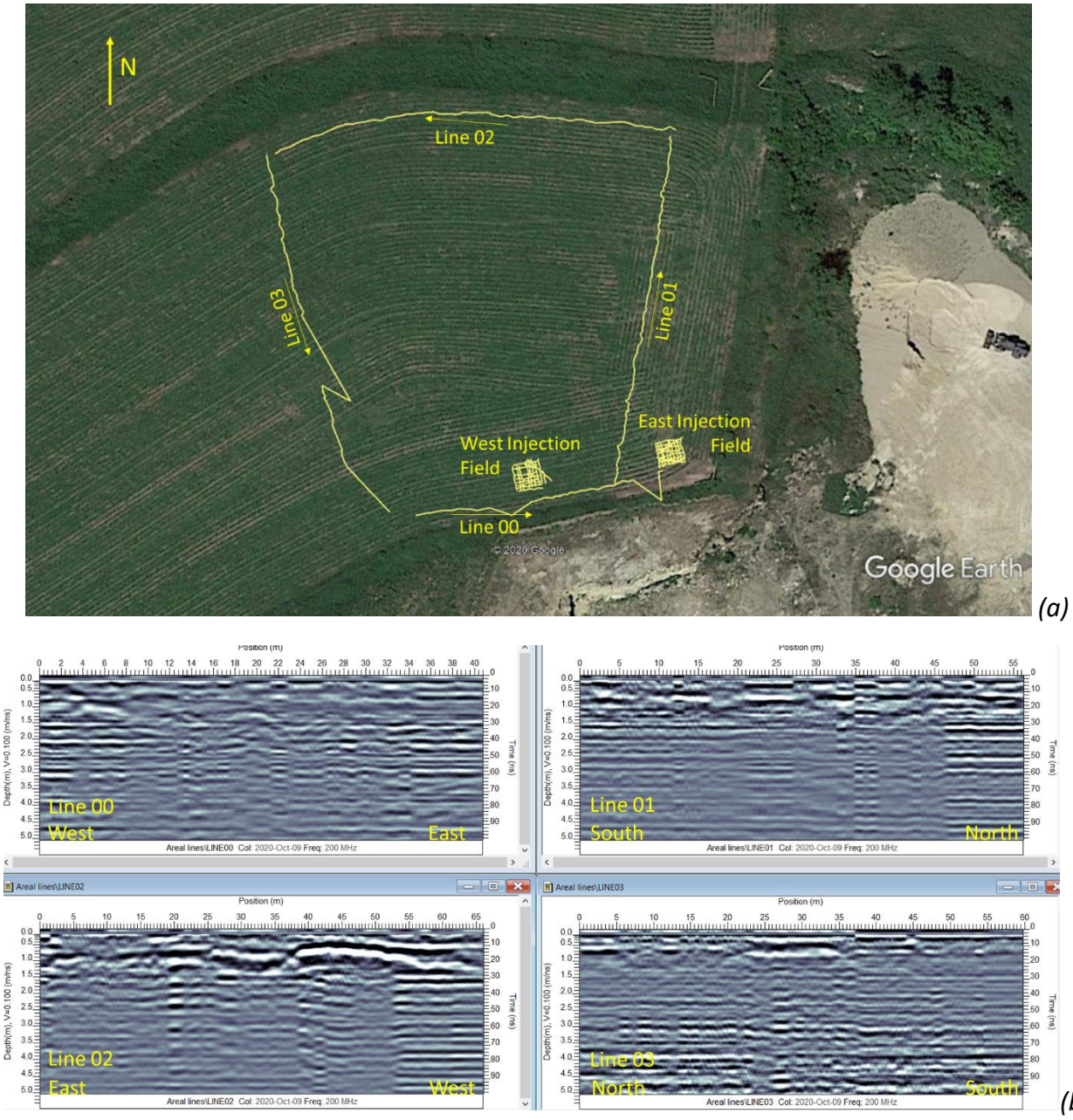

Figure B.37: (a) Location (Image: Google Earth) and (b) summary of the GPR survey and results across the experimental corn field in the Arlington Experimental Station.

In the same testing area, we collected electrical resistivity data in a dipole-dipole configuration, and we interpreted the data obtained from tomographic images (Figure 3.38). We deployed the survey along a line close to the one presented in line 00 of Figure B.38a. The 60-electrode survey line (electrode separation of 1.0 m) took about four hours to collect.

The data and inverted results are presented in Figure B.38b. Assuming a transition between sediment/bedrock at about 800 Ωm; the bedrock depth decreases from 1.5 m at the east to about 0.8 m West. These results contradict the data presented in the photographs in Figure B.36, which shows an increase in bedrock depth from East to West. It is important to emphasize that not only does the surface show topographic changes (Figure B.38a), but the bedrock surface also has topography.

We also collected electromagnetic data at the site using the Geometrics EM-31 instrument. Figure B.39 shows the location of the survey path. We collected data at two different sensor elevations and at different orientations to be able to solve the bedrock depth. As described in the electromagnetism section and compiled in Figure B.5, the sensitivity of the electromagnetic measurements depends on the dipole direction and the sensor's height.

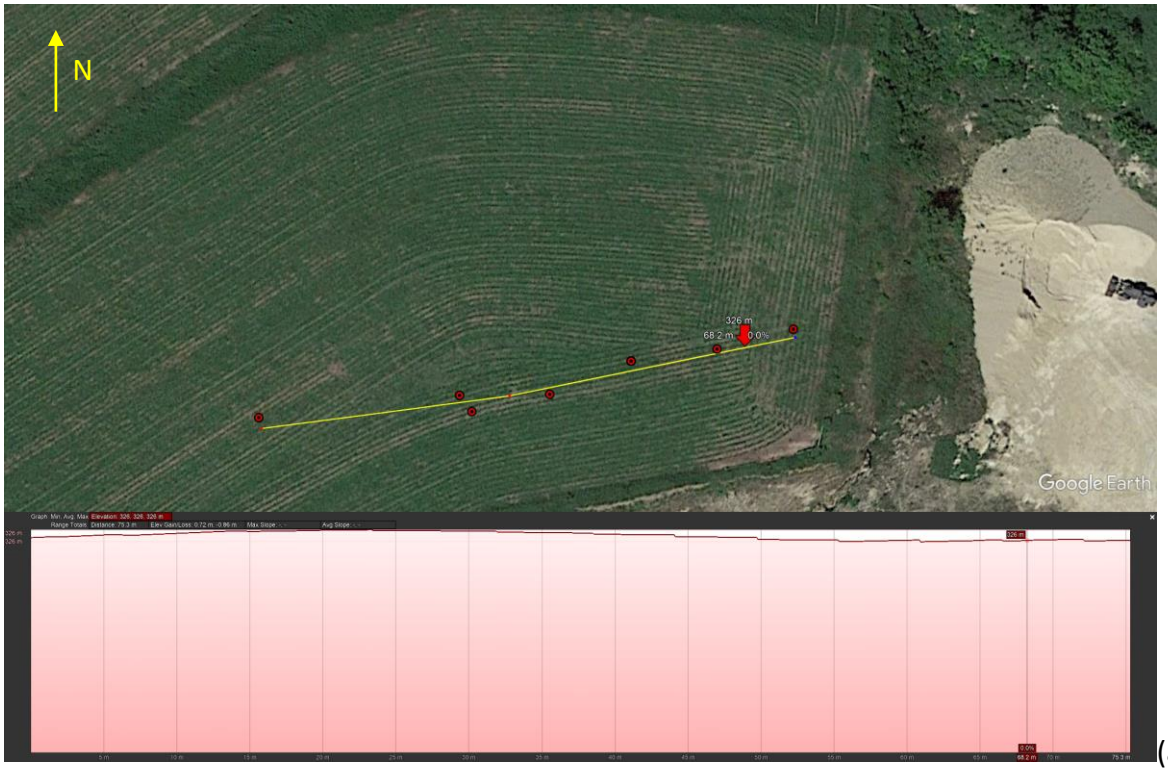

(a)

East West

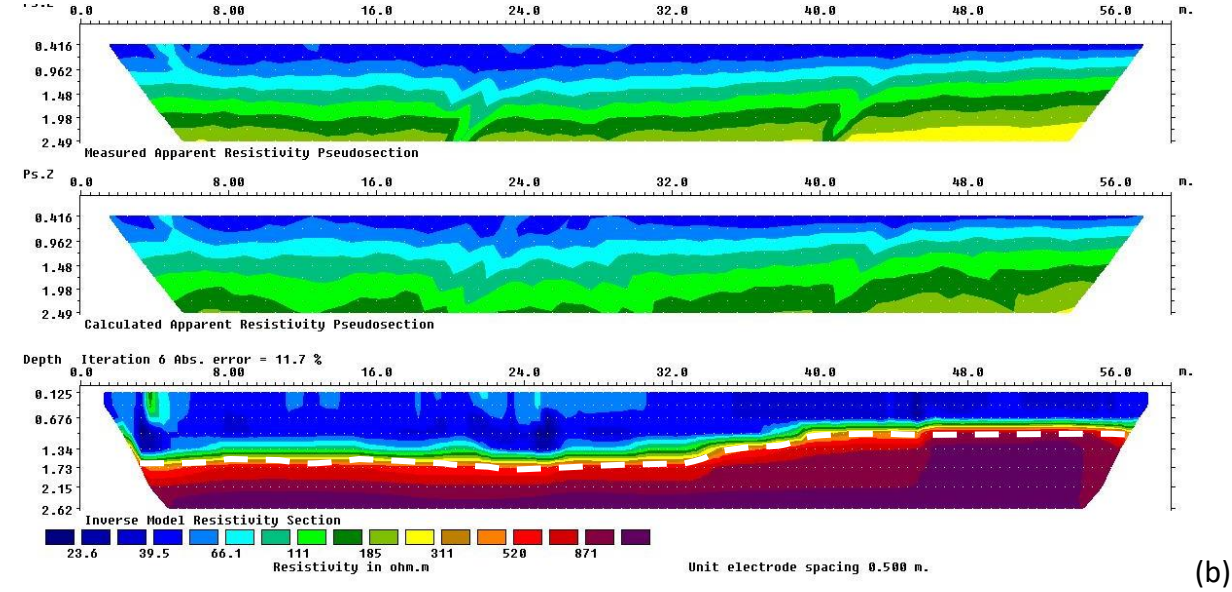

(b)

Figure B.38: (a) Location of the electrical resistivity survey (Image: Google Earth), and (b) inverted electrical resistivity tomographic image. The estimated bedrock depth is shown in the dashed white line.

Figure B.39: Location of the Geonics EM-31 electromagnetic survey (Image: Google Earth).

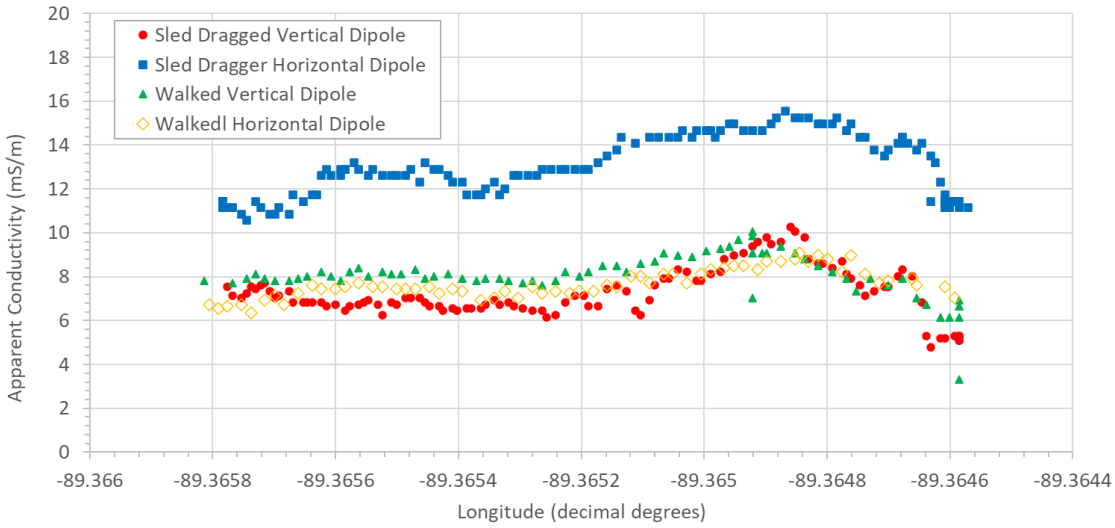

Figure B.40: Electromagnetic data collected with the Geometrics EM+31 sensor. For four configurations, data were collected with vertical and horizontal dipole configurations at about 0.15 m and 1.10 m in height.

The inverted results presented in Figure B.41 indicate an average electrical conductivity of about 5 mS/m for the bedrock and about 50 mS/m for the sediment on top of the bedrock. That corresponds to resistivities of about 200 Ωm for the bedrock and about 20 Ωm for soils. Those values match well with the inverted electrical resistivity results. Still, it might indicate that we overestimated the depth to bedrock by about 0.2 m in the electrical resistivity tomography image (see Figure B.37). Furthermore, the high conductivity of the surface soils also explains why the GPR survey was not successful in mapping the presence of the bedrock. The inverted bedrock depth using the electromagnetic data yields a value that starts at about 1.6 m at the West end and drops to about 0.8 m at the array's center to increase to 2 m at the East end. Using the Geonics EM-31 instrument required running the sensor four times over the same path. Completing the survey and changing the configuration between runs took about 30 minutes.

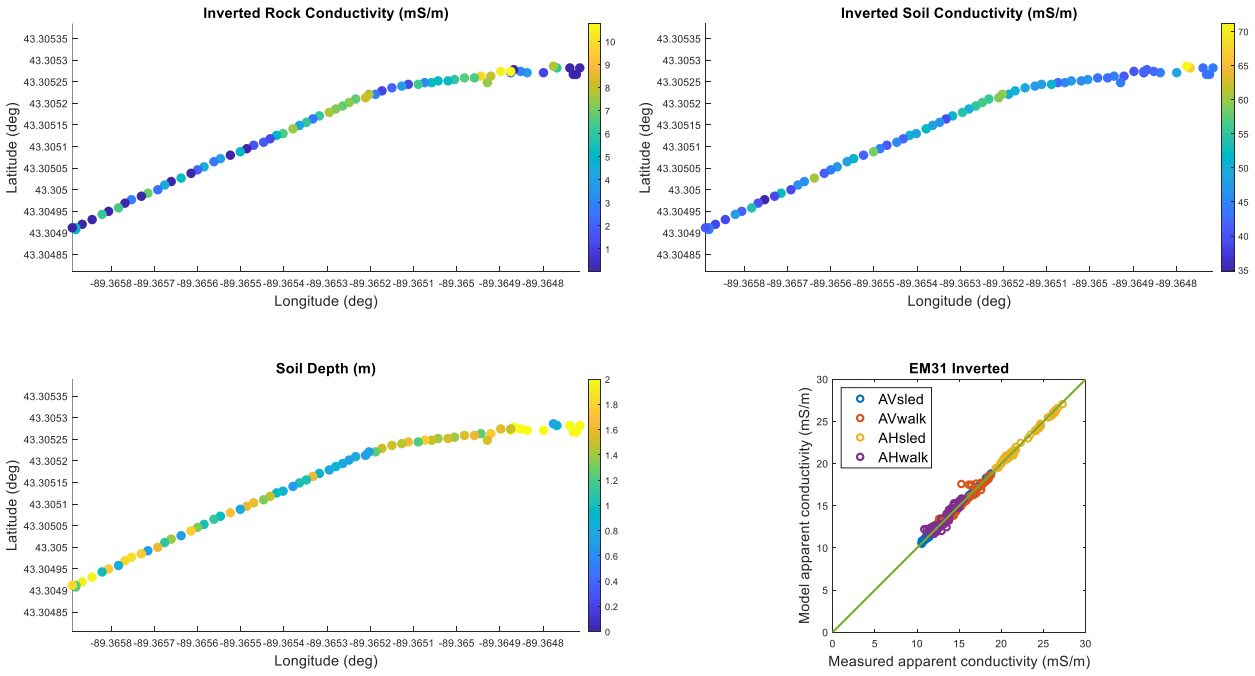

Figure B.41: Electromagnetic data were inverted for the electrical conductivities of the sediment and bedrock and the bedrock depth. The quality of the inversion was assessed by comparing the measured and modeled apparent conductivities for all three measurement configurations.

B.4.5 Southcentral Wisconsin: Jefferson County Farm (Figure B.21)

We collected electromagnetic, electrical resistivity, and seismic refraction survey data along the edge of a newly planted soybean field just northeast of the town of Waterloo in Jefferson County, WI. The survey line for all the surveys was in the North-South direction at the East edge of the field (Figure B.42). We used the Dualem-42 instrument in the electromagnetic survey. This sensor allows the collection of electromagnetic data in four configurations simultaneously. This specification permits a more rapid pace of data collection than the Geonics EM-31 instrument. Figure B.43 shows the electromagnetic collected at the site. Of all the data traces, the 1-m perpendicular dipole shows negative electrical conductivity values and was discarded for further analysis.

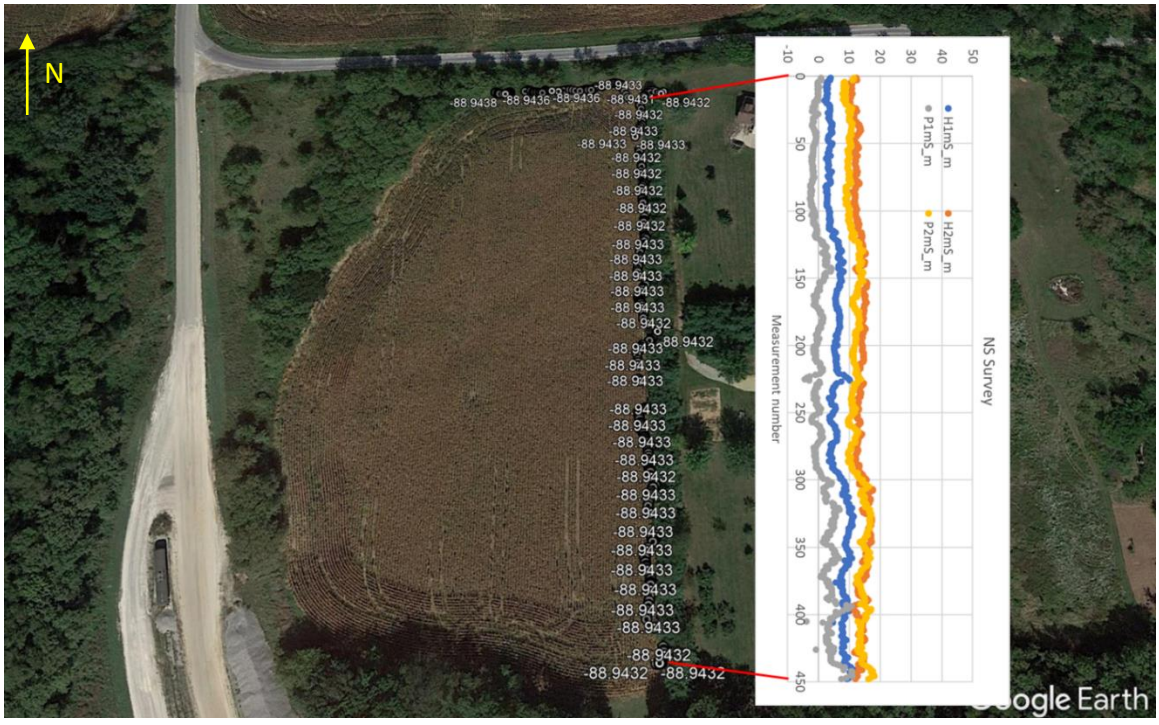

Figure B.42: Location of the Columbia County farm and the survey line along the east edge of the farm field (Image: Google Earth).

To interpret these results, we must consider that the data includes two different sensing configurations: vertical and horizontal. Let's assume that a layer interface is at a depth equal to the 1 m dipole separation, so the dimensionless depth z = 1 for the 1 m dipole separation and z = 0.5 for the 2 m dipole separation. We can assess how the different configurations sense the subsurface using the cumulative current vs. dimensionless plot in Figure B.44. Results indicate that the 1-0 perpendicular dipole configuration is most sensitive to surface layers. In contrast, the 2-m vertical dipole configuration is most sensitive to deeper layers. Following this analysis, it appears that the electrical conductivity increases with depth, and the Electromatic Dualem-42 sensor is not sensing the presence of bedrock as we would have expected a reduction in the apparent conductivity as the depth sensitivity of the instrument increases.

South North

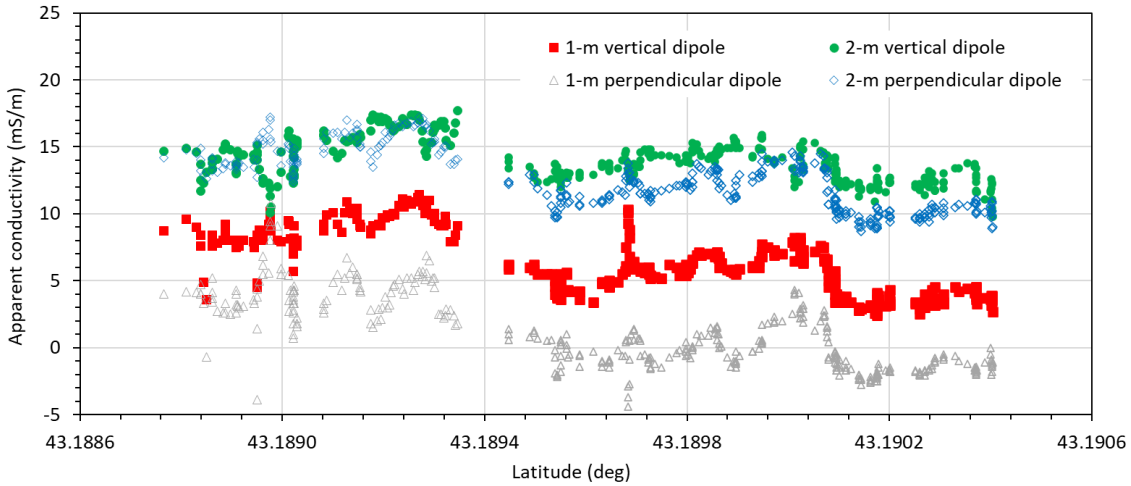

Figure B.43: Electromagnetic data collected with the Dualem-42 instrumented in the Columbia County farm.

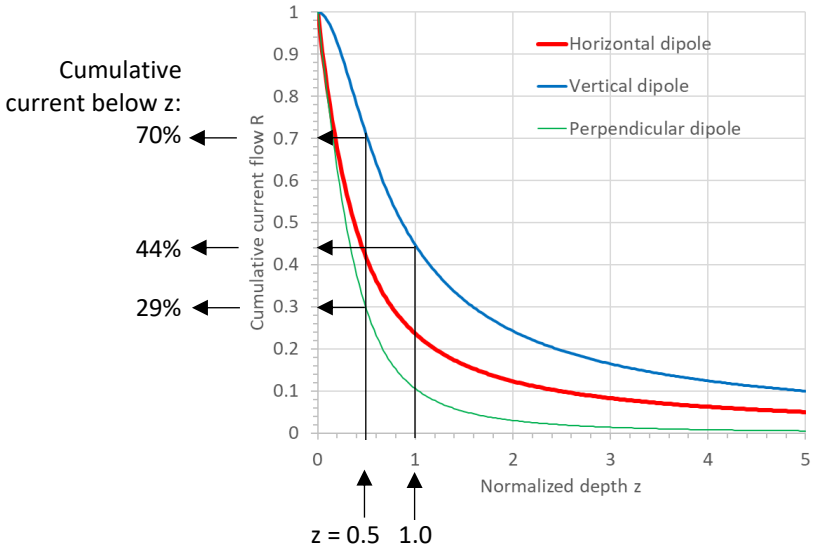

Figure B.44: Cumulative current flow R as a function of the normalized depth z for vertical, horizontal, and perpendicular dipole modes (modified after McNeill 1980; Fetterman and Labson 2005; Milson 2010; Dualem 2023).

Please note that the Geonics EM-31, with 3.7 m separation, would increase the depth sensitivity by 84%, extending the depth where the bedrock interfaces could be imaged. This advantage is offset by the need to run the EM-31 four times over the same line as each sensing configuration runs independently.

We collected electrical resistivity data along the same path as the electromagnetic survey (Figure B.45). We ran the study using 36 5-m separated electrodes, and the survey took about 2.5 hours to set up the array, collect the data, and remove the electrodes and cables. We interpreted collected data in an electrical resistivity tomography image (Figure B.46). We used the 500-Ωm electrical resistivity transition in the electrical resistivity to delineate the presence of the bedrock. The estimated bedrock depth ranges between 6 and 9 m below the surface, at the bottom range of the sensitivity of the Dualem-42 electromagnetic sensor, justifying those results.

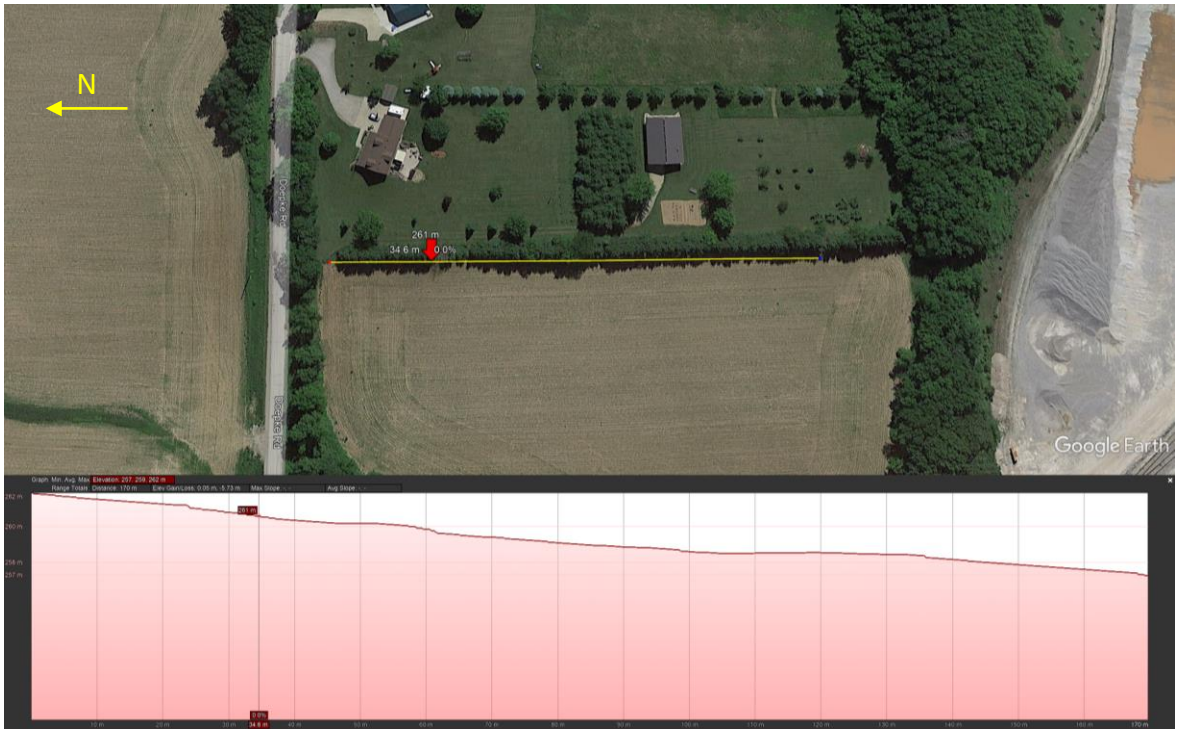

Figure B.45: Location and surface topography of the electrical resistivity survey (Image: Google Earth).

North South

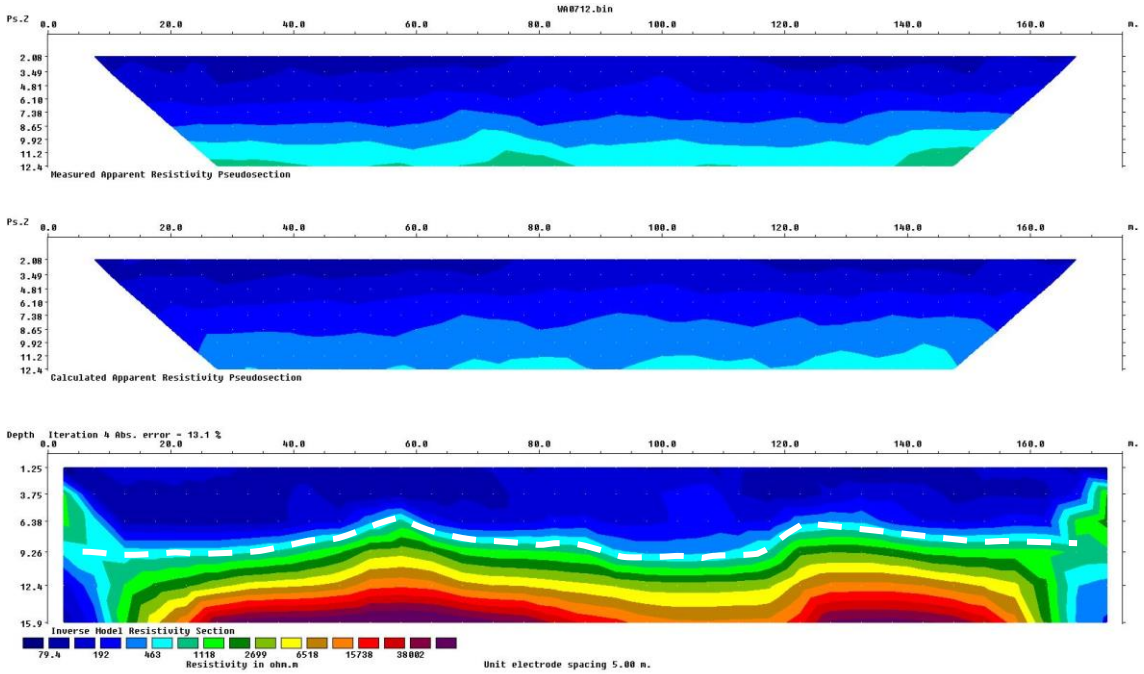

Figure B.46: Pseudo-section of apparent electrical resistivity data and inverted electrical resistivity distribution. We assumed a 500-Ωm transition in the electrical resistivity to delineate the presence of the bedrock (i.e., dashed white line).

Finally, we collected seismic refraction data using SmartSolo geophones. We ran a 72-m long survey line by placing 19 geophones 4 m apart, and we triggered the seismic waves using a sledgehammer. Figure B.47 shows the location of the seismic survey. Please note that the seismic study covered only half of the same site's electromagnetic and electrical resistivity survey length. Still, the survey took about 1.5 hours to deploy the geophones, gather the metadata, collect the seismic data, and retrieve all the geophones.

Figure B.48 presents the raw data collected with the seismic survey for three of the seven shots collected at the site. We analyzed the first arrivals of the first and last shots to create a profile of the refractor represented by the bedrock, and then we used the plus-minus method presented in Equations B.14 through B.23 to create a profile of the bedrock depth. Figure B.49 summarizes the forward and reversed arrival times, plus and minus times, and the resulting depth to the bedrock profile. Interpreted results show a P-wave velocity of ~485 m/s for the top sediment and 2945 m/s for bedrock, and bedrock depths ranging between 4.5 and 6.5 m. Figure B.50 compares the profile results obtained with the seismic refraction data with the image obtained with the electrical resistivity data. While both bedrock profiles have similar shapes, the depth obtained with seismic refraction is shallower than with electrical resistivity. There are two possible explanations for the difference in the results: (1) the selected electrical resistivity transition for the electrical resistivity is too high, or (2) the electrical resistivity contrast and the wave velocity contrast are different, so the boundary is not uniquely defined.

Figure B.47: Location and surface topography of the seismic refraction survey in the Columbia County farm (Image: Google Earth).

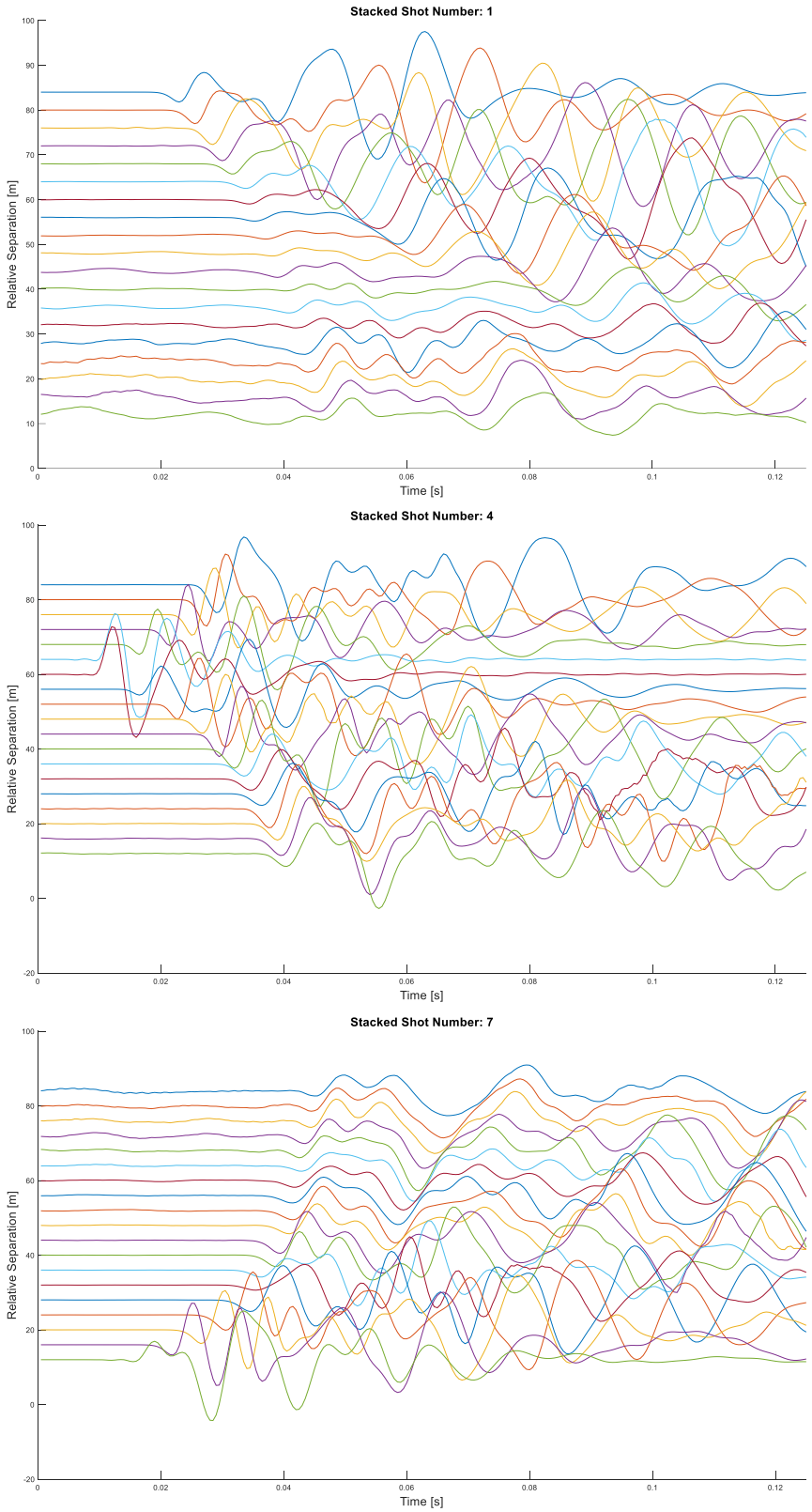

Figure B.48: Examples of the stacked seismic traces collected at the Columbia County farm.

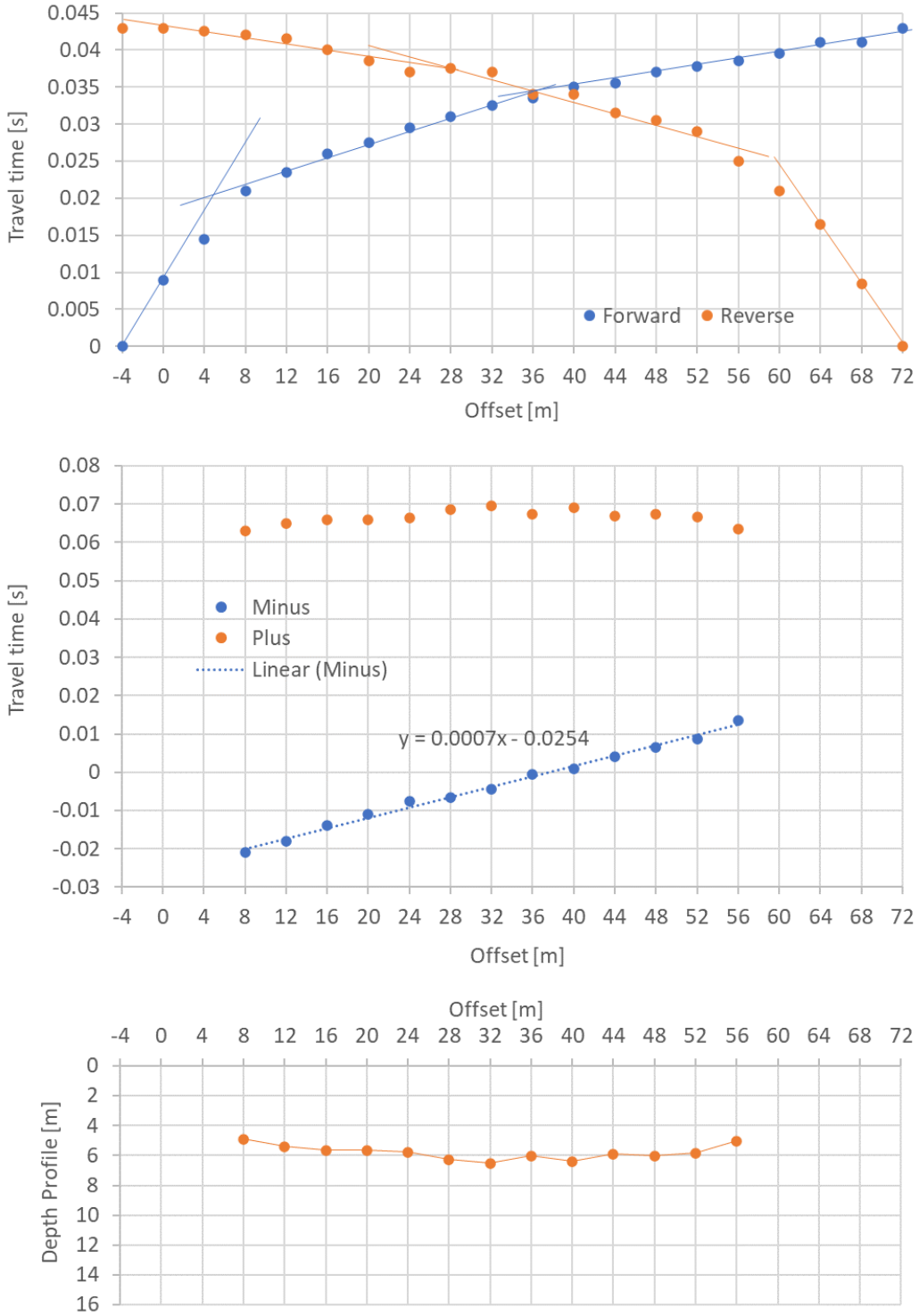

Figure B.49: Summary of the data reduction for interpreting the seismic refraction data.

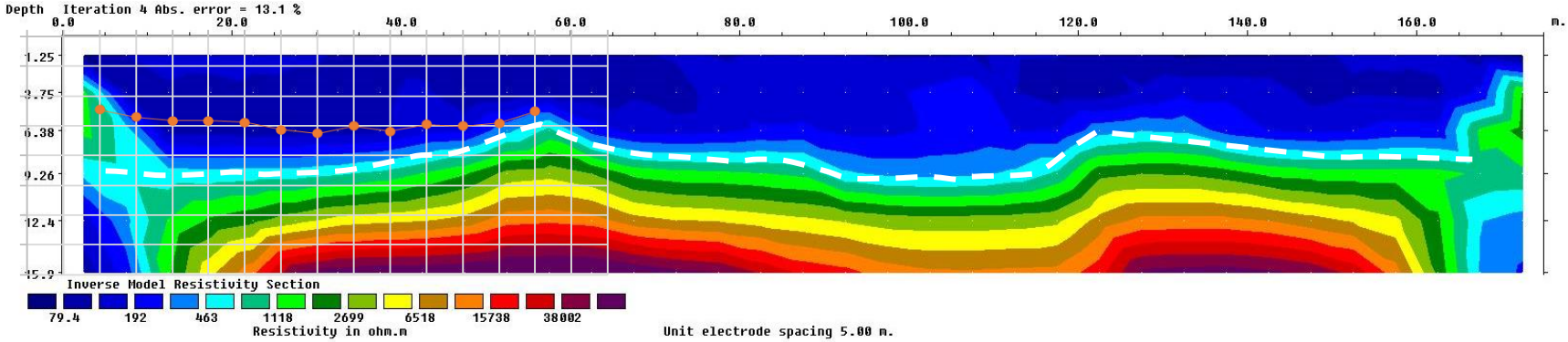

Figure B.50: Comparison of the interpreted bedrock depth obtained with electrical resistivity tomography (dashed white line) and seismic refraction (orange points).

B.4.6 Southcentral Wisconsin: Dane County Yahara River Site (Figure B.21)

We collected electrical resistivity and seismic refraction data along the east bank of the Yahara River Southeast of Madison, WI. Figure B.51 shows the topography of the grassy area where data where the electrical resistivity and seismic refraction data were collected.

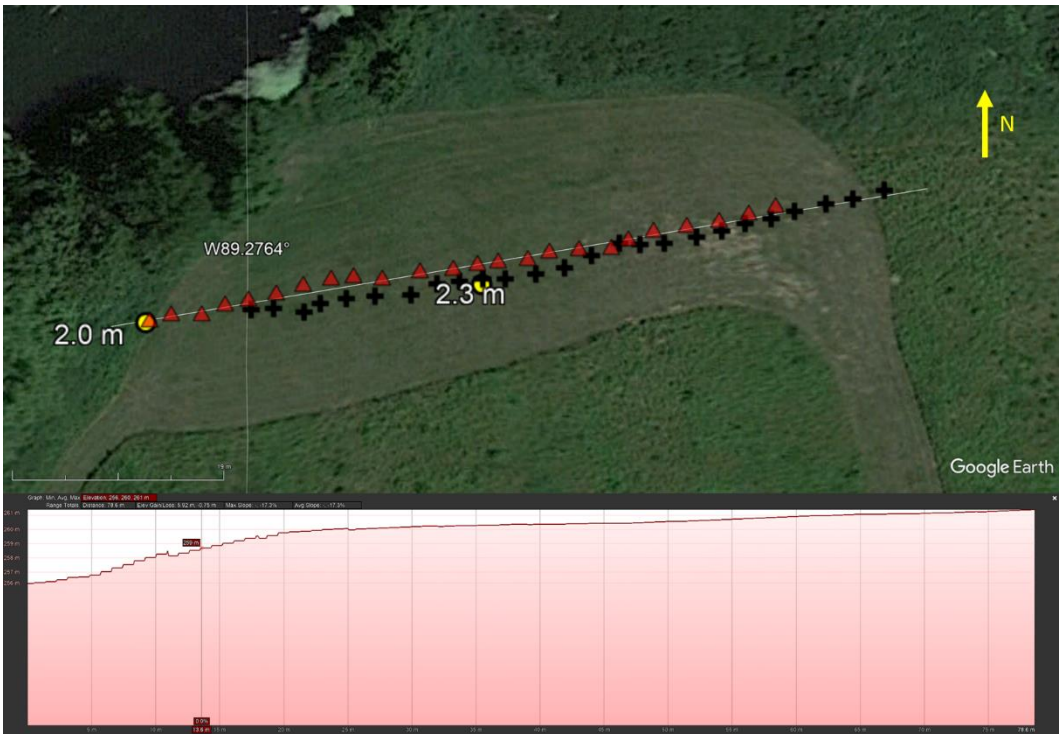

Figure B.51: Overview of the Dane County Yahara River site.

The separation of the electrodes for the electrical resistivity was 2.5 m (Figure B.52a), and the separation of the SmartSolo geophones was 2.5 m (Figure B.52b). We triggered the seismic waves using a sledgehammer. The geophones were synchronized using their internal GPS clocks. We located the sources at both ends and two locations within the survey lines. Figure B.53 shows quality electrical resistivity and seismic refraction data collected at the site—the interpretation of the results using the Res2Dinv software and Eqs. B.20 and B.23 (for the seismic refraction), and corrected for topography, matched across most of the profile well, as shown in Figure B.54.

There is one mismatch between the two profiles at the center of the survey though (see yellow rectangle in Figure B.54). That mismatch might be explained by the difference in the physical response of the two surveys: electrical resistivity images contrast the electrical properties of the sediments and bedrock, and seismic refraction senses a change in stiffness. While these properties are assumed to change at the locations, they might not necessarily coincide.

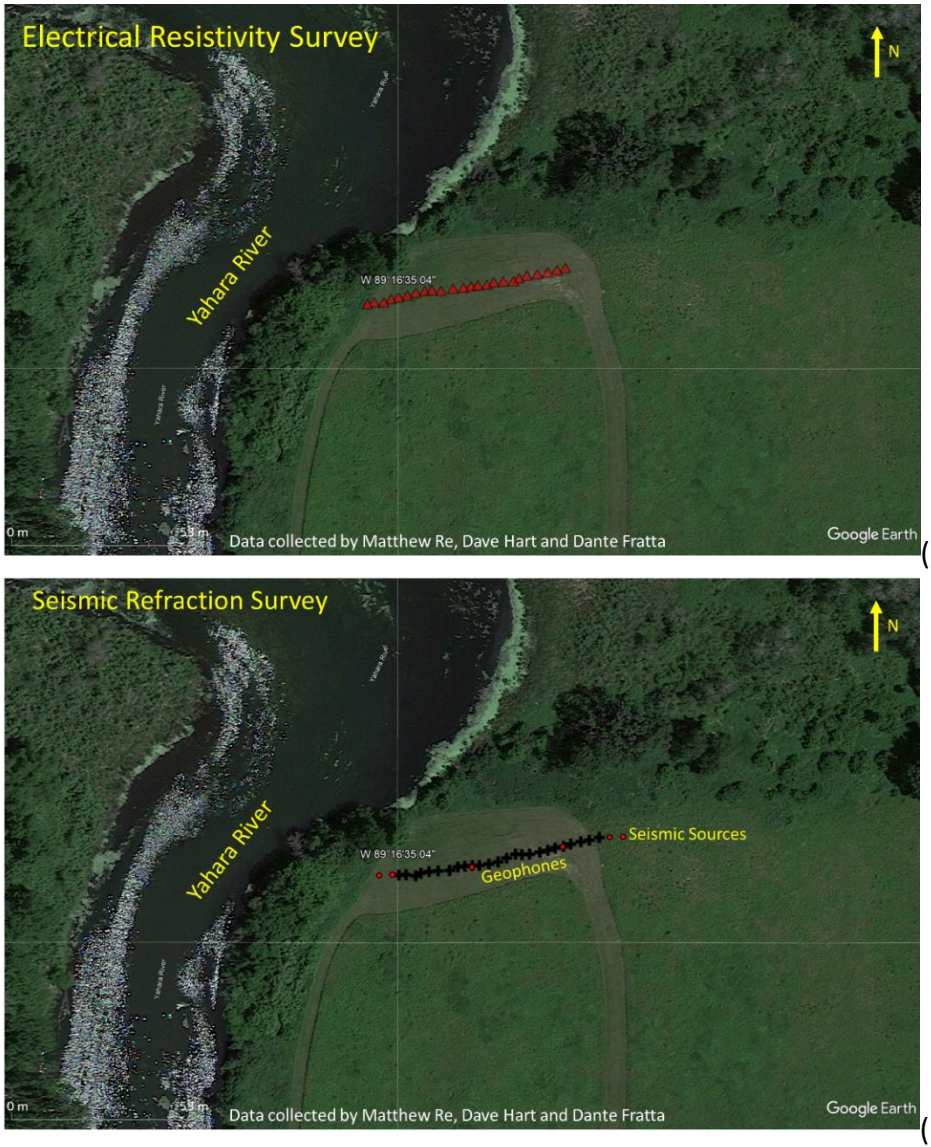

Figure B.52: Locations of (a) electrodes and (b) Smartsolo geophones and seismic sources at the Dane County Yahara River Site.

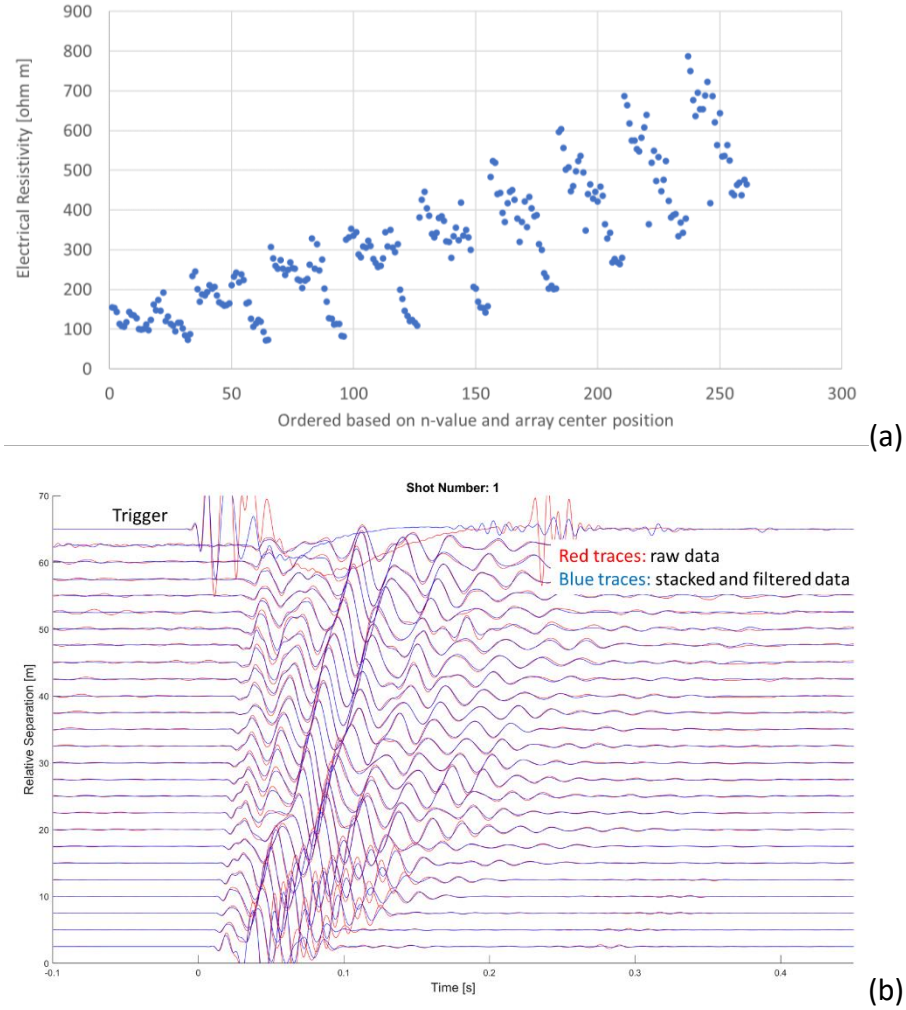

Figure B.53: Raw (a) electrical resistivity and (b) seismic refraction data collected at the Dane County Yahara River Site.

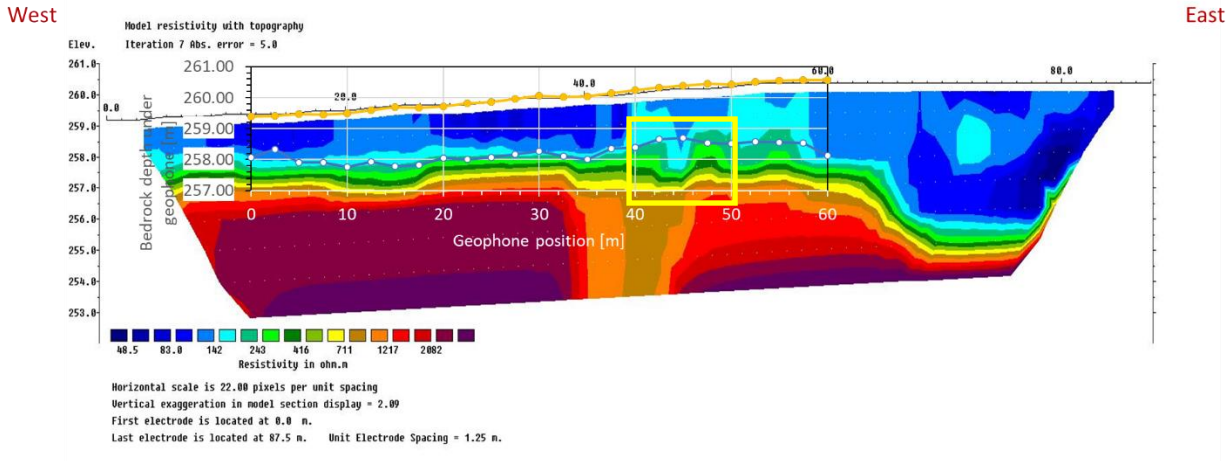

Figure B.54: Interpreted electrical resistivity and seismic refraction data collected at the Dane County Yahara River Site.

B.5. Conclusions and Recommendations

We studied different near-surface geophysical surveys as measurement techniques to comply with the requirement of Wisconsin's N.R. 151 *Maximum liquid manure application rates for Silurian bedrock as a function of depth.* We evaluated ground penetrating radar, electrical resistivity, electromagnetics, and seismic refraction techniques. We assessed penetration depth, sensitivity, ease of deployment and interpretation, and implementation cost. Each method has pros and cons that might help regulators and farmers decide on selecting one type of sensor over others.

- Ground Penetrating Radar: Provides the finest resolution of all the tested techniques, is operated by a single person, and can be rapidly deployed in open plots with little vegetation using carts. A single operation can cover up to a kilometer of survey in an hour. However, Ground Penetrating Radar is highly limited by high conductivity sediments such as clayey soils or soils they have repeatedly with fertilizers. Under those environments, Ground Penetrating Radar signal have very little depth of penetration. Typical Ground Penetrating Radar instruments cost between $50K and $100K.
- Electrical Resistivity Tomography: Provides different resolutions and penetration of electrical resistivity measurements by varying the separation between electrodes for various soils and rock environments. While a single person can operate it, the technique requires the deployment of cables and electrodes in electrical contact with the ground surface. Our study used an entry-level instrument that costs about $25K and can collect data 100 m per hour with a 4-m electrode separation. Higher collection rates can be

achieved with larger electrode separations (at the cost of lower resolution at the near surface) or with more advanced instruments (at a more significant price).

- Electromagnetism: Senses the electrical conductivity of near-surface soils and rocks by exciting and monitoring the response of a time-varying electromagnetic field across a field. The instrument does not need to be in contact with sediment or rock surfaces. The technique senses different depths by changing the sensing coils' elevation, separation, or orientation. For our study, we used two different instruments. The Geonics EM-31 uses a single elevation and orientation of the sensing electrodes. Still, those parameters can be manually changed while running the instrument along the same survey line multiple times. The Dualem-42 simultaneously collects four different sensing coil configurations, significantly reducing survey times. The sensor can be carried or pulled by a one or two-person crew at 1 km per hour. The data acquisition rate for either sensor can be sped up with mechanized vehicles. Still, care must be taken to prevent the interaction of the vehicle's metal with the electromagnetic responses. The main disadvantage of the techniques is that traces can be noisy, and our team had more success with Geonics instruments. The cost of the sensors ranges between $35K and $50K.
- Seismic refraction: Uses the high contrast in P-wave velocity between the low-velocity sediment and high-velocity bedrock allows the refraction of P-waves and imaging of the bedrock depth and topography. We used a setup with nodal geophones that does not require the deployment of cables and uses GPS clocks to synchronize the measurements across the array. The instrument set costs about $30K to $35K for systems with 24 geophones and a charges/data download system. While the data collection time is similar

to the electrical resistivity system (about 100 m/hour); the managing and interpreting of the data is much more complex than electrical resistivity tomography.

By evaluating the response of all tested instruments, assessing the results, and evaluating the interpretation, we found that electrical resistivity, while it can be relatively slow to deploy, is a geophysical technique that allows reaching the depth of penetration and the needed resolution by changing electrodes separation, the collected data has high signal-to-noise ratio, single persons can operate, it is a relatively cheap instrument, and the interpretation is relatively simple. If a higher data collection rate is desired, we recommend using electromagnetic sensors. However, the instruments require careful and frequent calibrations, and users should carefully design the experiment to maintain data quality and better image the bedrock depth.

B.6. References

AGI (2017). "Dipole-dipole array: electrical resistivity methods, Part 3." URL: https://www.agiusa.com/dipole-dipole%E2%80%8B-%E2%80%8Barray%E2%80%8B [Accessed March 27, 2023]

Annan, A. P. (2005). "Ground Penetrating Radar." In Near-Surface Geophysics, Edited by D. K. Butler, Society of Exploration Geophysics, 357-438.

Attia. A. M., Fratta, D. and Bassiouni, Z. (2008). "Irreducible water saturation from capillary pressure and electrical resistivity measurements." Oil & Gas Science and Technology-Revue de l'IFP 63 (2), 203-217. DOI: https://doi.org/10.2516/ogst:2007066.

Burger, H. R., Sheehan, A. F., and Jones, C. H. (2006). "Introduction to Applied Geophysics." Norton. 600 pages.

Callegary, J. B., Ferre, T. P. A., and Groom, R. W. (2007). "Vertical Spatial Sensitivity and Exploration Depth of Low-Induction-Number Electromagnetic-Induction Instruments." Vadose Zone Journal. 6:158–167. doi: https://doi.org/10.2136/vzj2006.0120.

Dualem (2023). "Analysis of Conductive Layering by Electromagnetic (EM) Vertical Sounding." URL: https://dualem.com/documents/vertical-sounding/ [Accessed on June 1, 2023].

EPA (2023). "Electrical Conductivity and Resistivity." US Environmental Protection Agency. URL: https://www.epa.gov/environmental-geophysics/electrical-conductivity-and-resistivity#:~:text=Archie's%20Law%20predicts%20an%20inverse,relationship%20between%20%CF%81%20and%20k. [Accessed on December 25, 2023].

Everett, M. E. (2013). “Near-Surface Applied Geophysics.” Cambridge. 403 pp.

Fetterman, D. V., and Labson, V. F. (2005). “Electromagnetic Induction Methods for Environmental Problems.” In Near-Surface Geophysics, Edited by D. K. Butler, Society of Exploration Geophysics, 301-355

Hart, D., Swager, K., Graham, G., Streiff, C., Fratta, D., Komiskey, M., Minsley, B., and Hunt, R. (2020). “Geophysical determination of depth to bedrock in agricultural fields.” GSA 2020 Session, paper 138-8. T89. Applying Near Surface Geophysics to Solve Geological Problems. 28 October 2020.

Jol, H. M. (2009). “Ground Penetrating Radar: Theory and Applications.” Elsevier. 524 pages.

KBGPR Surveys (2023). Module 3.4: GPR resolution. URL: https://kbgprsurveys.co.uk/gpr-training/module-3-4-gpr-ground-penetrating-radar-resolution/ [Accessed March 31, 2023]

Keary, P., Brooks, M, and Hill, I. (2002). An Introduction to Geophysical Exploration.” Blackwell. 262 pp.

Liu, X., Chen, J., Cui, X., Liu, Q., Cao, X., and Chen, X. (2017). Measurement of soil water content using ground-penetrating radar: A review of current methods. International Journal of Digital Earth, 12(1), 95-118. https://doi.org/10.1080/17538947.2017.1412520.

Loke M. H., (2016). RES2DMOD ver. 3.03, Rapid 2D resistivity and I.P. forward modeling using the finite-difference and finite-element methods. URL: https: www.geotomosoft.com.

Lowry, C. S., Fratta, D., Anderson, M. P. (2009). “Ground penetrating radar and spring formation in a groundwater-dominated peat wetland.” Journal of Hydrology 373 (2009) 68–79.

McNeill, J. D. (1980). “Electromagnetic Terrain Conductivity Measurement at Low Induction Regime.” Technical Note TN-6/ Geonics, Mississauga, Canada.

Milson, J. (2010). “Field Geophysics.” The Geological Field Guide Series. Third Edition, Wiley. 232 pp.

Mitsuhata, Y., Ueda, T., Kamimura, A. Kato, S., Takeuchi, A., Aduma, C., and Yokota, T. (2022). “Development of a drone-borne electromagnetic survey system for searching for buried vehicles and soil resistivity mapping.” Near Surface Geophysics, 20, 16–29. doi: https://doi.org/10.1002/nsg.12189.

Neyamadpour, A., Wan Abdullah, W. A., Taib, S., and Neyamadpour, B. (2010). Comparison of Wenner and dipole–dipole arrays in the study of an underground three-dimensional cavity. Journal of Geophysics and Engineering, 7(1), 30-40. Doi: https://doi.org/10.1088/1742-2132/7/1/003.

Pelton, J. R. (2005). “Near-Surface Seismology: Surface Waves Methods.” In Near Surface Geophysics. Society of Exploration Geophysicists. Tulsa, OK.

Santamarina. J. C., Klein, K., and Fam, M. A. (2001). “Soils and Waves.” Wiley. In Near-Surface Geophysics, Ed. D. Buttler, SEG. Tulsa, OK. pp. 218-263.

Santamarina, J. C., Rinaldi, V. A., Fratta, D., Klein, K. A., Wang. Y.-H., Cho, G.-C., and Cascante, G. (2005). “A Survey of Elastic and Electromagnetic Properties of Near-Surface Soils.” In Near-Surface Geophysics, Ed. D. Buttler, SEG. Tulsa, OK. pp. 71-87.

Sharma, P. V. (1997). “Environmental and Engineering Geophysics.” Cambridge University Press. 475 pages.

Utsi, E. C. (2017). Chapter 1: Fundamentals of GPR operation. In Ground penetrating radar: Theory and practice (pp. 1-11). Butterworth-Heinemann.

Witten, A. J. (2014). Handbook of geophysics and archaeology. Routledge.

WGNHS (2009). Karst and Shallow Carbonate Bedrock in Wisconsin. Wisconsin Geological and Natural History Survey. Factsheet 02. URL: https://wgnhs.wisc.edu/catalog/publication/000905/resource/ fs02 [Accessed August 1, 2023].

Zonge, K., Wynn, J., and Urquhart, S. (2005). “Resistivity, Induced Polarization and Complex Resistivity.” In Near-Surface Geophysics, Ed. D. Buttler, SEG. Tulsa, OK. pp. 265-300.

Appendices

Appendix A: Sample Calculations

Molar dissociation for NaBr

The 1:1 molar dissociation of sodium bromide (NaBr) was calculated to create a 100 mg/L (ppm) solution for bromide calibration standard concentrations used for HPIC testing.

$NaBr \rightarrow Na^{+} + Br^{-}$

1 mole Na^{+} = 22.990 g

1 mole Br^{-} = 79.904 g

Molar mass of NaBr = 102.894 g

$$(x\ g\ NaBr) \times \left(\frac{1\ mole\ NaBr}{102.894\ g\ Nabr}\right) \times \left(\frac{1\ mole\ Br^{-}}{1\ mole\ NaBr}\right) \times \left(\frac{79.904\ g\ Br^{-}}{1\ mole\ Br^{-}}\right) = \frac{1000\ mg\ Br^{-}}{1\ L\ water}$$

$$x\ g\ NaBr = 1.288\ g\ NaBr$$

Normalized infiltration time for short-term infiltration experiment

The total infiltration time for the sodium bromide solution into the short-term experiment area was 8 minutes. However, since the boundary created to contain the solution leaving the infiltrometer in the short-term infiltration experiment was a square area and the previous experiments were a circular area, this time value was corrected to match the parameters for infiltration of the previous experiments.

$$t_{corrected} = t_{measured}\left(\frac{A_{square}}{A_{circle}}\right)\left(\frac{V_{circle}}{V_{sqaure}}\right)$$

$$t_{corrected} = 8\ mins\left(\frac{1\ m^2}{0.13\ m^2}\right)\left(\frac{76\ L}{40\ L}\right)$$

$t_{corrected} = 116.9\ mins$

Hydraulic conductivity

The following is a sample calculation using a simplified version of A.2 to determine the unsaturated hydraulic conductivity for the short-term infiltration experiment.

$$q = \frac{V}{t} = K_{unsat}\frac{\Delta h_T}{L}A$$

$$\frac{0.04\ m^2}{8\ mins\left(\frac{1\ day}{1440\ mins}\right)} = K_{unsat}\left(\frac{0.05\ m}{0.10\ m}\right)1\ m^2$$

$$K_{unsat} = 14.4\ \frac{m}{day}$$

Appendix B: Supporting Data

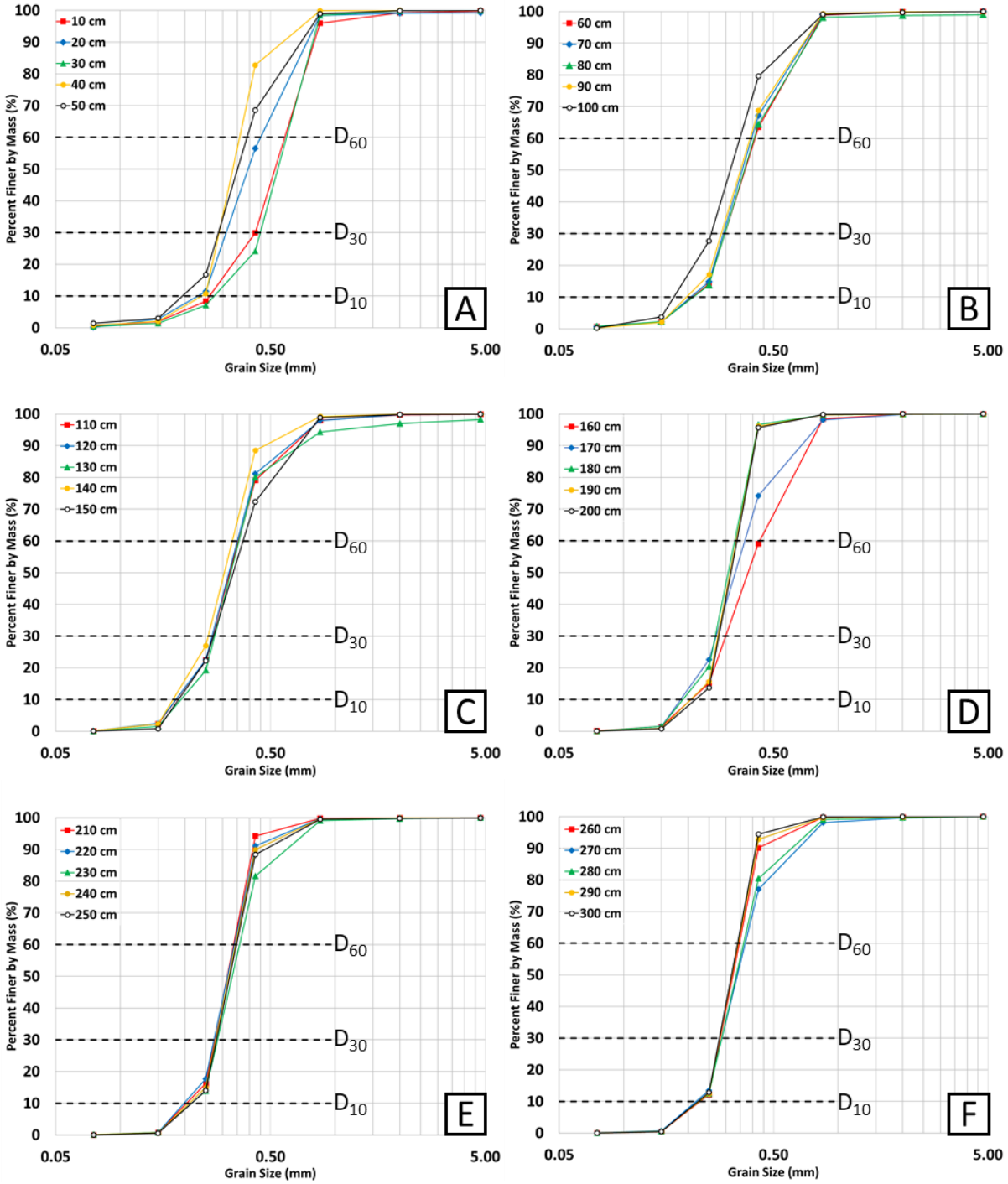

Figure A. 38: Grain size distribution curve for soil core sample 50 m northwest of injection areas. A) depths from ground surface to 50 cm, B) depths from 50-100 cm, C) depths from 100- 150 cm, D) depths from 150-200 cm, E) depths from 200-250 cm, F) depths from 250-300 cm.

Table A.5: Fertilizer schedule and details for the 2020 and 2022 farming seasons of Field 19 near the testing site (after Long, 2023).

Application Date	Application Type	NPK(S)*	Amount (kg/ha)	Amount (L/ha)
2020-May-09	Dry	0-0-60	117.71	
2020-May-09	Dry	21-0-0-24	78.47	
2020-May-21	Liquid	20-0-0-8		99.25
2020-Jun-08	Liquid	20-0-4-3		284.36
2020-Jun-29	Liquid	20-0-4-3		224.50
2020-Jul-11	Liquid	20-0-4-3		215.14
2022-May-22	Liquid	18-4-4-3		107.57
2022-May-22	Liquid	6-18-6		30.40
2022-Jun-10	Dry	0-0-60	156.94	
2022-Jun-10	Dry	21-0-0-24	89.68	
2022-Jun-14	Liquid	20-0-4-3		284.36
2022-Jun-27	Liquid	20-0-4-3		181.00
2022-Jul-11	Liquid	20-0-4-3		151.72
2022-Jul-26	Liquid	20-0-4-3		147.33

*NPK(S) is the percentage amount of nitrogen, phosphorous, potassium, and sulfur contained in the fertilizer.

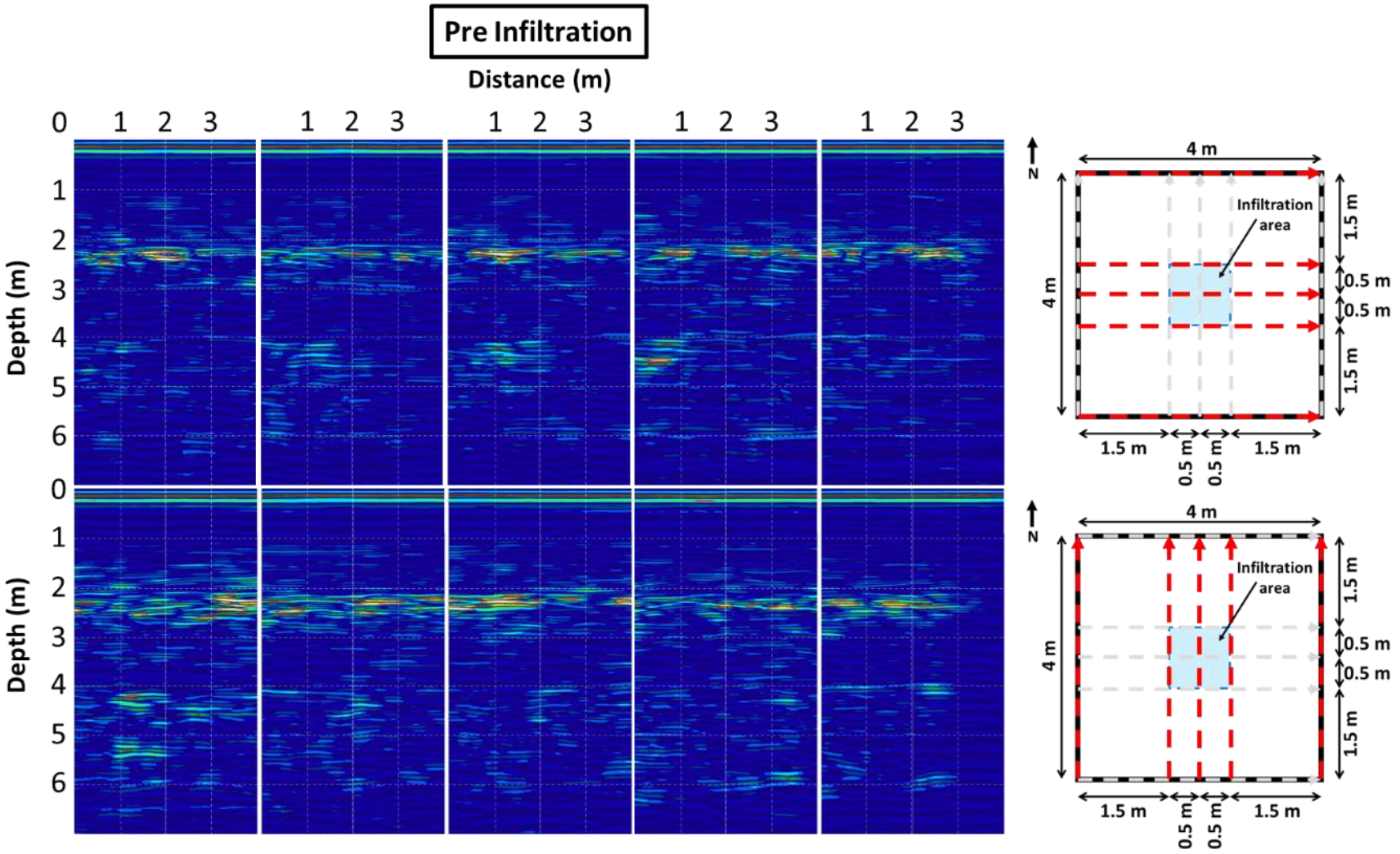

Figure A. 39: GPR results for the pre-infiltrations conditions of the short-term infiltration experiment in the west-to-east and south-to-north directions.

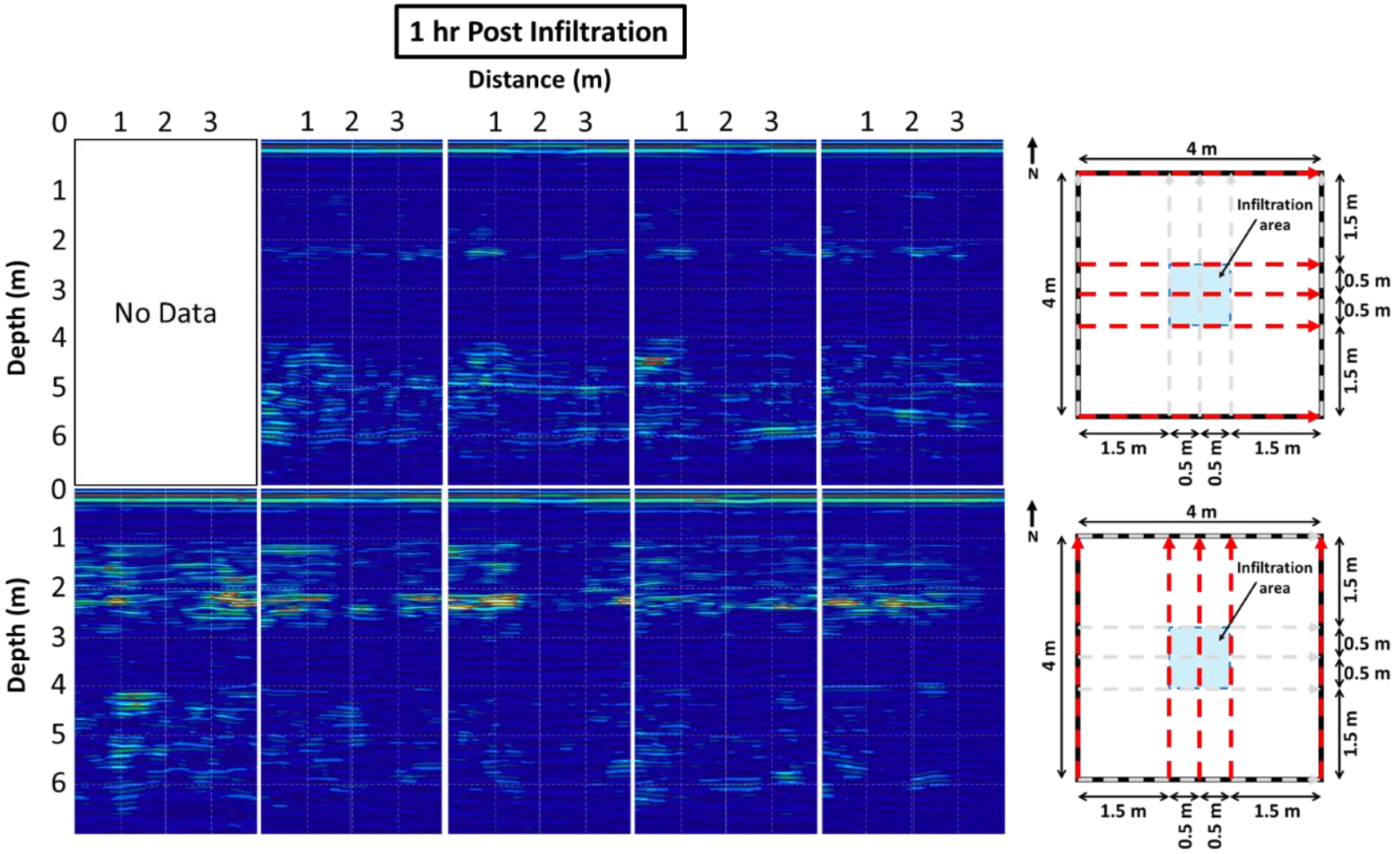

Figure A. 40: GPR results one hour after a sodium bromide solution infiltration in the short-term infiltration experiment.

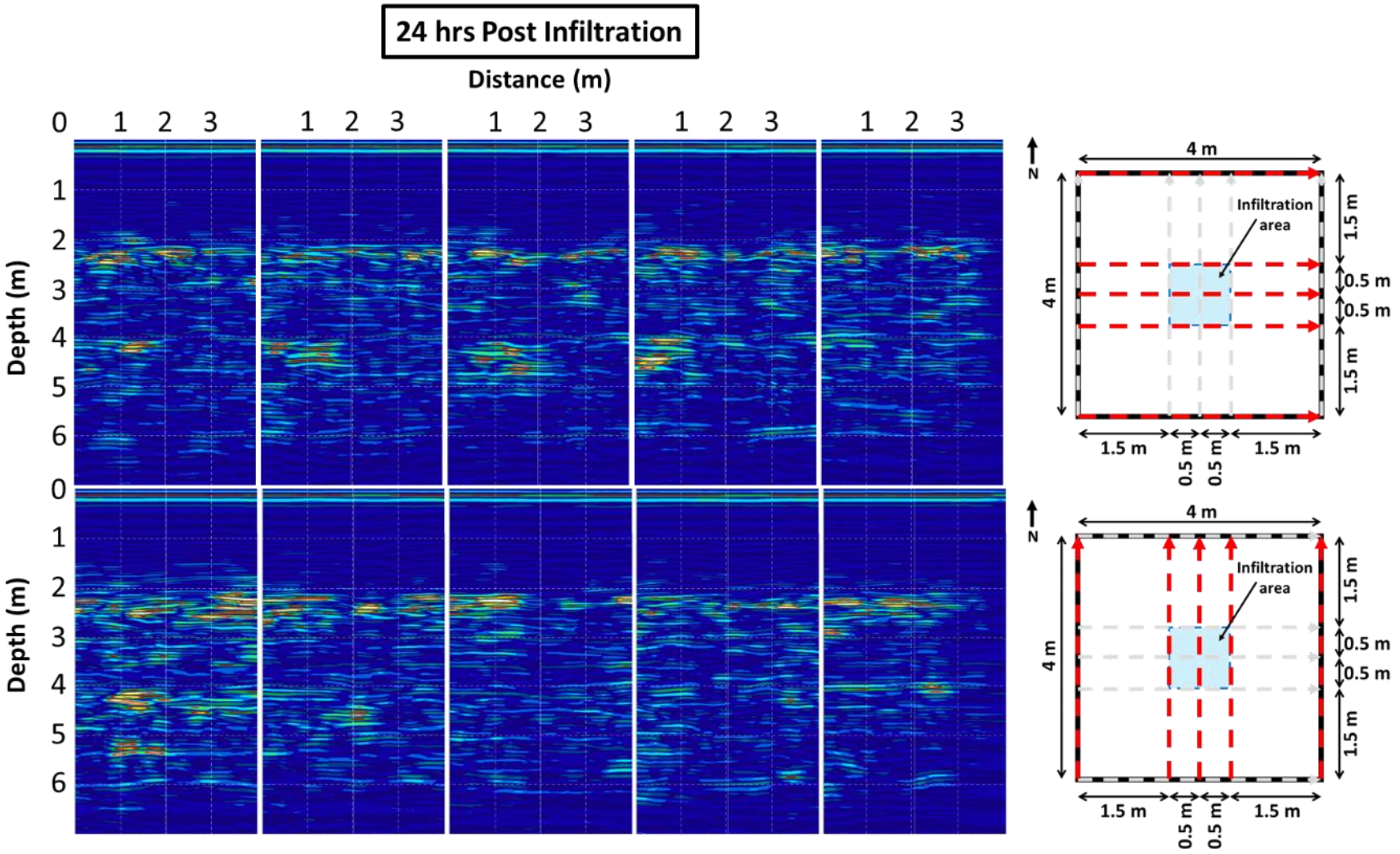

Figure A. 41: GPR results 24 hours after a sodium bromide solution infiltration in the short-term infiltration experiment.

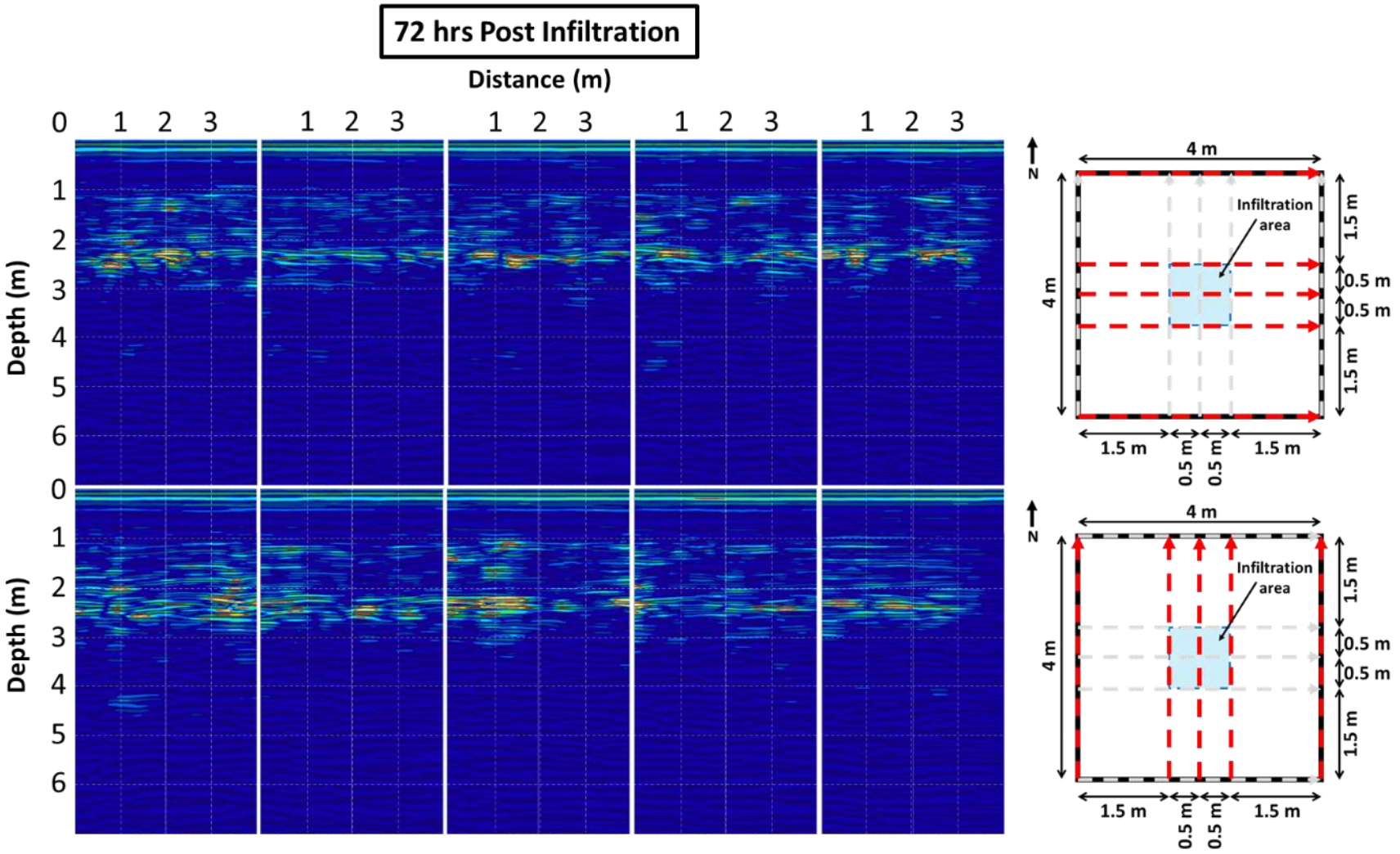

Figure A. 42: GPR results 72 hours after the infiltration of a sodium bromide solution in the short-term infiltration experiment